

**AN ENDCAP ELECTROMAGNETIC
CALORIMETER
FOR STAR**

TECHNICAL DESIGN UPDATE #1

February 10, 2000

Contents

1	Introduction	1
2	New Physics Simulations	5
2.1	Sensitivity of γ +jet to $\Delta G(x)$	5
2.2	'Fragmentation photon' background to γ +jet coincidences	8
2.3	Partonic kinematics reconstruction in W^\pm production	9
2.4	Sensitivity to quark polarization: Drell-Yan and high- p_T dijets	13
2.5	Simulated performance of the EEMC and SMD for $p + p$ collisions	13
2.6	EEMC tower performance	17
3	Prototype Detector Construction and Testing	18
3.1	Description of the prototype calorimeter	18
3.2	Description of the prototype shower-maximum detector	20
3.3	Description of simulations for the prototype	20
3.4	Detector tests	21
3.5	Status of T-438 data analysis	23
3.5.1	pSMD gain matching	23
3.5.2	Analysis of average transverse profile of electron showers	25
3.5.3	Analysis of event fluctuations of the shower profile	27
3.6	Summary of lessons learned from T-438	28
4	Mechanical Design Updates	31
4.1	Mechanical Structure	31
4.2	Megatile Design and Fabrication	35
4.3	Modular SMD	37
4.4	Suppliers and Manufacturers	40
4.5	Quality Control and Assurance	40
4.6	Coverage and Integration Issues	40
5	Optical System Updates	42
5.1	Tower Optical Construction	42
5.2	Tower Light Budget	42
5.3	SMD Fiber Routing	45
5.4	SMD Light Budget	46
5.5	Optical QA/QC	50
6	Electronics Update	52
6.1	Overview	52
6.2	PMT/MAPMT Tube and Base Selection	52
6.3	Progress on BEMC Electronics	55
6.4	SMD Readout Scheme	56
7	Calibration Issues	61
7.1	Overview of Current Status	61
7.2	Summary of the IUCF Calibration Workshop	61
7.3	A Calibration Scheme for the STAR EEMC	63

7.4	The EEMC UV Laser System	65
8	Integration/Interface with STAR/RHIC	68
8.1	STAR Integration Limits	68
8.2	Conditions on the Rear of the STAR Poletip	71
8.3	Progress on Level 3 Trigger Hardware and Software	74
8.4	Simulations Regarding the Importance of the Full Barrel EMC	79
9	Funding, Management and Schedule	81
9.1	EEMC Funding	81
9.2	Additions to the EEMC Collaboration	82
9.3	Management Plan	84
9.4	Timeline	84
9.5	Budget	84
10	References	92
A	Responses to the Conceptual Design Review	93

1 Introduction

This report summarizes the evolution of the STAR Endcap Electromagnetic Calorimeter (EEMC) project since the Conceptual Design Report [1] was written in April 1999. The intervening months have been marked by the achievement of several major milestones.

An NSF Major Research Instrumentation grant for partial funding (\$1.85 M) of the EEMC was awarded in September 1999. A funding profile for an additional \$2.34 M from the Physics Division at NSF has been established for FY 2000-2002. In combination with contributions from Indiana University and from the Indiana University Cyclotron Facility (IUCF) operating grant, this identifies most of the necessary funding. Additional requests from several collaborating institutions, as needed to complete the funding picture, are currently pending at DOE and NSF. To date, the NSF has authorized IUCF to spend only the first \$250 K of the MRI grant, with release of further funds pending the outcome of the Technical Design Review in February 2000.

Construction of a prototype of the EEMC, containing 12 towers and two orthogonal planes of a scintillating-strip shower-maximum detector (SMD), was completed in August 1999, including wavelength-shifting and clear readout fibers provided by the Michigan State University group. Initial tests of the prototype detector with cosmic rays and with high-energy electron beams at SLAC (in October 1999) have provided essential information on light output, linearity, and shower profile distributions. In particular, the observed SMD performance is consistent with the simulations from which the critical $\pi^0 - \gamma$ discrimination power estimates were originally projected. The performance tests on the prototype and on several alternative SMD scintillating strip geometries are guiding ongoing improvements in scintillator machining techniques, light collection and transmission to phototubes (PMT), PMT base design and simulations.

The basic mechanical design of the EEMC has not changed dramatically from the Conceptual Design Report (CDR), but many engineering details have been fleshed out to permit more accurate planning. The segmentation in pseudorapidity (η) and azimuthal angle (ϕ), and the depth profile, are indicated schematically in Fig. 1, which has been modified from the CDR only in placing the SMD after, rather than before, the 6th layer of tower scintillator tiles. One significant redesign, introduced in response to an earlier concern raised by the Review Committee, is the change to a modular structure for the SMD. Individual 30° modules can now be inserted or extracted from the fully assembled detector, without interfering with other modules. Yet the new design retains the highly desirable feature of avoiding coverage gaps within the overall fiducial area of each EEMC half. An initial extrusion run of *passive* plastic strips of the SMD design geometry has been carried out to allow construction at Argonne National Laboratory of a mechanical prototype of one SMD module. In parallel with this development, preparation of the scintillator megatile machining facility at IUCF is under way, with the imminent installation of a newly purchased high-speed routing machine.

Comparative tests of performance of different candidate phototubes for the EEMC tower readout have been conducted to inform our final choice. Prototype Cockcroft-Walton bases, for both the tower PMT's and the SMD and preshower multi-anode PMT's, are presently under construction in Dubna, and should be available for testing in March 2000. Considerable experience has been gained in quality assurance and control procedures for the scintillator megatiles. In particular, a test stand constructed at IUCF in summer 1999 has been in steady use at Wayne State University for testing the performance of each individual scintillator tile in fully assembled STAR *barrel* EMC modules.

Collaboration between the barrel and endcap EMC groups on electronics design has also paved the way for several important features of the electronics for the endcap and its associated spin

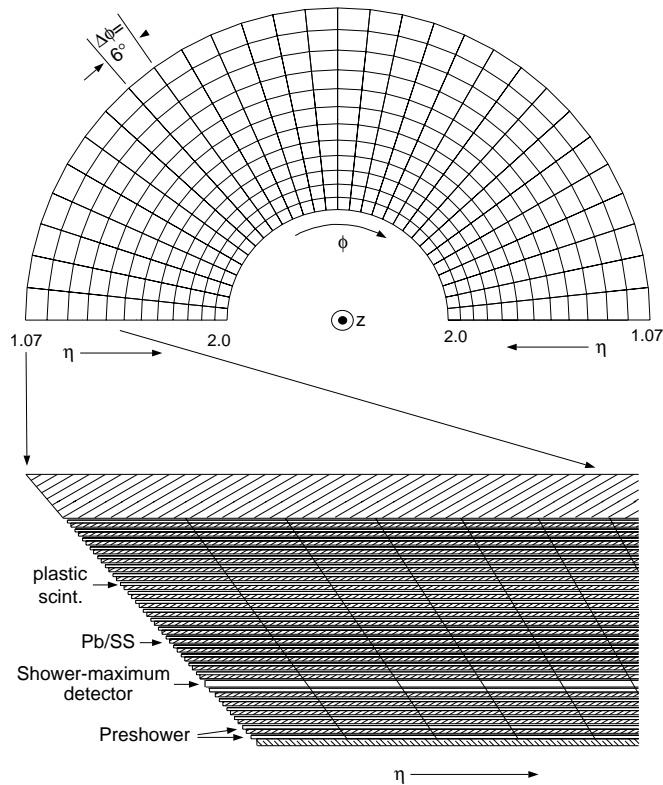


Figure 1: *Proposed tower structure of the EMC. Frame (a) shows the subdivision (into a total of 720 towers, half of which are shown) in pseudorapidity and azimuthal angle. Frame (b) indicates the depth profile of the projective towers, each with 23 layers of lead/stainless steel absorber and 24 layers of plastic scintillator. The two front scintillator layers from each tower are read out via two optical fibers, for use as a preshower detector. The space left for the shower-maximum detector (SMD) is indicated.*

physics research program. The Tower Data Collector being designed at IUCF already is made to accommodate readout of calorimeter towers from the endcap, as well as from the barrel. Allowance for readout of EMC data from beam crossings immediately before and after the one that fires the Level 0 trigger has been introduced to permit testing of algorithms that will select TPC tracks of interest even in the highest-luminosity pp running. The choice of scintillating strips for the endcap SMD, in contrast to the gaseous detector used in the barrel, demands changes in the SMD readout electronics between the two subsystems. Design of a fast amplifier for the endcap SMD, and a reworking of the readout boards to permit use of 12-bit ADC's to handle the greater endcap dynamic range, are under way. In the new design, the amplifiers for the 16 strips feeding each multi-anode PMT, the switched capacitor array to store output pulse heights for 128 consecutive beam crossings for each channel, and a common 12-bit ADC would all be built into the MAPMT bases.

We have followed up on a suggestion from the Conceptual Design Review by holding a mini-workshop on calorimeter calibration techniques at IUCF in September 1999. A full calibration scheme for the endcap has been developed as an outgrowth of that workshop. Critical to that calibration scheme is a newly designed laser monitoring system for both the tower and SMD scintillators. UV light from a single high-power pulsed laser will be injected directly into the scintillators via "leaky" optical fibers, to permit online monitoring of optical and electronic stability, linearity tests over the full dynamic range, transfer of absolute pre-calibrations determined with cosmic rays and test beams, and mockup of different energy *vs.* depth profiles in the calorimeter. The experience gained with cosmic ray calibrations of the prototype SMD also addresses some of the Review Committee's earlier concerns.

Considerable progress has been made on the development of a Level 3 trigger system for STAR

in general, and of TPC pileup rejection algorithms for high-luminosity pp running. By the end of 1999, the Level 3 group within STAR had installed and successfully operated the first phase of the processor farm, comprising 13 ALPHA processors communicating via a MYRINET interface. Twelve of the CPU's are used to reconstruct tracks from the hit information recorded within each of the 30° TPC sectors, while the 13th deals with global (cross-sector) trigger decision-making. Simulations carried out at IUCF have demonstrated the efficacy of a pileup rejection algorithm that can rapidly filter out TPC hit clusters associated with the majority of unwanted tracks, even for full luminosity ($\mathcal{L} = 8 \times 10^{31} \text{ cm}^{-2}\text{s}^{-1}$) pp running at $\sqrt{s} = 200 \text{ GeV}$. Extensive discussions have been initiated between the spin and Level 3 groups regarding the most efficient means to implement such an algorithm. A proposal will be presented from BNL to DOE in Spring 2000 for capital equipment funds to enhance the capability for high-luminosity pp triggering.

A variety of other simulations have been carried out in recent months to address hardware, triggering and analysis issues of importance to the spin physics program coupled to the EEMC. Further studies of the flagship experiment to detect $\bar{p} + \bar{p} \rightarrow \gamma + \text{jet} + X$ events have demonstrated that significant information regarding the integral gluonic contribution (ΔG) to the proton spin can be extracted for a variety of model gluon helicity distributions. Methods have been developed to correct ΔG for small systematic errors arising from simplifying assumptions made in the data analysis. The effects of higher-order QCD processes and of Q^2 -evolution of the parton distribution functions on the extraction of ΔG have been treated. The analysis of simulated W^\pm production has been improved to extract more detailed information on antiquark helicity distributions, and the implications of this analysis for resolution and linearity requirements on the EEMC have been considered. Simulations have been performed to assess the feasibility of two different approaches (involving dijet and Drell-Yan e^+e^- pair production, respectively) to attain sensitivity with STAR to *quark* polarizations at relatively high Bjorken x -values, in order to allow a calibration of STAR $\bar{p} + \bar{p}$ results against polarized deep inelastic scattering experiments.

Other simulations have addressed specific detector issues: the endcap tower and SMD strip occupancy arising from high- p_T jets; correlations between preshower and SMD information relevant to discriminating γ 's from π^0 's above 50 GeV; the severe impact on many aspects of the spin and p+A programs from a failure to complete the *full* barrel EMC. The latter simulations were carried out in preparation for a DOE review of the barrel EMC project in Spring 2000, at which STAR will request the remainder of the funding needed to complete the barrel.

The EEMC collaboration has been expanded and strengthened in several ways during recent months. A new group from Texas A&M University (Bob Tribble and Carl Gagliardi, with students and a post-doc) has expressed interest in joining and taking responsibility for the design and fabrication of PMT boxes to be mounted in the high-field environment on the back of the STAR poletip. This group brings to the project extensive experience and deep interest in probes of nucleon structure, experience from a similar PMT enclosure project they carried out for the MEGA collaboration at LAMPF, and the infrastructure of a DOE-supported cyclotron laboratory. Another strong and experienced group from Rutgers University is actively considering collaboration on the EEMC and spin physics program, pending approval from their university to replace a retiring nuclear physics faculty member. A positive response has been received from DOE regarding an increase in support for Hal Spinka's group at ANL, as needed for them to oversee the labor-intensive assembly and testing of the SMD modules. A number of recent visits from Dubna collaborators to the U.S. have been very instrumental in understanding results from the EEMC prototype detector tests, in choosing PMT's and designing bases. Additional Dubna collaborators will help in the preparation of optical fibers at MSU and in the SMD fabrication at ANL, over and above the substantial EEMC projects that will be carried out in Dubna.

The evolution in the EEMC collaboration and design, together with the establishment of a funding profile, lead to a revised management plan and resource-loaded timeline for the project, which are presented in Section 9 of this document. Consideration of the projects on the critical path for EEMC construction shows that a timely release of spending authorization, to permit placing significant equipment purchase orders by early Spring 2000, is essential to meet the goal of installing the first half of the EEMC in STAR during the summer shutdown in 2002. In contrast to the plan presented in the Conceptual Design Report, our current plan aims toward completion of the second half for installation in Summer 2003. We anticipate that the barrel EMC would also be completely installed on this time scale, and that full luminosity polarized proton collisions will be available at RHIC.

Sections 2-8 of this report present more detail on the developments summarized above and delineate the present status of the EEMC design and the initiation of its construction. Much of the work carried out over the past nine months has been stimulated by issues raised in the May 1999 review of the Conceptual Design. While detailed responses to these issues are presented throughout this report, we also summarize all the responses in the Appendix, for the benefit of the Review Committee.

2 New Physics Simulations

Many new simulations have been completed since the STAR endcap electromagnetic (EEMC) Conceptual Design Review. Included in this list are

- the calculation of the expected spin correlation, A_{LL} , for γ +jet coincidences with different model input for the gluon helicity asymmetry distribution, properly evolved to the Q^2 scales relevant at RHIC.
- the calculation of the expected background magnitude and the influence on A_{LL} measurements from γ + jet coincidences arising from partonic processes leading to two final state jets. These are so-called ‘fragmentation photon’ processes.
- the development of a procedure to reconstruct initial-state partonic kinematics for W^\pm production based on the measured four momentum of the daughter charged lepton.
- an improved understanding of the resolution of the TPC for reconstructing the transverse momentum and the sign of the curvature for $p_T=40$ GeV/c positron tracks in the pseudorapidity interval spanned by the EEMC.
- the development of a scheme to trigger at ‘level-0’ on e^+e^- pairs produced by the Drell-Yan process.
- the investigation of the use of quark/gluon fragmentation function differences in conjunction with phase space cuts to isolate partonic initial states that do not involve gluons (whose polarization is unknown) in di-jet production. The object of this study, and of the study of polarization effects in the Drell-Yan process, would be to ‘calibrate’ the RHIC-spin results against the existing data base of polarized deep inelastic scattering.
- the study of the occupancy in the EEMC towers and the SMD detector strips expected for different partonic subprocesses.
- the study of the performance of the EEMC calorimeter towers, accounting for expected variations in the thickness of the lead converters and the sampling scintillator sheets.

Some detail of this simulation work is provided in the sections below.

2.1 Sensitivity of γ +jet to $\Delta G(x)$

The existing data for scaling violations in polarized deep inelastic scattering provide only very loose constraints on $\Delta G(x)$. Several analyses of these constraints have been made [2, 3] and have generally concluded that the *integral* ΔG should be positive. The variation of the gluon helicity asymmetry distribution with the gluon momentum fraction (x_{gluon}) has significant differences in these different analyses. There is generally always a positive peak of $\Delta G(x)$, but the x_{gluon} value of the peak is not well constrained. Consequently, the gluon *polarization*, defined as the ratio $\Delta G(x)/G(x)$ can be either large or small, depending on where the peak in $\Delta G(x)$ occurs. In leading order perturbative QCD (pQCD), the spin correlation parameter (A_{LL}), that will be measured in $\vec{p}+\vec{p} \rightarrow \gamma+X, \gamma$ + jet + X reactions at RHIC, is proportional to the gluon polarization. As well, many parameterizations of $\Delta G(x)$ that are consistent with existing measurements result in negatively polarized gluons at some x_{gluon} values.

To better illustrate the utility of the γ + jet coincidence measurements planned for STAR, simulations using the three $\Delta G(x)$ models in Ref. [3] (hereafter referred to as GS sets A,B and C) have been performed. In all cases, the input $\Delta G(x)$ must be evolved [4] from the scale where the analysis was performed [3], $Q_0^2=4$ GeV², to the scales that will be probed at RHIC, taken to be $Q^2=p_{T,\gamma}^2/2$. The variation of the resulting gluon polarization with x_{gluon} for the three $\Delta G(x)$ models in Ref. [3], evolved to $Q^2=100$ GeV², is shown in Fig. 2.

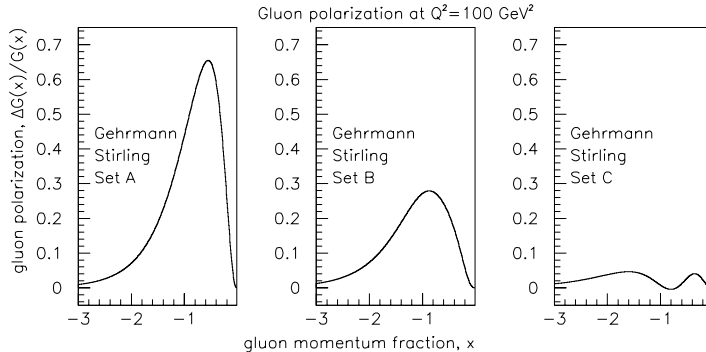


Figure 2: *Gluon polarizations computed from models of $\Delta G(x)$ consistent with polarized deep inelastic scaling violations [3]. The structure functions are evolved to the scales that will be probed at RHIC.*

The simulated spin correlation coefficient [5] expected for inclusive photon production in $\vec{p} + \vec{p}$ collisions at RHIC, using the GS-A,B and C models of $\Delta G(x)$, is shown in Fig. 3. The simulations include the subprocesses $fg \rightarrow f\gamma$ (where f refers to either a quark or an antiquark), $q\bar{q} \rightarrow g\gamma$ and $q\bar{q} \rightarrow \gamma\gamma$, hereafter referred to as ‘direct photon’ processes. The first of these subprocesses provides $\sim 90\%$ of the photon yield. The magnitude of the calculated A_{LL} in the pseudorapidity range covered by the STAR EEMC is larger than at midrapidity, as expected since the endcap selects events having more asymmetric gg collisions and having partonic scattering angles where \hat{a}_{LL} (the pQCD result for the partonic spin correlation coefficient) is large. The predicted decrease in A_{LL} as one goes from GS set A, to set B and then set C for $\Delta G(x)$, simply reflects the smaller gluon polarization vs x_{gluon} in those three models (Fig. 2).

As discussed elsewhere [5, 1], STAR will be able to detect a significant fraction of the away-side jets in coincidence with the produced photon. This capability results from the large phase space coverage of the existing time-projection chamber and the planned electromagnetic calorimetry. Detection of γ +jet coincidences enables the reconstruction of the initial-state partonic kinematics [5]. With this capability, a direct extraction of $\Delta G(x)$ can be made from the measured A_{LL} , assuming contributions from only quark-gluon Compton scattering and collinear initial-state parton collisions. Background contributions from $\pi^0(\eta)$ production that are not eliminated by either the shower-shape analysis performed on the SMD data or by isolation cuts, can be subtracted from the measured values. There remain small contributions to the γ +jet yield from partonic subprocesses other than quark-gluon Compton scattering. The $q\bar{q}$ annihilation contribution can be corrected for based on simulations. Fig. 4 shows the directly extracted $\Delta G(x)$ from the simulated A_{LL} values, after applying an additive correction for $q\bar{q}$ annihilation. A 320 pb⁻¹ sample at $\sqrt{s} = 200$ GeV and a 800 pb⁻¹ sample at $\sqrt{s} = 500$ GeV have been combined in the figure. These data samples can be

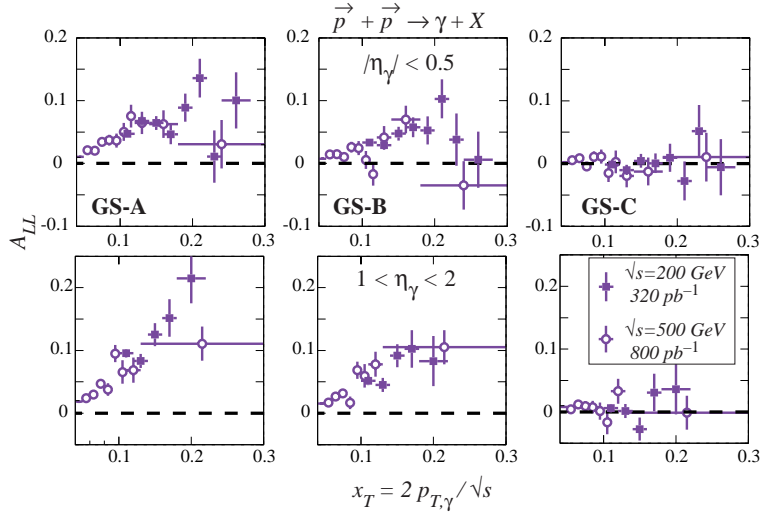


Figure 3: *Simulated values for A_{LL} for inclusive photon production at RHIC energies. The top row shows the spin correlations for midrapidity photons that can be detected at both PHENIX and STAR. The bottom row show expected values at the forward angles probed by the STAR EEMC. Not evident in this figure, is that for a given x_T , photons detected in the EEMC correspond to smaller- x gluons than those detected at midrapidity.*

achieved in two ten week runs, based on the projected luminosity for $\vec{p} + \vec{p}$ collisions. The latter is especially crucial to extend the coverage to small x_{gluon} values. To ascertain the sensitivity STAR will have to the fraction of the proton's spin carried by gluons (or, the *integral* ΔG), the results in Fig. 4 were fitted to a standard structure function parameterization [3], with the coefficients specifying the large- x variation fixed. The resulting fitted value for η represents the integral ΔG .

Beyond illustrating the sensitivity of STAR to the fraction of the proton's spin carried by gluons, Fig. 4 illustrates several other things.

- *an accurate determination of ΔG will require both $\sqrt{s}=200$ and 500 GeV data samples to get to sufficiently small x_g .* Due to strong correlations between η and a (specifying the small x behavior of $\Delta G(x)$), $\delta\eta$ grows rapidly as the low- x points are successively eliminated. It is critical to observe the falloff of $x\Delta G(x)$ with decreasing x to ensure an accurate determination of η .
- *the large- x behavior of $\Delta G(x)$ must be constrained to determine the integral ΔG at RHIC.* The fixed parameters in the above analysis presuppose that the large x behavior of $\Delta G(x)$ is known. As discussed in Sect. 8.4, the *full* barrel electromagnetic calorimeter is critical to cover phase space regions for γ +jet coincidences that will provide overlap with other planned experiments (COMPASS [6]) that will measure the large x behavior of $\Delta G(x)$.
- *fitting $\Delta G_{recon}(x)$, including only the corrections for $q\bar{q}$ annihilation, yields a value for the fitted η that is too small compared to the input ΔG .* The present analysis neglects several other corrections, including evolving all of the $\Delta G_{recon}(x)$ points to a common Q^2 and correcting for the kinematic reconstruction errors, because they require knowledge of $\Delta G(x)$ and hence will require an iterative approach to deduce the result. Even when making these corrections, the fitted η , although closer to the input value, is still too small. The largest remaining

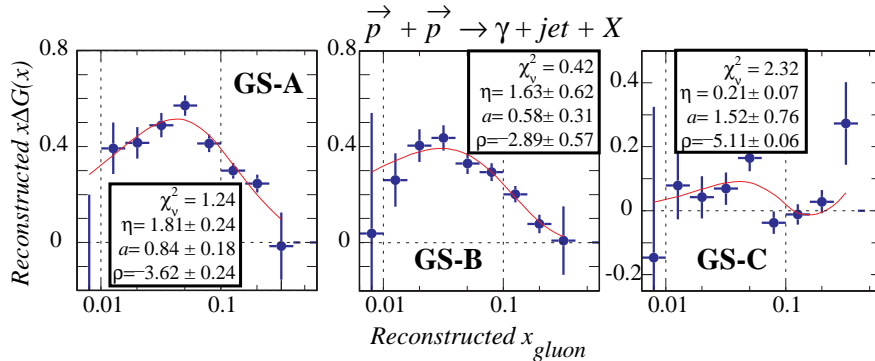


Figure 4: Fits to the reconstructed $\Delta G(x)$ directly reconstructed from the simulated A_{LL} for γ +jet coincidences, after correcting for $q\bar{q}$ annihilation. A standard parameterization is used to fit the data, with the parameters specifying the large x_{gluon} behavior fixed. Full data sets for $\sqrt{s}=200$ (500) GeV are assumed, corresponding to integrated luminosity of 320 (800) pb^{-1}

error comes from neglecting the transverse momentum (k_T) of the partons in the initial state. Repeating the analysis with simulations that don't include initial-state parton showers (and hence do not include k_T smearing) results in a fitted η in agreement with the input ΔG .

The end result is, that after accounting for the most significant sources of systematic error [1], we expect that the fraction of the proton's spin carried by gluons can be determined to an accuracy of approximately 0.5, primarily based on the STAR measurements of $\vec{p}+\vec{p} \rightarrow \gamma+\text{jet}+X$. Data samples at both $\sqrt{s}=200$ and 500 GeV are crucial so that the accuracy is not limited by extrapolation errors. The analysis of $\Delta G_{recon}(x)$ presented here is intended to illustrate the sensitivity of the STAR measurements to the integral ΔG . Clearly, the best determination of ΔG will result from a global analysis of all relevant data.

2.2 'Fragmentation photon' background to γ +jet coincidences

As predicted by several studies [7], photons produced in the fragmentation of final state recoiling partons present an important background to 'direct photon' studies. The impact of these so-called 'fragmentation photons' on the measurement of γ +jet coincidences at STAR has been ascertained using PYTHIA [8]. Reliable results are expected from the simulated 'fragmentation photon' yield, since the $p + \bar{p} \rightarrow \gamma + 2 \text{ jet} + X$ yield measured by CDF [9] is well represented by PYTHIA.

The 'fragmentation photon' yield is obtained by considering all $2 \rightarrow 2$ subprocesses, responsible for the bulk of the non-diffractive inelastic cross section, and searching for those events that have an energetic photon that is not produced by the decay of any parent hadron. The events are analyzed after accounting for STAR detector resolutions and acceptances by applying a jet finder and imposing the UA2 isolation condition [10]. Naively, the latter is expected to effectively eliminate 'fragmentation photons', because of the additional hadrons expected within a cone around the photon. Unfortunately, the hardest photons result from bremsstrahlung, and are widely displaced from the core of the jet produced by the radiating parton. The end result is that a significant fraction of the overall $\gamma + \text{jet}$ yield will arise from 'fragmentation photons'. The comparison between this yield and the 'direct photon yield' (defined in the previous section) is shown in Fig. 5. It is possible that an improved isolation condition, beyond the one employed by UA2, can reduce the 'fragmentation photon' yield beyond that shown in the figure.

$p + p \rightarrow \gamma + \text{jet} + X$ $\sqrt{s} = 200 \text{ GeV}$ 75 pb^{-1} (PYTHIA 5.7)
(includes UA2 isolation condition)

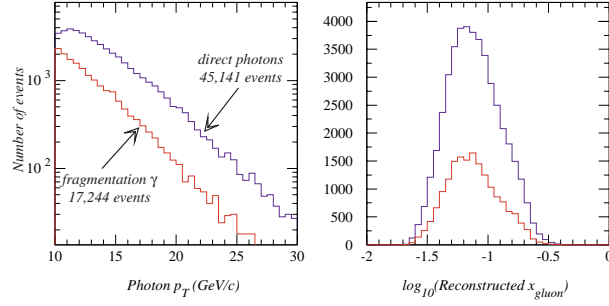


Figure 5: Comparison between the ‘direct’ and ‘fragmentation’ $\gamma + \text{jet}$ yield that is expected to be observed with the STAR detector. Direct photons are those produced in hard scattering events, predominantly quark-gluon Compton scattering. Fragmentation photons are produced in the fragmentation of recoiling final state partons. It is possible that a more restrictive isolation condition will reduce the contribution from fragmentation photons.

What impact does this background process have on the planned measurement of $\Delta G(x)$? This question was addressed by calculating the A_{LL} for $\vec{p} + \vec{p}$ collisions including both ‘direct’ and ‘fragmentation’ photon processes. The hard scattering partonic spin correlations for all contributing subprocesses were employed in the calculation. The result for A_{LL} is shown in Fig. 6, comparing ‘direct photon’ production alone to a calculation combining direct and fragmentation photons. The input $\Delta G(x)$ corresponds to GS set A [3]. A small dilution of A_{LL} is observed from fragmentation photons. Either improved isolation cuts or a more sophisticated analysis of the event topology is expected to reduce the dilution of the direct photon A_{LL} . The relative importance of the dilution will increase as the gluon polarization decreases.

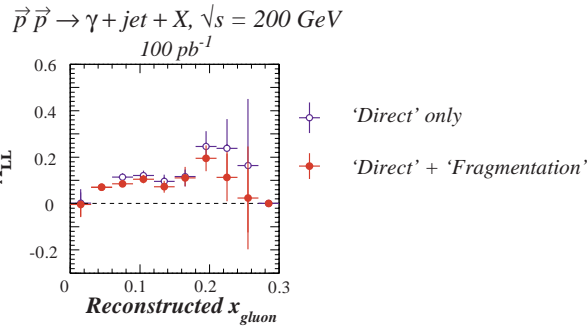


Figure 6: Calculated A_{LL} for $\vec{p} + \vec{p}$ collisions at $\sqrt{s} = 200 \text{ GeV}$ for ‘direct photon’ production only versus ‘direct + fragmentation’ photon production. The sizeable yield of ‘fragmentation photons’ produces a small dilution of A_{LL} .

2.3 Partonic kinematics reconstruction in W^\pm production

To achieve the goal of determining the unpolarized and polarized parton distribution functions

of the nucleon, the variation of these probabilities with Bjorken x , interpreted as the fraction of the nucleon's longitudinal momentum carried by the parton, and the scale, Q^2 is required. In many cases, this x and Q^2 dependence is deduced from a theoretical interpretation of experimental observables. The impact of the measurement errors on the deduced structure functions can be best ascertained if these critical kinematic variables can be *directly deduced* from the experiment. For the case of determining the gluon polarization within the proton, γ +jet coincidences provides the necessary kinematic determination. This section discusses how the x and Q^2 dependence of the polarization of sea antiquarks in the proton can be deduced from $\vec{p} + \vec{p} \rightarrow W^\pm + X$, by detecting only the daughter charged lepton from W^\pm decay. The relevance of this to the design of the STAR endcap electromagnetic calorimeter (EEMC) is the constraint this procedure imposes on the energy resolution of the calorimeter.

The Standard Model predicts that W^\pm bosons are predominantly produced in $p + p$ collisions by the partonic processes $u + \bar{d} \rightarrow W^+$ and $d + \bar{u} \rightarrow W^-$, at leading order in perturbation theory. Given the $V - A$ theory of the weak interaction, sizeable *parity violating* longitudinal spin asymmetries, A_L , are expected in $\vec{p} + p$ collisions [11]. These asymmetries can be related to the polarized and unpolarized parton distribution functions, and in certain kinematic domains are directly proportional to either quark or antiquark polarizations [1] (*ie.*, the ratio of the structure functions $\Delta f(x)/f(x)$, where f represents either q or \bar{q}). Since the partonic constituents of the proton are assumed to have negligibly small transverse momenta, the produced W^\pm bosons should be collinear with the colliding protons. Higher-order gluon radiation [12] results in non-zero, but small, values for the W^\pm transverse momentum, defined as q_T .

If the W^\pm transverse momentum is zero, then by simply measuring the angle and energy of the daughter charged lepton, the Bjorken x values for the interacting q and \bar{q} can be directly deduced, with the further assumption that the small decay width of the W^\pm can be ignored. In a real experiment, q_T can be ignored if it is small compared to the W^\pm longitudinal momentum, $p_{L,W}$. Conveniently, the region of phase space where A_L can be most directly related to the quark and antiquark polarization corresponds to asymmetric $q + \bar{q}$ collisions, resulting in large $p_{L,W}$. When $p_{L,W}$ is large, q_T can assumed to be zero. The accuracy of this initial-state partonic kinematics reconstruction is shown in Fig. 7. In that figure, $p + p \rightarrow W^\pm$ events at $\sqrt{s}=500$ GeV are generated by PYTHIA [8]. The parton shower model is used to simulate the higher-order QCD effects producing non-zero q_T . Event selection requires that a e^+ or e^- be within the acceptance of the STAR barrel and endcap EMC and have $p_{T,e} \geq 10$ GeV/c. Perfect detector resolution is assumed. The finite accuracy in the partonic kinematics reconstruction results from the simplifying assumptions used in the analysis.

The critical assumption that q_T is small works best when the daughter e^\pm from W^\pm decay is detected away from midrapidity ($|\eta| \approx 0$). The reason for this is that most of the e^\pm at large η are produced from W^\pm created in asymmetric $q + \bar{q}$ collisions [1]. These asymmetric collisions provide a sizeable longitudinal momentum to the W , $p_{L,W} = \beta_{pCM} \gamma_{pCM} M_W c$, where the partonic center of momentum (pCM) is moving with velocity equal to $\beta_{pCM} c$ and $\beta_{pCM} = (x_1 - x_2)/(x_1 + x_2)$ in the collider reference frame. The momentum fractions of the q and \bar{q} are denoted as x_1 and x_2 . When the daughter e^\pm are detected near $|\eta| \approx 0$, the reconstruction procedure fails because $p_{L,W}$ is generally small, and q_T can no longer be ignored. Events with large $|\delta x_{max(min)}| = |x_{max(min)}^{sim} - x_{max(min)}^{recon}|$ for e^\pm having $\eta > 0$ arise for several reasons: (1) events with sizeable q_T are predicted to occur by PYTHIA even when the daughter e^\pm is detected at $\eta > 0$, (2) the mass distribution of the W can result in events with M_W significantly different from its central value of 80.4 GeV/c², and (3) some of the daughter e^\pm can be produced by the decay chain $W^\pm \rightarrow \tau^\pm + \nu_\tau \rightarrow e^\pm + \nu_e + \nu_\tau$ meaning that the W rest energy is shared between three, rather than two, final state particles. Some degree

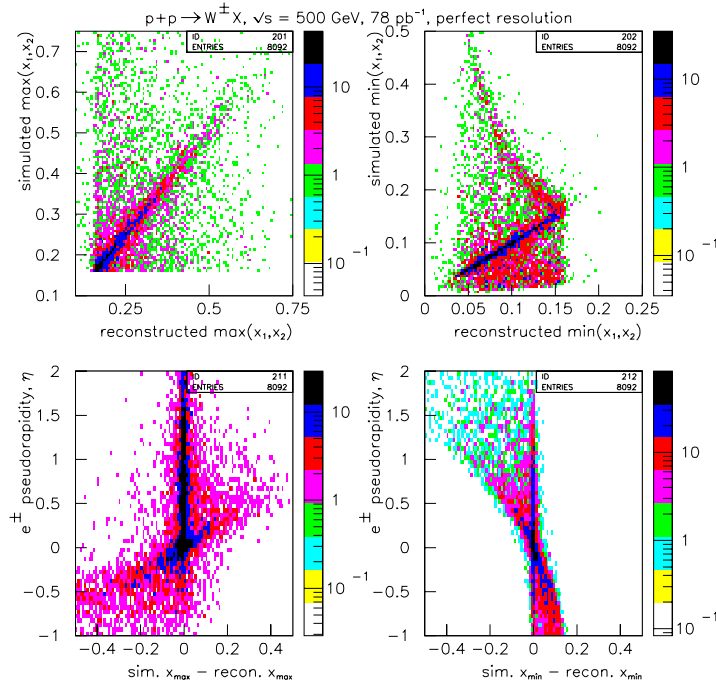


Figure 7: (Top) Simulated versus reconstructed Bjorken x values for the quark and antiquark that form the W^\pm in $p + p$ collisions. The reconstruction ignores the transverse momentum of the W (q_T). (Bottom) The difference between simulated and reconstructed x value versus the pseudorapidity of the daughter e^\pm produced by W^\pm decay. The e^\pm detected at midrapidity are mostly produced by W s with small positive or negative longitudinal momentum. The initial-state kinematics reconstruction fails at midrapidity because q_T is not ignorable. The reconstruction procedure is most successful away from midrapidity.

of ambiguity will also arise in the assignment of $x_{max(min)}$ to the interacting q and \bar{q} . For most of the events x_{max} will correspond to x_q and x_{min} to $x_{\bar{q}}$. Even with all of these problems, it is expected that initial-state partonic kinematics deduced in this manner for W^\pm production will be valuable.

The influence of q_T on the kinematics reconstruction can be minimized by imposing a cut on both η_e and $p_{T,e}$. The correlation of $\delta x_{max(min)}$ with $p_{T,e}$ is shown in Fig. 8. The large- p_T edge of the $p_{T,e}$ distribution is known to be most sensitive to q_T [13].

What impact does any of this have on the design of the EEMC? The answer is that the finite resolution of the EEMC will contribute a comparable amount to the kinematics reconstruction resolution as do the systematic errors inherent to the procedure. This is most apparent by fitting the narrow peak in the $\delta x_{max(min)}$ distribution with a Gaussian function, ignoring the small background in the distribution displaced from the narrow peak. That background originates from the sources listed above. The variation of the Gaussian σ with $p_{T,e}$ is also shown in Fig. 8. A finite energy resolution corresponding to $\sigma_E/E = 0.02 + 0.16/\sqrt{E}$ is assumed for the EEMC in the analysis. With this resolution, the Gaussian σ for $p_{T,e} < 30$ GeV/c is $\approx 30\%$ larger than for ‘perfect’ energy resolution. Hence, the partonic kinematics reconstruction for W production imposes a requirement

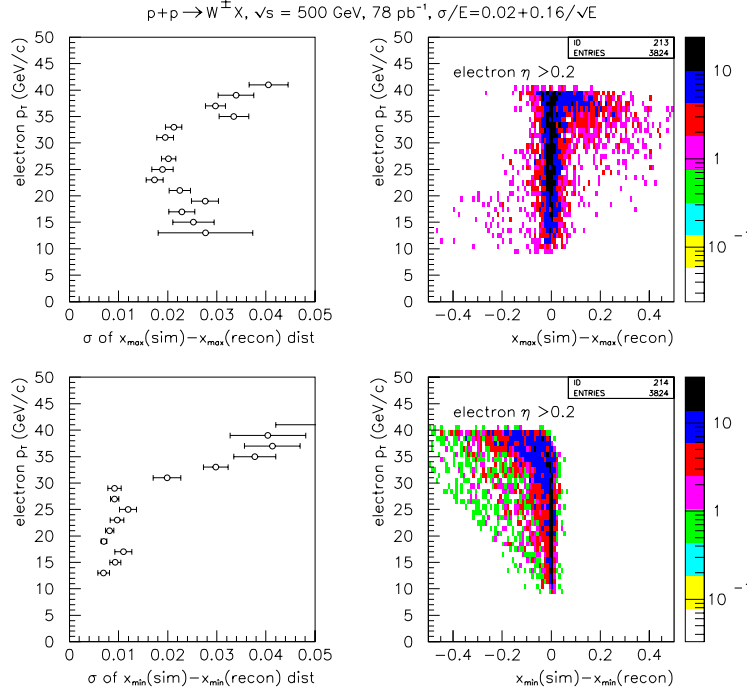


Figure 8: *The partonic kinematic reconstruction errors are correlated with $p_{T,e}$. The largest $p_{T,e}$ are most sensitive to q_T . For $p_{T,e} < 30$ GeV/c, the planned EEMC resolution of $\sigma_E/E = 0.02 + 0.16/\sqrt{E}$ contributes a comparable amount to the resolution of the kinematics reconstruction as the systematic errors in the reconstruction, thus imposing a requirement on the EEMC performance.*

on the energy resolution of the EEMC.

Another important simulation [14] relevant to the STAR W physics program has been recently performed. The detection of daughter e^\pm in the pseudorapidity interval spanned by the EEMC is complicated by the rolloff in the TPC acceptance. This rolloff results in shorter tracks as $\eta \rightarrow 2$ which may impair the ability to distinguish the curvature difference between e^- and e^+ .

A simulation of the TPC response to single positron tracks with $p_T = 40$ GeV/c was conducted [14]. The simulation models the expected response of the STAR TPC from the extensive understanding of previously built TPCs. The existing STAR tracking software was then used to reconstruct tracks, using reconstructed space points from the TPC simulation and the event origin. Fitted track parameters include the sign of the electric charge and the transverse momentum of the particle. The result is that the probability for reconstructing the wrong sign for the electric charge is vanishingly small in the $1 < \eta < 1.5$ interval. Even for events in the interval $1.5 < \eta < 2$, there is only a 10% probability for improperly reconstructing the sign of the charge. This result can probably be improved by including in the fit the space point from the EEMC SMD, and by constraining the fitted p_T for the track to agree with the EEMC energy measurement.

2.4 Sensitivity to quark polarization: Drell-Yan and high- p_T dijets

To make contact with the extensive body of polarized deep-inelastic scattering (PDIS) data, it is desirable to find ways to diminish the importance of $g+g$ and $q+g$ subprocesses in $\vec{p}+\vec{p}$ collisions, since the gluon polarization is unknown. A simulation study has been conducted to examine if the spin dependence of di-jet production in $\vec{p}+\vec{p}$ collisions at $\sqrt{s} = 200$ GeV can be used for this purpose. The isolation of $q+q'$ subprocesses was examined by exploiting differences in the fragmentation functions of final-state quarks and gluons. Recent data from the experiments at LEP suggests significant differences in these fragmentation functions, although, at present, event generators have not been ‘tuned’ to fully reproduce the data. With the PYTHIA generator, it is found that jets containing leading π^0 s, that carry a significant fraction of the jet momentum, predominantly arise from quark fragmentation. Further suppression of subprocesses involving gluons can be obtained by detecting di-jets having large invariant masses.

Another possible way of making contact with the PDIS data base is to study the Drell-Yan process. The large acceptance of the barrel and endcap EMC at STAR make it ideally suited to that task. Initial simulation studies of the feasibility of triggering on $p+p \rightarrow e^+e^-$ events arising from the Drell Yan process have been completed. It was found that by demanding a pair of spatially separated ‘high towers’ from the barrel and endcap EMC, the background rate from jets containing energetic neutral mesons is reduced to a level compatible with the level-0 trigger rate requirements and the efficiency for triggering on e^+e^- pairs (where both the e^+ and e^- are within the STAR acceptance) with invariant mass greater than $4.5 \text{ GeV}/c^2$ is greater than 40%. The specific conditions used in the simulation required finding the ‘high tower’, with a transverse energy greater than 3 GeV, and the ‘second highest tower’ with a transverse energy greater than 2 GeV. With these conditions, the background L0 trigger rate is 28 Hz, at $\sqrt{s} = 200$ GeV for the expected luminosity of $0.8 \times 10^{32} \text{ cm}^{-2} \text{ sec}^{-1}$. It remains to be established if these conditions can be programmed within the DSM boards of the level-0 trigger that are planned for both the BEMC and the EEMC. If so, or if a comparably effective level-0 trigger can be defined, then an exciting program of studies of Drell-Yan production in $\vec{p} + \vec{p}$ will be possible.

Neither of these programs impose any special requirements on the construction of the EEMC or SMD. Both programs are only feasible to consider if the barrel EMC construction is completed, so that the BEMC covers the pseudorapidity interval, $-1 \leq \eta \leq +1$.

2.5 Simulated performance of the EEMC and SMD for $p+p$ collisions

A GEANT model of a design of the EEMC and the planned triangular cross section SMD has been created. The particles arising from the primary interaction as generated by PYTHIA [8] are transported through a simplified model of the STAR magnet to the EEMC. GEANT is used to simulate showers in the EEMC from these particles. Although this simulation does not include secondaries produced between the primary vertex and the EEMC, it is expected that it will predict the occupancies in the EEMC towers and the SMD strips to an accuracy of $\sim 20\%$. With this model many aspects of the overall performance of the EEMC, and indications of the complexities in the global event analysis for $p+p$ collisions, can be obtained.

The first issue to address is the occupancy of the towers of the EEMC and the strips of the SMD. This issue was addressed by considering partonic subprocesses contributing to the $p+p \rightarrow \text{jet} + X$ yield at $\sqrt{s} = 200$ GeV. The events were generated with a threshold on the partonic transverse momentum of 8 GeV/c, since the direct photon studies will be confined to $p_{T,\gamma} > 10$ GeV/c to ensure the applicability of perturbative QCD. Events were selected that resulted in a single tower of the EEMC having an effective transverse energy of 5 GeV. This ‘high-tower threshold’ is planned

as one component of the STAR level-0 trigger for the photon studies. A count of the EEMC towers within each event that have energy deposition of at least 10 MeV, corresponding to roughly half the energy deposited by a minimum ionizing particle (MIP), was made. A similar count was made for the SMD strips. The simulation of the strip response converted the energy deposition, as calculated by GEANT, into an expected number of photoelectrons by assuming that a MIP yields, on average, two photoelectrons when traversing the triangular cross section strip along the shortest line connecting the apex to the base. Cross talk on the multi-anode photomultipliers was not included in this simulation. A count of all strips having more than one photoelectron in a single event was made. The resulting multiplicity distributions are shown in Fig. 9.

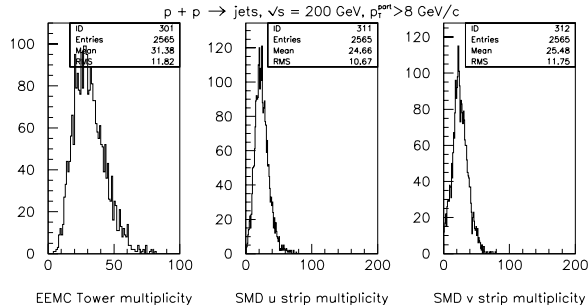


Figure 9: *Multiplicity of towers and strips expected for $p+p \rightarrow jets$ at $\sqrt{s}=200$ GeV. Towers were counted that had deposited energy of 10 MeV or greater (approximately half the energy deposited by a MIP). Strips were counted that had a simulated yield of more than 1 photoelectrons.*

One may be tempted to conclude from Fig. 9 that either the number of EEMC towers or SMD strips could be reduced without creating too great an impact on the physics results. This conclusion is inaccurate because the average tower multiplicity does not set the requirement on the EEMC segmentation. A much more severe requirement is imposed by considering the particle multiplicity within the ‘high tower’ that will trigger the event readout. This is shown in Fig. 10 for jet production in $p+p$ collisions at $\sqrt{s} = 500$ GeV, the primary physics background that will be encountered in trying to reconstruct daughter e^\pm produced in the decay of W^\pm bosons. The most probable particle multiplicity of 2 in the high tower arises from photon pairs produced in the decay of a leading $\pi^0(\eta)$ meson. These are not problematic events for W physics, assuming that the tracking efficiency of the TPC is adequate to reliably identify ‘neutral high towers’. The problem arises for larger particle multiplicities within a single EEMC tower. There is a significant probability ($> 20\%$) that EEMC towers will be intercepted by both energetic photons *and* charged particles. Based only on the correlation between the EEMC tower information and the TPC tracks these events would create a significant background for reconstructing e^\pm produced by W^\pm decay. Coarser granularity in the EEMC towers would clearly make this much worse.

Good performance from the EEMC SMD is required to distinguish daughter e^\pm arising from W^\pm decay from the jet background where a charged particle falls in the same tower as an energetic photon pair. The SMD response will need to be correlated with the projected track from the TPC. If the track has a ‘well formed’ SMD peak in the vicinity of the EEMC tower intercept, it would be identified as an energetic electron. The background events will have multiple peaks in the SMD profile created by the photon pair arising from $\pi^0(\eta)$ decay, and possibly an additional small peak(s) from the most likely MIP response of the SMD to the charged hadron(s). To develop

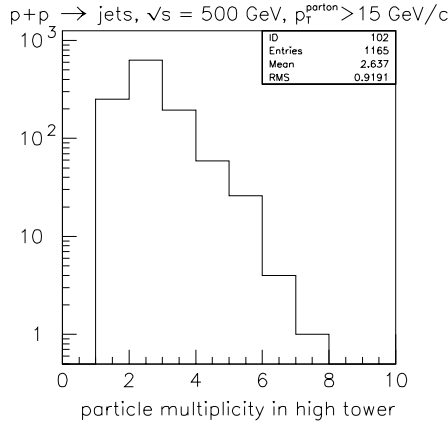


Figure 10: Number of particles from the primary vertex that contribute $>5\%$ of the energy deposited in the EEMC tower with the largest transverse energy. Jet production is the primary source of background for detecting daughter e^\pm from the decay of W^\pm bosons produced in $p + p$ collisions at $\sqrt{s} = 500$ GeV. Coarser granularity of the EEMC towers would increase the already large probability for a charged hadron to intercept the same tower as an energetic photon pair, produced in the decay of $\pi^0(\eta)$ mesons. Such events require a careful treatment to avoid misidentifying them as energetic electrons.

the necessary ‘electron finder’, more complete simulations of the EEMC and SMD performance, in conjunction with a full simulation of the STAR TPC response, are required. The recent development of an EEMC and SMD model within the STAR software framework by the Dubna group is a step towards that goal. Ultimately, simulations of $p + p \rightarrow W^\pm + X$ events, in the presence of the considerable pileup of minimum bias events, are required to establish if the TPC track recovery efficiency is adequate to eliminate this background.

It should be noted that the particle multiplicity in the EEMC high tower is not as problematic for determining the gluon polarization via γ +jet coincidences, because the photon p_T is, in general, substantially smaller than the transverse momentum of e^\pm produced by W^\pm decay. The jet background at these smaller p_T values will have a lower particle density surrounding the leading particle. This will result in much smaller probabilities for multiple particle pileup in a single EEMC tower. Furthermore, the photon physics program requires identifying neutral EMC ‘high towers’. Charged particle pileup in a neutral high tower should be eliminated by projecting the TPC track to the tower. This would result in an inefficiency, rather than a background, for photon physics.

As discussed above for the EEMC towers, the required granularity of the SMD is also not set by a simple occupancy argument. Instead, the SMD profiles from electromagnetic showers must involve a large enough number of strips to enable the required $\gamma/\pi^0(\eta)$ discrimination via the shower shape analysis [1]. We envision fitting the shower profiles for each event. Accurate peak fits require a minimum of five points. Inevitably, given the fluctuations in the longitudinal and transverse shower profiles in response to incident photons, some events will have a very small number (even zero) of strips having measureable pulse height. For the vast majority of the photon showers, the photoelectron yield and transverse dimensions of the strips determine the number of strips involved in a given event. The presently designed granularity of the SMD strips is adequate for the shower shape analysis, as shown in Fig. 11.

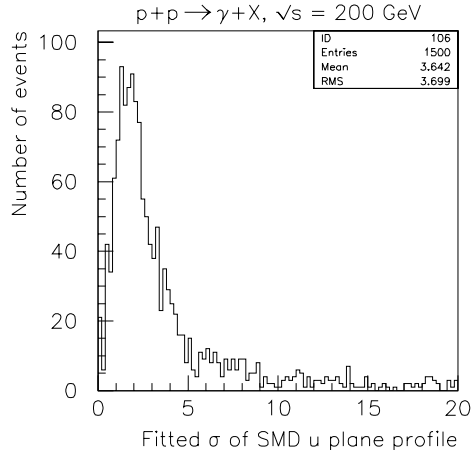


Figure 11: *Fitted σ (in units of number of strips) for the SMD u -plane shower profile for incident high- p_T photons. An accurate shower-shape analysis requires at least 3, and preferably 5, strips to have measurable pulse height. This requirement prevents the design of a SMD with coarser segmentation.*

The final question addressed with this model of the EEMC and SMD and a simplified treatment of the TPC response was raised at the EEMC Conceptual Design Review. Can the EEMC preshower response be correlated with the shower-shape analysis of the SMD response to provide an event sample enriched in ‘direct photons’ and a separate sample enriched in di-photons arising from $\pi^0(\eta)$ decay? This is particularly relevant to obtain measurements at the same x_{gluon} , but different Q^2 , from γ +jet coincidence data obtained at two collision energies, $\sqrt{s} = 200$ and 500 GeV. To get overlapping values of x_{gluon} , it is necessary to reliably detect photons with $p_T > 20$ GeV/c at $\sqrt{s} = 500$ GeV. At $\eta=1.5$, $p_T = 20$ GeV/c corresponds to a 47 GeV photon, an energy where the opening angle between the photon pairs arising from $\pi^0(\eta)$ decay is sufficiently small that the shower shape analysis begins to fail [1].

To answer this question it is necessary to consider both isolation conditions and the response of the EEMC preshower detector and the SMD. An improved understanding of very high- p_T events (> 30 GeV/c) suggests that the ability to impose isolation cuts will be affected by the sizeable number of hadrons near the jet axis. Distinguishing individual particle clusters within the BEMC, and especially the EEMC because of the coarser granularity, will be difficult. The lack of hadronic calorimeters at STAR is nominally compensated for by the p_T measurement of charged hadrons performed by the TPC. Unfortunately, the increased hadronic density near the jet axis makes it difficult to correct the measured EMC tower energies for hadronic showers. Without this correction, which *can be made at lower p_T* , the distinction between single (isolated) photons and jets containing a leading $\pi^0(\eta)$ via isolation cuts is compromised. This problem must be understood more thoroughly before the question raised at the CDR can be answered. It is hoped that the necessary understanding will be available by the time of the upcoming review.

2.6 EEMC tower performance

A study of the impact on the resolution and linearity of the EEMC caused by thickness variations in the lead sheets and scintillator layers, and by layer-to-layer variations in the light yield from the sampling scintillator, has been started. Based on one randomized configuration of lead and scintillator thicknesses, GEANT simulations of the EEMC tower response to single photons and electrons in the energy range between $1 \leq E \leq 100$ GeV were performed. The analysis of those results suggests that with the thickness tolerances planned for the lead and scintillator that will be used in the EEMC construction, as discussed in the following sections, the requisite resolution and linearity of response required for the STAR spin physics program can be achieved. More complete results will be available at the upcoming review.

3 Prototype Detector Construction and Testing

A crucial element to the successful measurement of the gluon helicity-dependent structure function ($\Delta G(x)$) at STAR, via the study of $\vec{p} + \vec{p} \rightarrow \gamma + \text{jet} + X$ at \sqrt{s} values up to 500 GeV at RHIC, is the discrimination between single photons and di-photons arising from the decay of the copiously produced $\pi^0(\eta)$ mesons. One of the primary methods planned for this discrimination is to employ a triangular cross section, scintillator-strip shower-maximum detector (SMD) to measure the transverse profile of showers produced in the STAR Endcap Electromagnetic Calorimeter (EEMC) [1]. Although the SMD is similar in design to the D0 preshower detectors [15], presently under construction, there are critical differences that require testing a prototype of the SMD, planned for the STAR EEMC. Tests are important to establish whether the average shower profile and the event-to-event fluctuations of the SMD response are properly modeled by the simulations [1]. Existing simulations suggest that the SMD will provide 80% suppression of the $\pi^0(\eta)$ background expected in the EEMC, while retaining 80% of the photon signal, for $p + p$ scattering events at STAR.

This section provides a status report of the present understanding of an in-beam test of a prototype calorimeter, including two orthogonal planes of a prototype shower maximum detector (pSMD), constructed from triangular cross section scintillator strips. The pSMD was positioned after ~ 5 radiation lengths of lead converter sheets in the calorimeter. A brief description of the construction of the 12 tower sampling calorimeter and the pSMD is provided. A description of the setup and tests of the prototype in the Final Focus Test Beam at SLAC is given. Finally, preliminary results from SLAC test beam run T-438 on the performance of the pSMD are presented.

3.1 Description of the prototype calorimeter

The design of the prototype calorimeter is modeled after an earlier conceptual design of the STAR EEMC [1]. It is a layered lead and scintillator sampling calorimeter, with a sampling fraction of 6.5%. There are 24 lead radiators in the calorimeter. Each radiator is 5 mm thick and was produced by Vulcan Lead. This stack differs from the EEMC by one extra lead layer. It was included in the prototype to account for the material upstream of the EEMC in the STAR detector. The first 2 scintillator layers were 5-mm thick Kuraray SCSN-81 scintillator. The last 22 scintillator layers were all 4-mm thick SCSN-81. The extra thickness of the first two layers will allow their use as preshower detectors. In the EEMC, two wave-length shifting (WLS) optical fibers will be inserted in the tiles of the first two scintillator layers. One fiber will transmit scintillation light to the ‘tower’ photomultiplier tubes (PMT), and the second fiber will transmit light to independent PMT for use as ‘preshower’ readout. In the prototype calorimeter, only a single WLS is used, at present. The lead and scintillator layers of the prototype were held in place by spacer grooves machined in aluminum bars. The entire assembly was housed in a light-tight aluminum box.

The scintillator sheets of the prototype had machined ‘isolation’ grooves, subsequently filled with titanium dioxide loaded epoxy, to provide optical isolation for the 12 tiles in each sheet. The 12 tiles in a sheet formed a 3×4 pattern, resembling an 18° section of an earlier design of the STAR EEMC near the inner radius of the detector, as shown in Fig. 12. When stacked, the isolation grooves within the 24 scintillator megatiles formed a ‘projective tower’, pointing at an origin upstream of the detector by 270 cm, again similar to the design of the EEMC. The final step in the machining of the scintillator megatiles was to cut a σ groove, into which a WLS fiber is inserted for light collection. After machining, the scintillator megatiles were wrapped in two layers of white paper to diffusely reflect scintillation light escaping from the surface of the sheets.

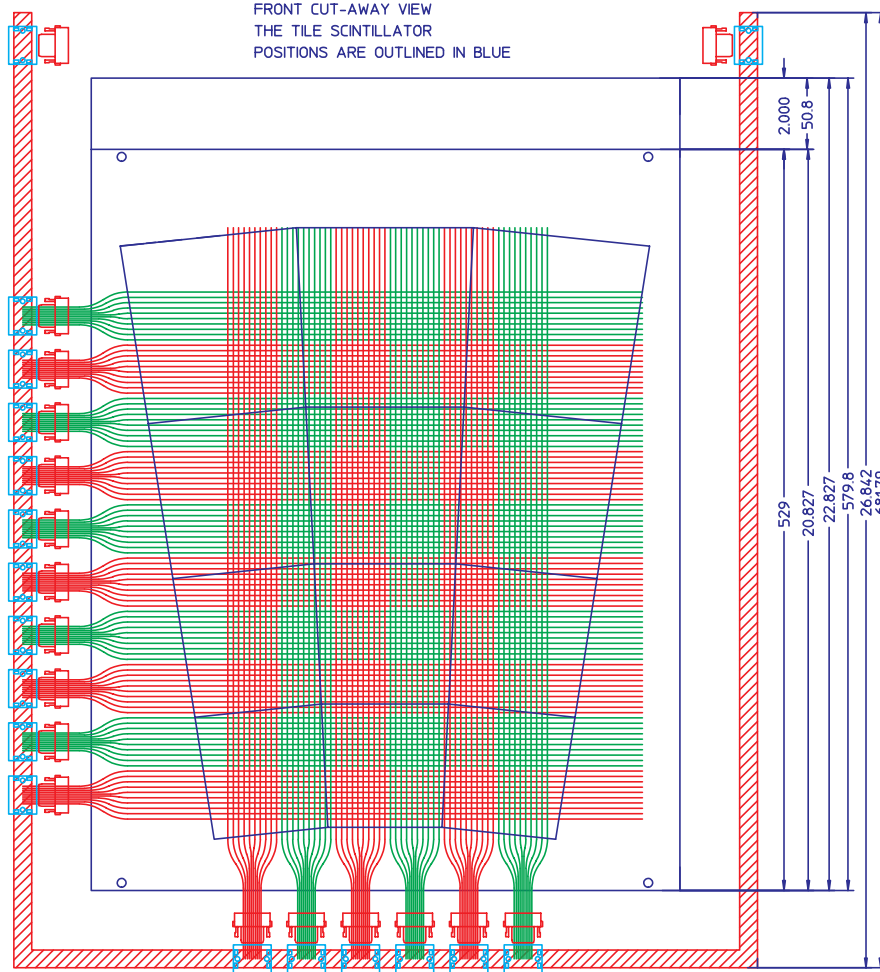


Figure 12: Schematic layout of one layer of the prototype EEMC section tested at SLAC in October 1999. Superimposed on the 3×4 scintillating tile structure is the wavelength-shifting fiber layout for light collection from the $60 \times$ and 100μ SMD strips.

Light was collected from the individual scintillator tiles by 0.83-mm diameter, Y11-doped, wavelength shifting (WLS) optical fibers, produced by Kuraray. The fiber lengths were chosen to compensate for the varying ratio of the perimeter to the area enclosed by the σ groove, thereby differentially attenuating the light from the 24 tiles forming a given projective tower. The WLS fibers were polished and then mirrored on one end. The other end was glued into an optical connector and then polished again using a diamond fly cutter. The fibers were prepared by the MSU group and underwent the same quality control procedures established for the optical fiber production for the STAR barrel electromagnetic calorimeter (BEMC). Optical connections were made between the WLS fiber in the scintillator tiles and 3.5-m long, 0.90-mm diameter clear optical fiber, using a ten-fiber connector produced by DDK Electronics. These long pieces of clear fiber transported the light from the light-tight detector box to a photomultiplier tube (PMT) box. A second optical connection was made on the PMT box to 1.0-m long, 1.00-mm diameter clear optical fibers that routed the light from the 288 tiles to polished lucite light mixers attached to 12 Burle 83101 PMT.

These PMT provide readout of the scintillation light produced in the towers of the prototype calorimeter. The clear fiber pigtailed were also constructed and tested by the MSU group, following the same procedures that are used for the BEMC optical fibers.

3.2 Description of the prototype shower-maximum detector

The prototype shower-maximum detector (pSMD) consists of two planes of triangular cross section scintillator strips, formed by extrusion, with a centered hole into which a WLS optical fiber is inserted for light collection. The 0.83-mm diameter WLS fibers were prepared by the MSU following the same procedures used for the prototype scintillator fibers. The scintillator strips have a transverse profile approximating an equilateral triangle, with an apex-to-base height of 0.5 cm. The strips were given to us by the D0 group. The quality control procedures followed in their manufacturing are unknown. Careful measurements of the strip dimensions indicated there were two separate sets. One set, wrapped in aluminized mylar by the D0 group, had an average apex-to-base height of 5.4 mm. The second set were not wrapped, and had an average apex-to-base height of 5.1 mm.

After being cut to length, the individual strips were wrapped at IUCF in two overlapping layers of 25 μm thick aluminized mylar to optically isolate them from their neighbors. Two different strip lengths were used. The x pSMD plane comprises 60 strips, each 43 cm in length and the y pSMD plane comprises 100 strips, each 36 cm in length, as indicated in Fig. 12. The 60 (100) wrapped scintillator strips were epoxied between two 0.8-mm thick G10 sheets to form the x (y) pSMD plane.

The WLS fibers in the strips were connected to 0.90-mm diameter clear fibers using the same design optical connector used for the calorimeter tiles. The clear fibers were polished on both ends, but only one end was glued into the DDK connector. The free end of the fiber was coupled directly to the face of the PMT. A bundle of ten 3.5-m long clear fibers was contained in a light-tight, flexible RTV tube. Sixteen RTV tubes were threaded through holes machined in the side of a light-tight box housing ten multi-anode PMT (MAPMT). The holes were subsequently sealed to prevent light leaks. The clear fibers routed light from the individual pSMD strips to individual pixels on the Hamamatsu H6568 MAPMT. The mapping of strips to pixels was chosen to minimize the influence of neighboring pixel cross talk in the measurement of electromagnetic shower profiles. The ten sets of 16 anode currents from the H6568 were sent through passive delay lines, and then were integrated and digitized by LeCroy 4300B (FERA).

3.3 Description of simulations for the prototype

A GEANT model of the pSMD, the prototype calorimeter and the T-438 experimental configuration was created to compare the in-beam and cosmic-ray precalibration measurements to simulations. The simulations are very similar to those used to predict the $\gamma/\pi^0(\eta)$ discrimination via shower-shape analysis for the full endcap electromagnetic calorimeter in STAR [1]. The salient features of the GEANT model are:

- The strips are assumed to be perfectly uniform, having an equilateral triangular profile. No geometrical irregularities are included in the plane of strips in the GEANT model. The pitch of the strip placement was slightly larger than the half-length of the triangular base to account for the mylar wrapping.
- Some details of the pSMD construction were accounted for, including the G10 substrate to

which the strips were glued and the central WLS fiber hole in the scintillator strip. These details result in only small reductions in the simulated energy deposition in the strips.

- Light collection within the strips is assumed to be uniform, independent of position. The simulated energy deposition is converted to light output, by assuming N photoelectrons for a minimum ionizing particle (MIP) crossing from the apex to the base of the triangle. The simulated energy deposition in a strip is converted into an effective number of MIPs crossing from apex to base. That number, and the input N value, are used to compute the mean of a Poisson distribution. The number of photoelectrons for the event is drawn at random from the Poisson distribution. For the simulation of the ‘effective gain’ determination via cosmic-ray muons, the light output (N) was chosen from a Gaussian distribution for individual strips. For the simulations of the T-438 data, a constant value of $N = 4$ photoelectrons was assumed.
- Nearest neighbor cross talk, distributed according to Poisson statistics, is assumed for the multi-anode photomultiplier tubes. The mean value of the nearest neighbor cross talk was an input parameter. A value of 1.5% accounts for the measurements, as described below.
- The conversion of the simulated light incident on a MAPMT pixel to the ADC count assumes that a single photoelectron produces a Gaussian response. The centroid of the Gaussian represents the gain and the sigma of the Gaussian represents the pixel resolution. A Gaussian noise contribution is also included in the simulation. For the simulation of the ‘effective gain’ determination, the pixel gain was chosen from a Gaussian distribution. For the simulations of the T-438 data, a constant value was assumed.
- The beam phase space for the Final Focus Test Beam facility at SLAC was simulated by drawing values for the x (y) positions and angles of the incident electrons from Gaussian distributions. The focal point of the beam was assumed to be at the center of the detector.
- To compare the prototype detector precalibration measurements to simulations, a model of the cosmic-ray muon flux was used. That simulation properly accounts for the muon energy and angle distribution.

3.4 Detector tests

Prior to transport of the prototype to SLAC, tests were performed at IUCF to measure the tile and strip response to cosmic-ray muons. Tests were conducted without the lead converters in the stack, allowing the detector to be oriented horizontally. One use of the cosmic-ray data was to establish that all of the optical connections for both the tiles and the strips were properly made. The mapping of strips onto MAPMT pixels was verified by correlating which strips had significant pulse height with the projected positions from the multi-wire proportional counters in the test stand. These tests uncovered several errors in connections of the optical fibers. For the strips, the horizontal orientation cosmic-ray data additionally provided a means of determining the ‘effective gain’ of individual strips, defined as the product of the MAPMT pixel gain and the strip light collection efficiency. The results from the gain matching procedure are described below. Data were also collected with the prototype in a vertical orientation to enable a comparison of the detector performance at IUCF, where the calibrations were performed, and at SLAC, after the transport of the detector. No observable change in the performance of the prototype was observed from the cross-country shipping.

The prototype was mounted in the Final Focus Test Beam (FFTB) at SLAC for test-beam run T-438, which ran parasitically to the BaBar experiment. The detector was mounted on Thompson rails, to enable remotely actuated left/right translation of the detector by ± 10 cm through the electron beam. The detector was mounted on four feet. The feet enabled a 9.8° tilt of the detector about the horizontal axis and also provided a means of manually translating the detector by ± 10 cm in the vertical direction. The tilt angle of the detector partially compensated for the projective geometry, enabling showers from the nearly horizontal electron beam to be mostly contained within a single tower. Two scintillators were mounted upstream of the prototype, and were used to trigger the readout of the calorimeter. A third counter with a 2.54 cm diameter hole concentric with the beam was used to aid in focussing the beam.

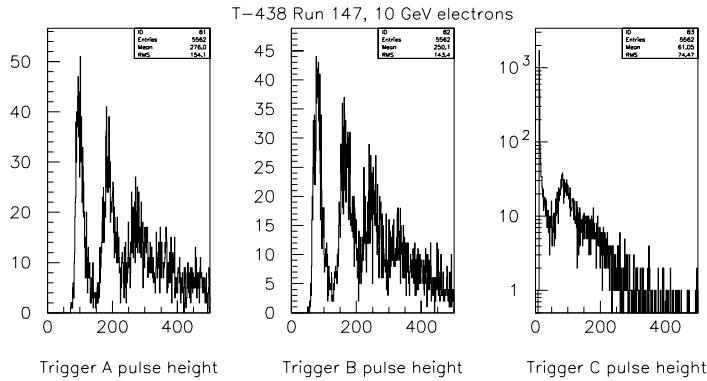


Figure 13: *Raw pulse height distributions from the plastic scintillator trigger counters. For this run, the electron beam in the FFTB had an energy of 10 GeV and was well focussed. The pulse height distribution for trigger counter A and B has peaks from SLAC pulses containing 1, 2, 3 or more 10-GeV electrons. Trigger counter C has a 2.54 cm diameter hole, aligned with the beam. More than 60% of the events result in no pulse height in counter C, implying the beam was well focussed and electron induced showers were initiated in the prototype calorimeter.*

The FFTB is a highly sophisticated beam line, originally constructed to focus 1-ps high intensity electron pulses to sub-micron transverse dimensions, as required for the Next Linear (e^+e^-) Collider. To achieve that goal, the alignment of beam-line elements is highly precise, and a detailed understanding of the beam-line optics exists. The FFTB provides an ideal environment for calorimeter tests. A secondary electron beam is produced upstream of a small-angle bending magnet prior to the FFTB. Slits mounted before and after the magnet can be positioned to sub-millimeter accuracy in both position and width. The beam energy spread in the FFTB is $\sim 0.1\%$ and the emittance and secondary beam intensity is defined by the opening of slits at the momentum analysis magnet. Typical beam intensities for T-438 were ~ 1.5 electrons per SLAC pulse, resulting in single pulses having either 0,1,2 or more energetic electrons. The number of electrons in a SLAC pulse was easily measured by the pulse height in the trigger counters and the pulse height in the calorimeter towers. Typical trigger counter pulse height distributions are shown in Fig. 13. All of the electrons within a single SLAC pulse arrived within ~ 1 ps. The repetition rate was 10 Hz. For T-438, secondary electron beams having energies of 5, 10 and 20 GeV were tuned. The 10- and 20-GeV runs were conducted in two modes. In the ‘focussed mode’, a beam spot having a diameter of a few mm was directed onto the prototype. In the ‘defocussed mode’, the sophisticated optics of

the FFTB enabled the beam to be spread to a ~ 1 cm diameter spot to provide a sample of events where the spatial separation of the incident electrons approximated the separation on the EEMC within STAR of photons arising from the decay of π^0 .

3.5 Status of T-438 data analysis

The emphasis in this section is on the performance of the prototype shower-maximum detector (pSMD). Understanding the performance of the pSMD was the primary objective of the T-438 run. The performance of the calorimeter towers will not be reported here, because it was discovered after the run that the PMT used for the tower readout were saturated by the scintillation light from the electron-induced showers. These tower PMT were originally purchased to allow high-gain studies of scintillator tile response to individual cosmic ray MIP's, and were not intended for use in the STAR environment.

3.5.1 pSMD gain matching

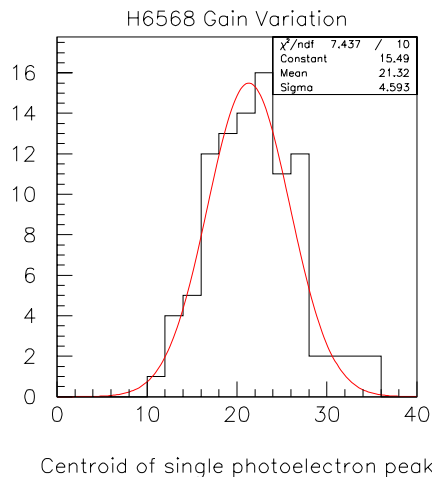


Figure 14: *Distribution of single photoelectron peak centroids from individual pixels of the 16-anode Hamamatsu H6568 multi-anode photomultiplier tube. The observed variation is consistent with other measurements of the pixel-to-pixel gain variation [16].*

Cosmic-ray muon events were used to match the ‘effective gain’ of the 160 strips of the pSMD. There are two factors determining the effective gain. One factor arises from the sizeable pixel-to-pixel variation of the MAPMT gain. The second factor is associated with the strip-to-strip variation in the light output, arising from differences in the scintillator strip quality, the mylar wrapping, differences between optical fibers, couplings between fibers and couplings between the optical fiber and the MAPMT. The ‘effective gain’ is the product of these two factors. The variation in MAPMT gain was measured separately by determining the centroid of the single photoelectron peak from the pulse height spectrum for a strip. A distribution of these centroids is shown in Fig. 14. The variation in the response of individual pixels of the Hamamatsu H6568 is similar to what has been reported by other groups.

A separate determination of the ‘effective gain’ was made from the response of the strips to incident cosmic-ray muons. The triangular cross section of the strips poses a challenge to the measurement of the light output from the strip because of the varying amount of scintillator traversed by the incident muons. To reduce this variation, events were selected that primarily traverse a strip from the apex to the base of the triangle, by demanding that the adjacent strips have small pedestal-corrected pulse height. The centroid of the resulting pedestal-corrected pulse height distribution is computed, and its inverse is associated with the strip’s ‘effective gain’. The distribution of centroids from the individual strips is shown in Fig. 15. The efficacy of this procedure for determining the ‘effective gain’ has been verified in simulation. The effectiveness of this procedure is further supported by the quality of the results for the shower profiles from the T-438 data.

00/02/02 10.14

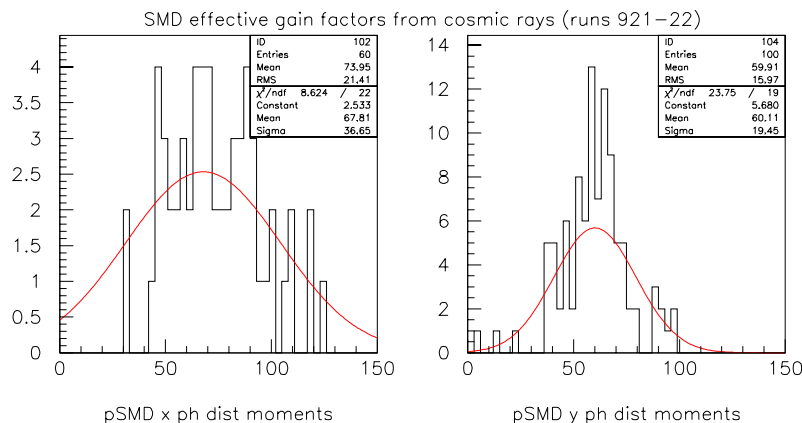


Figure 15: *Distribution of pulse-height centroids for ‘apex-to-base’ cosmic-ray events for individual strips of the pSMD. The strip ‘effective gain’ is assumed to be proportional to the inverse of the pulse height centroid.*

Several features of Fig. 15 are striking and have implications for the construction of the SMD of the EEMC.

- There are differences in the average performance of the strips comprising the two pSMD planes. This difference probably reflects the fact that the strips were given to us by the D0 collaboration, and the quality controls applied to the donated strips were unknown. When assembling the pSMD, the x-plane strips were found to have slightly larger dimensions than the y-plane strips, but that difference is too small to account for what is observed in Fig. 15. The implications for the construction of the SMD for the EEMC is that, **careful quality control procedures must be followed when producing the scintillator strips to minimize the variation in light output.**
- The variation in the strip ‘effective gain’ is larger than the pixel-to-pixel variation of the H6568 gain. This can probably be improved by quality control procedures in the strip production, but it is inevitable that the light collection efficiency will vary between different strips. The implications for the SMD of the EEMC is that **the number of bits in the ADC used to**

encode the anode currents should be increased to preserve the needed dynamic range.

3.5.2 Analysis of average transverse profile of electron showers

Data from T-438 for 5-GeV single-electron events were analyzed to examine the average transverse profile of the resulting electromagnetic showers, as measured by the pSMD. The individual strip pulse heights were corrected for the measured pedestal and an ‘effective gain’, deduced from cosmic-ray data as described in the previous section. Single-electron events were selected by imposing conditions on the observed pulse height in the appropriate calorimeter tower(s). A global view of the response of the pSMD is provided in Fig. 16.

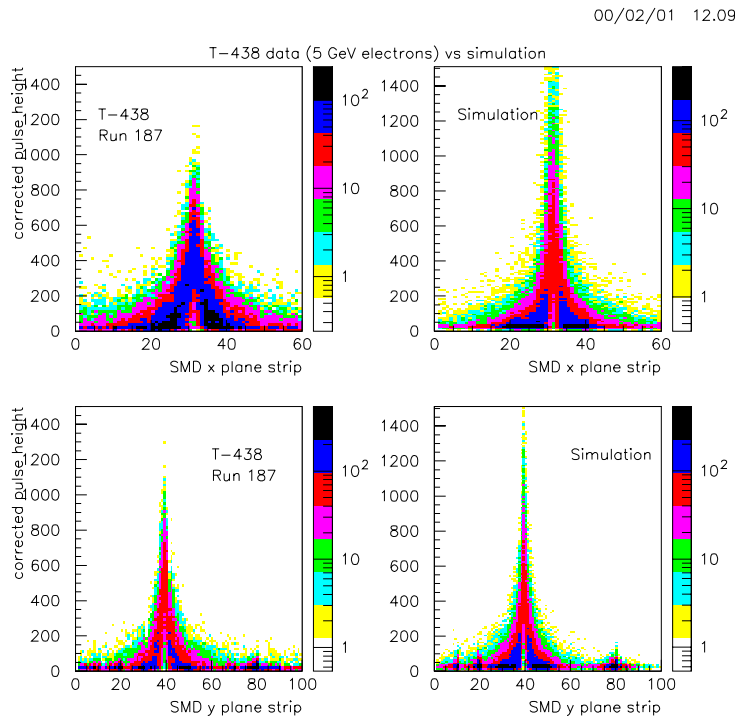


Figure 16: (Left) *Electromagnetic shower profile, as measured by the prototype shower maximum detector (pSMD). The detector is illuminated with 5 GeV electrons produced at SLAC. The horizontal axis is strip number and the vertical axis is corrected pulse height. The correlation shows the relative intensity of the response from different strips.* (Right) *Simulation of the pSMD response to 5-GeV electrons.*

The following features are observed in Fig. 16:

- The general smoothness of the shower profile observed in the data suggests that the matching procedure, described earlier, accurately determines the ‘effective gain’ of individual strips.
- The general features of the observed average shower profiles are reproduced by the simulation. The most obvious shortcoming of the simulation is its inability to predict the greater width of the pSMD x-plane profile compared to the y-plane profile.

- The simulation predicts larger pulse heights near the core of the shower than are observed in the data. This may be due to saturation of the MAPMT output with the non-tapered resistive voltage divider bases used for these tests, as discussed in more detail below.
- The features observed in the correlation near strip numbers 20 and 80 in the pSMD y-plane are associated with MAPMT cross talk. These strips neighbor pixels on the MAPMT that are subjected to large light output. The simulation includes 1.5% nearest-neighbor optical cross talk on the MAPMT, and qualitatively describes the features observed in the data.

A more quantitative analysis of the average shower profile can be performed by examining the average pulse height observed in each strip for the full sample of 5-GeV single-electron events. The results for the average pulse height shower profile are shown in Fig. 17. The data in the top, middle and lower frames were obtained as part of a horizontal scan of the detector across a focussed 5-GeV electron beam.

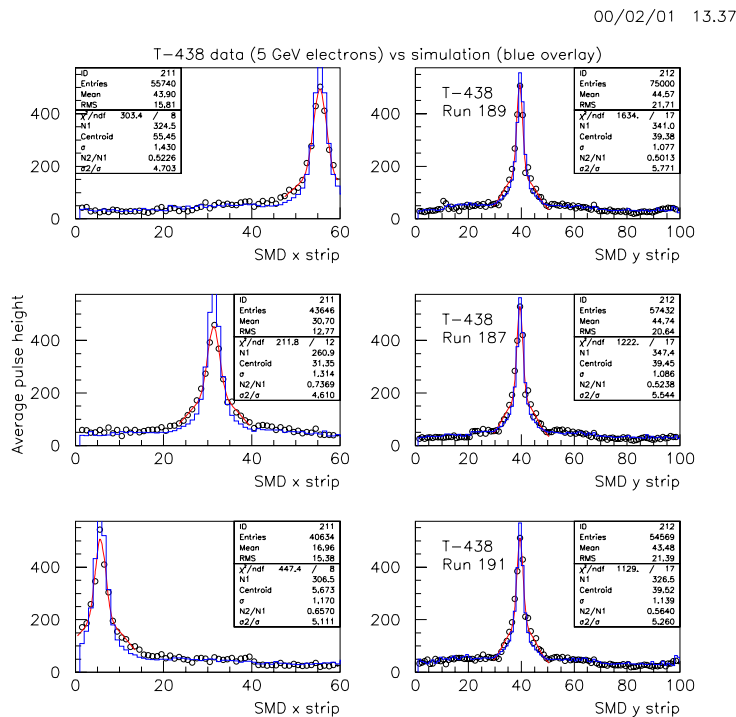


Figure 17: Average pulse height versus strip number for the x- (left) and y- (right) prototype shower maximum detector. The points are the measured average pulse heights. The points are well fit by a distribution used in the simulations of $\gamma/\pi^0(\eta)$ discrimination reported earlier. The solid-line histogram results from the simulation described in the text.

From the uniformity of the response of the pSMD x-plane as the detector is moved through the electron beam, it is evident that the determination of the ‘effective gain’ of individual strips by the cosmic ray measurements is accurate to at least the 10% level. Already, this accuracy is sufficient for the discrimination between single photons and di-photons arising from $\pi^0(\eta)$ decay in STAR [1]. It is likely that *in situ* calibrations can improve the ‘effective gain’ determination.

The transverse shower profile measured by the pSMD y-plane is quantitatively described by the simulation. The profile is well described as a central narrow core with long tails. From the simulation, it is possible to establish that the non-zero response, on average, of the strips far from the shower core is associated with the shower development, rather than optical cross talk on the MAPMT. Also evident in Fig. 17 is that the response of the y-plane strips is very nearly independent of position along the detector. This suggests that optical attenuation over a ~ 30 cm length of the triangular strips is negligibly small.

The transverse shower profile measured by the pSMD x-plane is qualitatively similar to the simulation, but the latter misses important details. In particular, the simulated x-plane shower profile is more narrow, in both the central core of the shower profile and in the tails, than the data. As well, the simulation predicts a significant difference between the x- and y-plane response, that is not observed in the data. These features suggest that some tuning of the GEANT simulation is required. Studies of how to accomplish this are underway.

3.5.3 Analysis of event fluctuations of the shower profile

To discriminate between single photons and di-photons arising from energetic $\pi^0(\eta)$ decay using the shower-maximum detector in STAR, it is critical to understand the fluctuations in the transverse shower profile. These fluctuations can produce a single-event response in the SMD similar to what is observed in the pSMD during the T-438 run (Fig. 18). In that figure, the clump of energy deposition near pSMD x-strip number 35 probably results from the fluctuations in the single-electron-induced shower. If such a profile were observed in the STAR EEMC, and no charged particle track projected to this position, implying that a neutral particle initiated the shower, then such an event would probably be identified as a di-photon, arising from π^0 decay, because of the second peak in the profile distribution. The crucial question is, are the shower fluctuations properly modeled by GEANT?

Before addressing this question, it is useful to comment on other features of the pSMD single-event shower profile (Fig. 18) and the resulting implications for the design of the SMD of the EEMC. The small pulse heights observed in the pSMD y-plane strips that are significantly displaced from the shower center probably arise from nearest-neighbor optical cross talk in the H6568 MAPMT. To minimize the influence of cross talk on the shower-shape analysis of STAR EEMC data, it is critical to choose an appropriate mapping of strips to MAPMT pixels such that nearest neighbors on the MAPMT never correspond to strip number differences smaller than 40. Such a mapping would provide a set of contiguous strips within the SMD that are not strongly affected by optical cross talk. Events in STAR with multiple showers in the EEMC having SMD centroids displaced by more than 40 strips can be easily identified by the topology of the EEMC tower response.

To test whether the predicted $\gamma/\pi^0(\eta)$ discrimination [1] is reasonable, it is important to establish if the shower fluctuations are properly modeled by GEANT. One measure of the most relevant shower fluctuations is the second moment of the pSMD x- and y-plane single-event profile distributions, restricting attention to strips within ± 10 of the centroid of the shower. For the mapping of strips to MAPMT pixels used for the pSMD, this restriction also minimizes the influence of optical cross talk on the MAPMT. The distribution of second moments, with this restriction applied to the pSMD x- and y-planes, is shown in Fig. 19. Also shown in the figure are results from the simulations. Exactly the same restrictions are applied to the simulations as are applied to the data.

In general, the simulations provided a very good description of the single-event fluctuations, as measured by the second moment of the shower-profile distribution. The mean value of the simulated

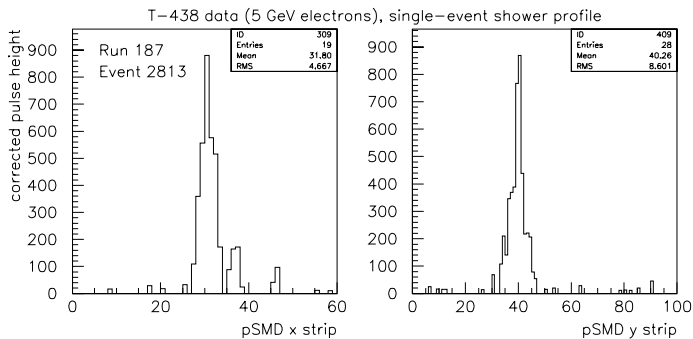


Figure 18: *Single-event shower profile measured by the prototype shower-maximum detector during T-438 at SLAC. The event corresponds to a single 5-GeV electron incident on the center of the prototype calorimeter. The profile is generated by sorting all strips that record non-zero pulse height in the event. The pedestal- and gain-corrected pulse height is used as a weight in the histogram. The second moment of the resulting distribution is one measure of the event-to-event shower fluctuations.*

second moment distribution is 0.5 strips smaller than observed in the data for the pSMD x-plane. The shape of the distribution is very similar between the data and the simulation, suggesting that the observed fluctuations are in agreement with the simulation. The smaller value of the second moment is undoubtedly correlated with the underestimate of the average shower profile observed in Fig. 17. There is quantitative agreement between simulation and the data for the pSMD y-plane.

The conclusion that can be drawn from Fig. 19 is that **the predicted 80% suppression of the $\pi^0(\eta)$ yield (with cuts that retain 80% of the single photons) can be achieved with the triangular-strip shower-maximum detector that will be built for the STAR endcap electromagnetic calorimeter.**

3.6 Summary of lessons learned from T-438

Overall, the in-beam test of the prototype shower-maximum detector demonstrated that the basic principle of the detector works, and that the response of the SMD can be successfully modeled. This suggests that the discrimination between single photons and di-photons arising from the decay of $\pi^0(\eta)$ can be accomplished using a shower-shape analysis of the response of the SMD in the STAR EEMC.

In addition to this primary objective, many things were learned about the prototype calorimeter. They are simply summarized below, without providing supporting details.

- It was found that the response of the calorimeter towers was highly non-linear with incident electron energy. This was established by examining the pulse height response of the towers for 1-, 2-, 3- and 4-electron events at a single energy, and by comparing the data for 5-, 10- and 20-GeV incident electrons. Subsequent to the completion of T-438, a study of the linearity of the Burle 83101 using light-emitting diodes revealed significant saturation of the output current for the number of photons produced by the electron showers in the calorimeter at SLAC. Linearity tests of candidate PMT for the EEMC are underway. A second test run at

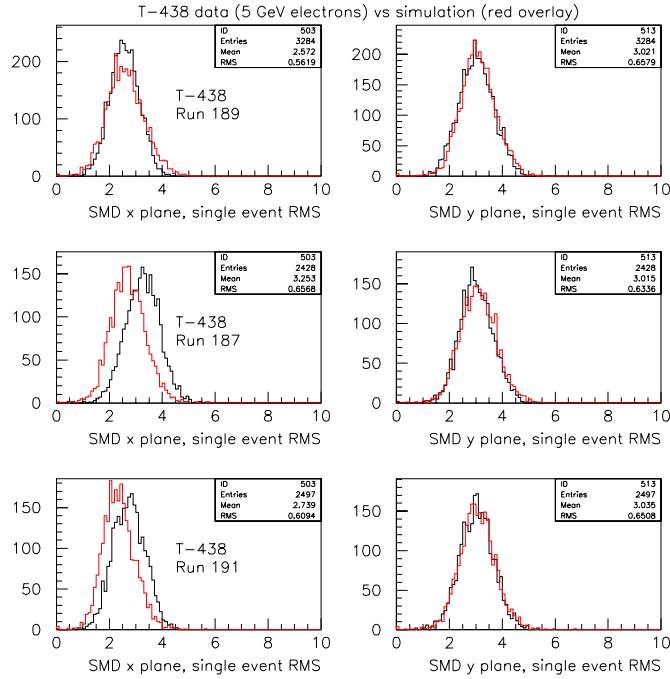


Figure 19: *Distribution of second moments of the single-event shower profiles. The second moment is one measure of the event-to-event fluctuations of the transverse shower profile. The T-438 data (solid-line histograms) in different frames were taken as part of a horizontal scan of the detector through the SLAC 5-GeV electron beam. The data are compared to simulations (dashed-line histograms) described in the text. The single-event profiles are restricted to ± 10 strips of the shower centroid to minimize the influence of MAPMT cross talk.*

SLAC will be required to check the tower linearity after the prototype detector is outfitted with the final full optical chains foreseen for the full EEMC.

- A second problem was encountered during T-438 associated with the tower PMT. A significant slow-decay-time (\sim few μ s) tail on the current pulse from the Burle 83101 was observed. The total charge in the tail was comparable to the charge observed in the narrow portion (~ 20 ns) of the current pulse. Subsequent to the completion of T-438, studies of the Burle 83101 response using light-emitting diodes excited by fast current pulses, revealed that the long tail to the current pulse was due to the PMT. The most probable explanation is that residual gas in the PMT was getting ionized, producing the very slow falloff of the current pulse. In selecting a suitable PMT for the tower readout, the fraction of the total charge associated with the slow component of the current pulse is being measured. To avoid pileup effects in the STAR EEMC, it is essential that the magnitude of this slow component be as small as possible.
- It was also found that the linearity of the H6568 with a resistive ‘straight’ voltage divider was not sufficient over the dynamic range needed for the STAR EEMC. There are two implications of this result: (1) the operating voltage of the MAPMT must be significantly lower than used

in T-438, necessitating front-end electronic (FEE) amplification, and (2) either a ‘tapered’ resistive divider or a Cockcroft-Walton base will be required for the MAPMT. The Dubna group is presently exploring the latter possibility and is also working on the design of the FEE chips.

Analysis of the T-438 data continues, focussing on the performance of the pSMD. A second test run of the prototype calorimeter will be carried out after several modifications are made. The PMT chosen for the EEMC tower readout will be used for the prototype calorimeter towers. It is also planned to have two WLS fibers inserted in the σ grooves of the tiles from the first two scintillator layers, to test their use as a preshower detector. Finally, tests of prototype front-end electronics and Cockcroft-Walton bases for the shower-maximum detector readout are planned. A third prototype test is foreseen for 2001, incorporating final design readout electronics for both towers and SMD, and the laser monitoring system (see Sec. 7.3–4) to permit precise comparison of test beam pulse height calibrations to those obtained with cosmic rays and the laser system.

4 Mechanical Design Updates

4.1 Mechanical Structure

The primary features of the mechanical structure of the detector have not changed from those presented in [1] as we move toward the final design. The design is being carried out by producing a full 3D model with standard CAD software. The lead/stainless steel laminated radiator plates form shelves between which the scintillator is placed. The weight of the radiator plates is carried primarily by a conical stainless steel hub. This hub is welded to a stainless backplate which attaches to the magnet poletip. The full detector is split in half for ease of transportation, handling and phasing of the project. The two halves divide along a line tilted by 15° from horizontal, in order to match EEMC 30° sectors to TPC sectors in STAR.

A cross section of half the EEMC is shown in Fig. 20. The stainless steel backplate is 3.2 cm thick except near the inner radius, where it must pass over the correction coil in the STAR poletip, and the thickness is consequently reduced to 2.5 cm. The conical hub, initially of 2.5 cm wall thickness, will have steps cut into its surface to provide alignment for the layers of radiator plates as shown in Fig. 21. These plates have 2 stainless steel inserts every 30° which include a spacer to the next radiator to maintain plate separation. A 0.64 cm diameter tie rod passes through each column of spacer/inserts, the 0.95 cm thick aluminum front plate and the back plate. These tie rod/spacer assemblies (here after just referred to as tie rods) divide the detector into 30° sectors. An additional radiator plate spacer is needed in the center of the outer circumference of each sector to maintain the radiator spacing. Along the surface between the halves of the detector a 0.16 cm thick sheet of stainless steel will be welded to the backplate and hub and bolted to the front plate. A clearance of 0.4 cm will be maintained between the detector halves resulting in a dead gap 0.7 cm wide along the 180° split.

The weight of the lower half detector is transferred to a recess in the poletip for the correction coil by placing a 2.5 cm thick stainless steel shelf on the back plate. This shelf will rest on the lower ledge of the poletip recess, where sufficient clearance from the correction coil is available. An existing bolt pattern on the poletip, just inside the inner radius of the back plate will be used to hold the backplate to the surface. The backplate will be counter-bored and slotted to accept the bolts. Along the 180° split 2 additional bolts will be used on each side to pull the backplate to the poletip surface. These are needed to reduce a tendency for the backplate to deflect away from the poletip surface. Two 2.5 cm shear pins will be used on each side along the 180° split to prevent rotation of the off horizontal detector as well as to enforce alignment between the detector halves.

The weight of the upper half detector is supported by a protruding pin placed in the poletip near the top of the detector. An existing 12.5 cm plug will be removed from the poletip and remachined to allow a stainless steel cap to thread on. When reinserted, this cap will extend 3.2 cm past the poletip surface to capture a matching hole in the backplate of the upper half, as shown in Fig. 22. The backplate will be bolted to the poletip surface in the same manner as the lower half. Appropriate clearance and alignment holes will be cut in the backplate along the 180° split to match up with the lower half. The upper half does not need additional bolts along this line because deflections push the backplate toward the poletip.

The necessary additional holes in the poletip will be drilled using an alignment jig. The manufacturer of the backplate and hub will use the CNC program for the final machining of the backplate to generate an aluminum jig plate having all the relevant alignment features: pin hole, shelf and existing holes. This will be test mounted on the poletip. Drill bushings will be inserted in the jig plate at the location of the new holes to be drilled, to allow precise alignment. This procedure will

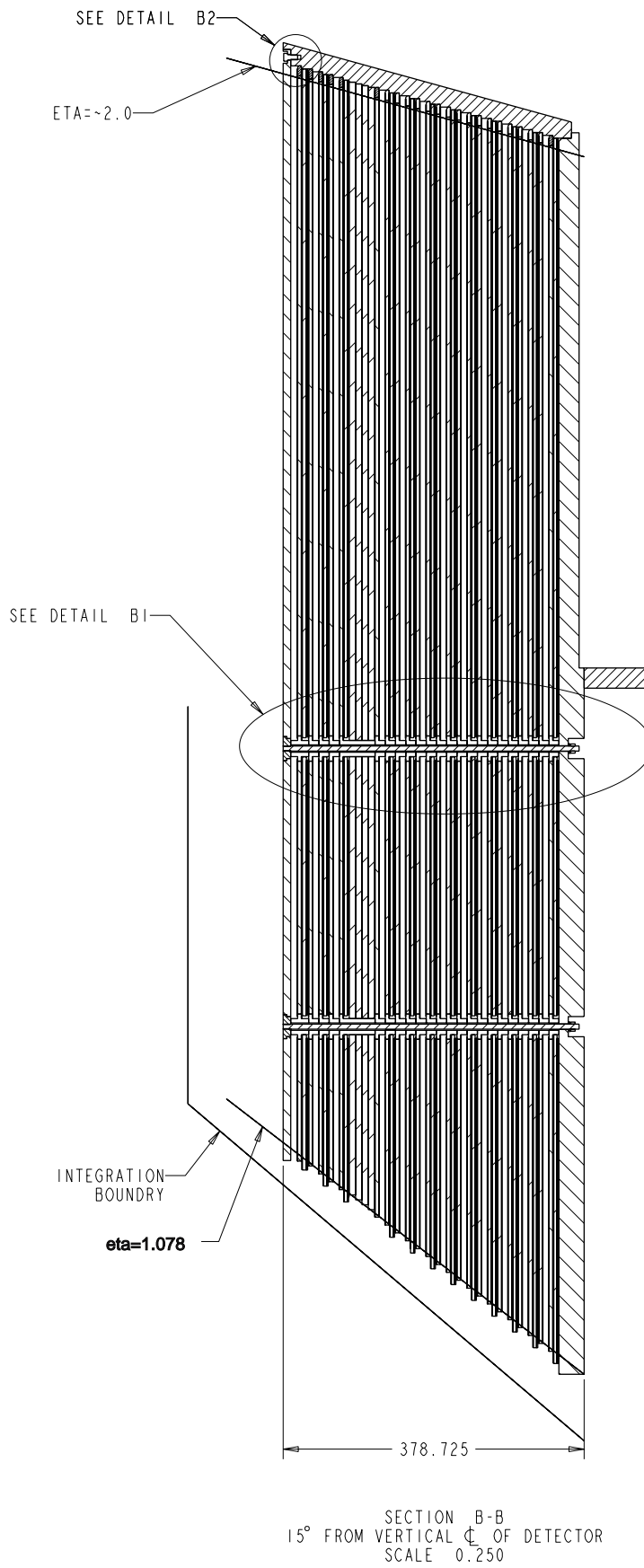


Figure 20: A cross sectional view through the bottom half of the detector.

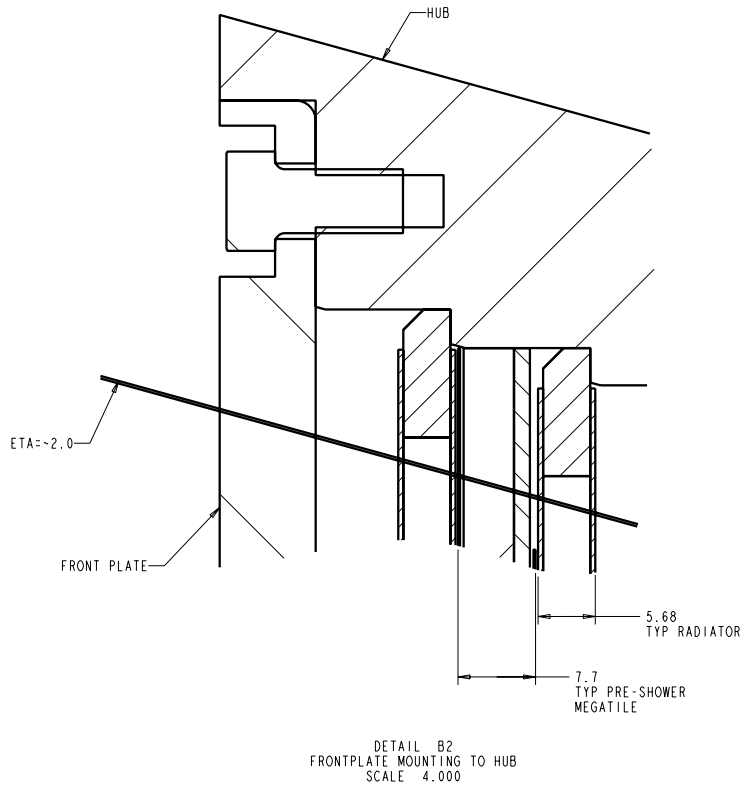


Figure 21: A cross sectional view showing the steps in the hub used to align the radiators in depth.

check the CNC program with respect to existing features as well as allow the accurate placement of the new holes.

The radiators will be made from plates of 0.47 cm thick lead, laminated on each side with 26 gauge stainless steel coiled sheet. A manufacturer with an 8 foot wide rolling mill has been located, allowing each half-annulus of lead to be made in one piece. Stainless steel sheet is readily available in 4 foot wide coils, so the stainless cladding will have to be pieced together. This will be done so that joints on the front and back do not overlap. Scotch-Weld 2216 B/A epoxy (used by CDF for the same purpose) will be used to laminate the layers on a vacuum table to be constructed for this purpose. A stainless steel ring and insert/spacers will be installed during the lamination process and then spot welded to the stainless steel cladding. A cross sectional view of a few layers near a tie rod is shown in Fig. 23 The danger of delamination due to differential contraction of the lead and stainless steel with temperature will most likely set the allowed temperature range of the detector. This should not present a problem in normal operating temperatures but may preclude shipping without climate control in the heat of summer or cold of winter.

To assemble the mechanical structure the backplate and hub will be laid horizontal on steel I-beams which will later serve to cradle the detector for lifting to vertical. The tie rods will be inserted and then radiator plates will be lowered onto the assembly one by one. Each plate will register on a step in the hub and rest on integral spaces at the tie rods. Each plate will be checked to verify that it is lying flat on the spacers, to avoid depth buildup. After inspection the plate

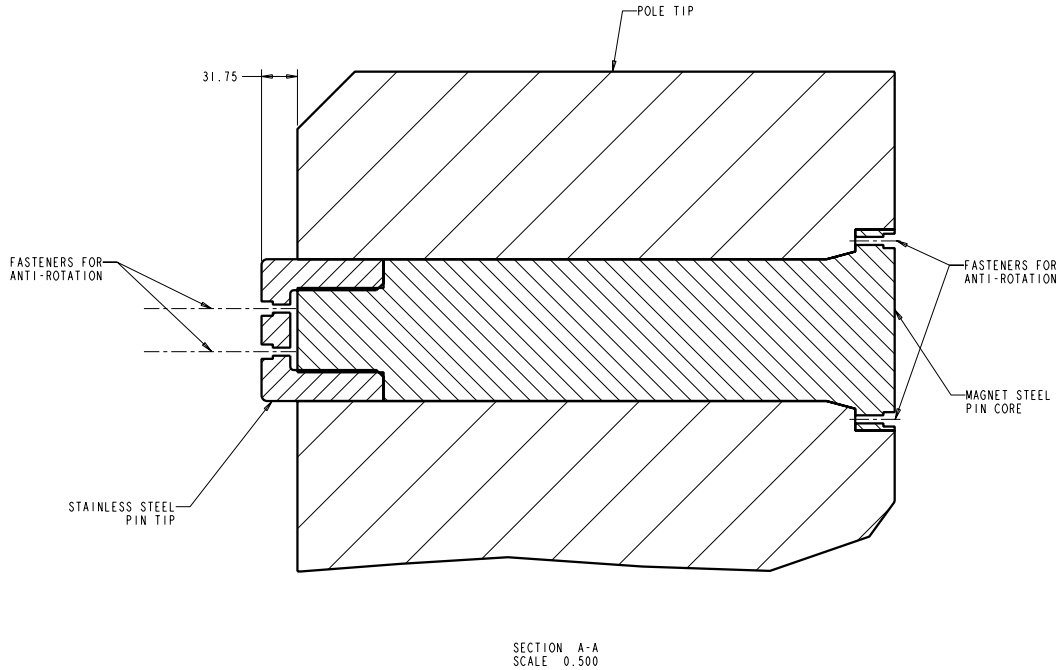


Figure 22: A 12.5 cm diameter pin is used to carry the weight of the upper half of the detectors.

will be welded to the hub. This will continue up to the SMD layer where shelves for the SMD (see Sec. 4.3) will be installed and function as additional spacers with respect to the tie rods. The remaining 5 radiator layers are then installed in the same fashion as the lower ones. The front plate is placed over the tie rods and bolted to the hub and the tie rods are tightened down with tee-nuts designed to be flush to the surface. Finally the bulkhead along the 180° split is welded to the backplate and bolted to the front plate. At this point the megatiles and SMD modules can be slid into place for cosmic ray testing.

Deflections and stresses in key areas of the detector have been modeled and checked with FEA software at IUCF to aid in the design process. To verify the final design we have contracted with outside experts in FEA to perform further calculations. Fig. 24 shows the magnitude of deflections in the lower half of the detector. These are never more than 1 mm, with the largest deflections out away from the poletip face near the inner radius. The addition of bolts and the 1.5 mm bulkhead along the split between the detector halves are important features for reducing deflections. The calculations show that the stress is quite low in most of the structure. One area of concern is the region in the backplate immediately above the pin supporting the weight of the upper half. The stress locally is only 2.5 times yield of *minimum* strengths quoted for stainless steels. This stress is not in the full part but only local to the surface directly above the pin. We have contacted manufacturers and confirmed that we should be able to specify stainless steel that will have a yield strength sufficient for us to exceed a factor of 3 safety margin.

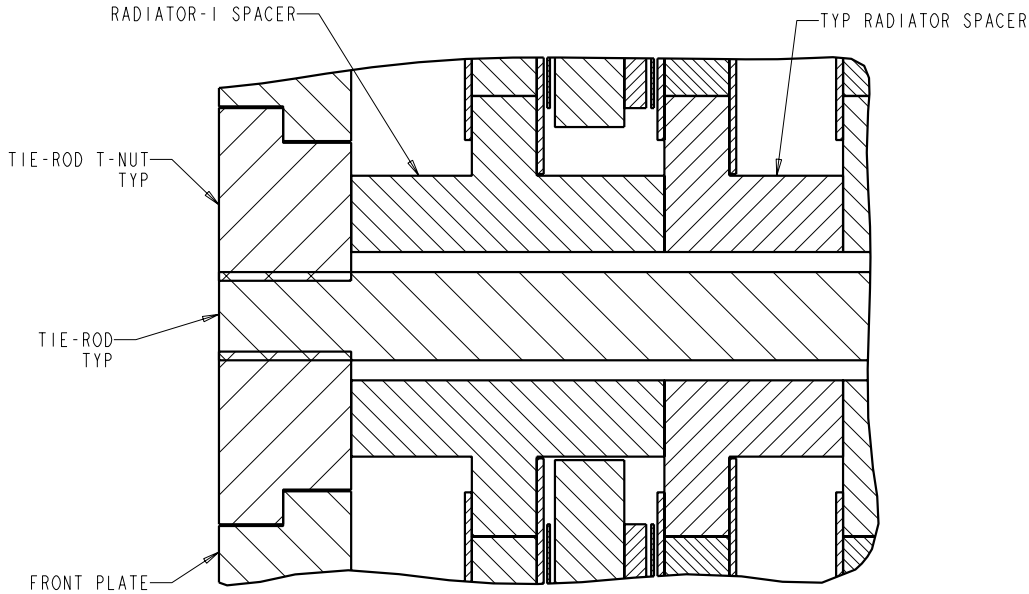


Figure 23: *Detailed view of the tie rods and spacers near the front plate.*

4.2 Megatile Design and Fabrication

The near-final design of the megatiles has not changed in a major way since the Conceptual Design Report. The scintillator tiles are to be constructed using the megatile technology developed at Fermilab for a number of detectors, as well as utilized in the STAR barrel EMC project. The tie rods divide the detector into 30° sectors which will be covered in each layer of depth by two 12° megatiles and one 6° megatile. The 12° megatiles have cutouts to capture on the tie rods, one to the left and one to the right, and the 6° megatile slides in between them to hold them against the tie rods.

An exploded view of a 6° megatile is shown in Fig. 25. The 4mm thick scintillator is covered top and bottom by 0.15mm thick Tyvek as a light reflector. The edges are painted white to reflect light also. On top of this is placed a 1.5 mm thick fiber routing layer made of white polystyrene. This whole assembly is covered with 0.05 mm black Tedlar for light isolation. The fiber routing layer has 1 mm deep paths cut in it for the wavelength-shifting (WLS) fibers to pass to the outer edge, where they enter a 12-fiber connector. Paths have been designed which allow for ℓ/A scaling compensation (see Sec. 5.1). In addition, each fiber routing layer will have a separate 1 mm deep groove to seat the “leaky” plastic fiber that will deliver pulsed UV laser light to the tiles (see Sec. 7.4). (Small holes will be cut in the Tyvek layer to allow UV light illumination of each of the 12 tiles within a 6° megatile.) The fiber guides in every 4th layer of depth will have an additional hole to house a tube to allow radioactive source insertion from the outside circumference. The fiber guides in the two preshower layers will have an additional groove cut out to rout the second set of readout WLS fibers (where ℓ/A scaling compensation is not required).

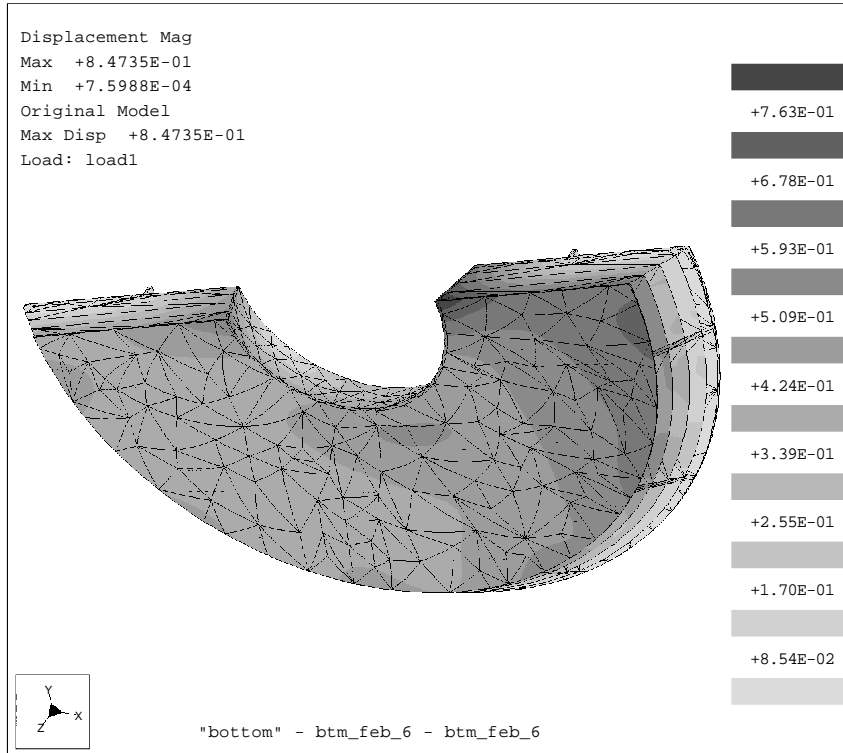


Figure 24: An FEA calculation showing the deflection magnitude for the bottom half of the detector.

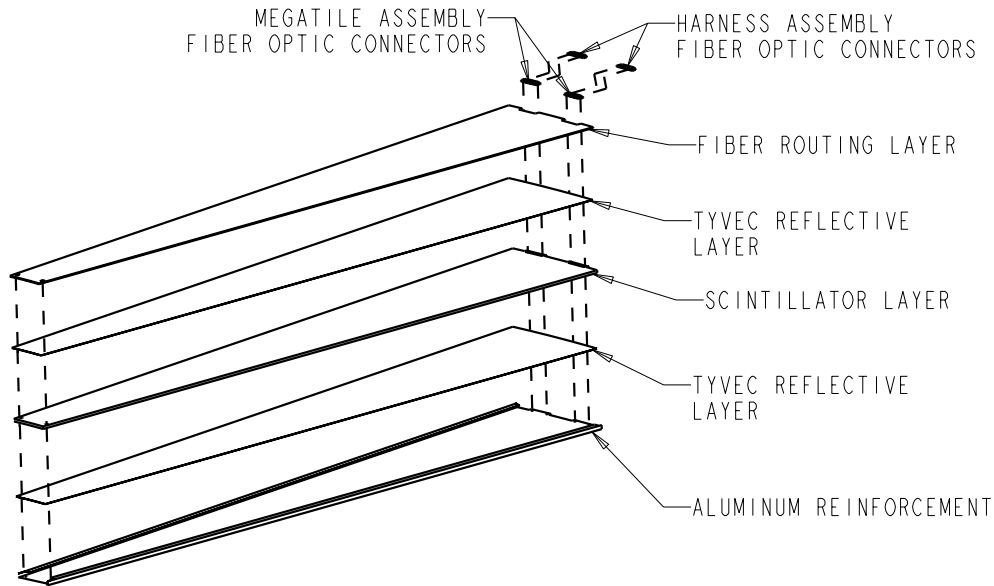
A 0.2 mm thick aluminum pan covers the bottom and bends around the edge and over the top of each megatile assembly to help hold the fiber routing layer to the scintillator and stiffen the whole assembly to bending. Standard 4-40 pan head screws and a specially machined brass tee-nut are used to fasten the layers and connector together. These fasteners are used at the inner and outer edge of the megatile, outside the active volume of the tiles. Additional details are shown in Fig. 26

Full scale mechanical prototypes of the design for both 6° and 12° megatiles have been manufactured in the IUCF machine shop. This has allowed us to verify the assembly technique and placement of fasteners. The prototypes also demonstrated that the assembly is significantly stiffened and the fiber router layer held to the scintillator layer sufficiently to avoid fiber damage.

The scintillator and fiber routing layers will be machined on a high speed CNC routing table. The machine has been ordered and delivery is expected in mid-February 2000. An 1800 sq.ft. area has been cleared out in the IUCF machine shop and is being prepared for the router, gluing and assembly areas. The first goal of this new facility will be to produce a few full scale working prototype megatiles. This will be followed by a small production run of a number of megatiles and finally by true full scale production.

4.3 Modular SMD

One of the more substantial changes to the mechanical design has been the development of a modular SMD unit which can be inserted and removed from the detector without disassembling



6° PRESHOWER MEGATILE ASSEMBLY (EXPLODED VIEW)

020300 BMP

Figure 25: *Components of a megatile.*

the structure. As shown in Fig. 27 a module covers slightly more than 30° in ϕ . On one side a straight edge will butt up against the tie rods. On the other side, there will be cutouts for the tie rods, which allow the module to extend past the 30° edge of the sector defined by the tie rods. This allows modules at different depth within the SMD layer to overlap in ϕ , and thereby eliminates dead space except for small areas immediately around the tie rods themselves. In any sector there are two orthogonal strip planes, a u and a v . The depth of the planes in adjacent sectors is staggered as shown in Fig. 28, to allow for the overlap near the line of the tie rods. About 1.5 cm of overlap is provided for. Without this overlap, the transverse shower profile information provided by the SMD would be truncated for all showers centered within $\approx \pm 4$ cm of any sector edges, seriously reducing the fiducial area over which adequate γ/π^0 discrimination could be attained. The open space left between the u - and v -planes in each sector is used for shelf/separators to hold the SMD modules in place in depth.

The scintillator strips are still oriented at $\pm 45^\circ$ with respect to the radial centerline of each sector. There are approximately 300 strips in a module. Fibers exiting along the outer ($\eta \approx 1$) circumference immediately enter a 9-fiber connector. Fibers exiting along the straight (tie rod) edge in ϕ bend back and up into a fiber routing plane (see Sec. 5.3) and then out to 12-fiber connectors at the outer circumference. The longest wavelength shifting fiber is about 187 cm and the average is about 115 cm. Aluminum channels will be constructed around the areas where the fibers exit the scintillator to protect them.

The triangular scintillator strips (10mm base, 5mm apex height) will be made by extrusion. In December we had a test extrusion of non-scintillating polystyrene, the base material, to use in mechanical prototyping. We are currently in the process of putting together a full scale mechanical

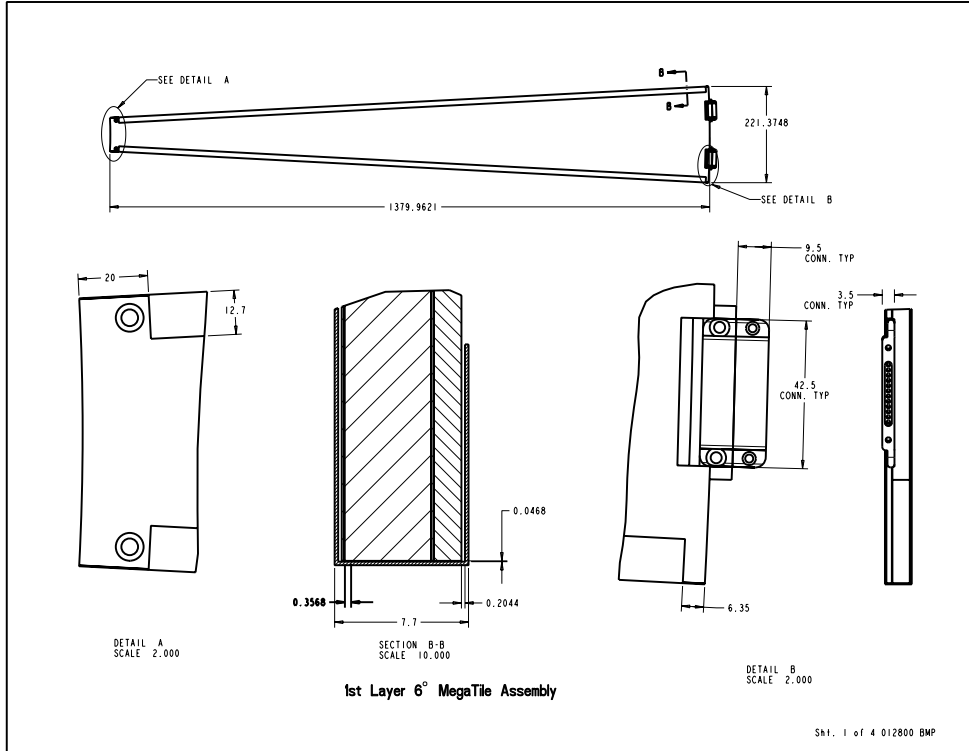


Figure 26: *Some assembly details of a 6° megatile.*

prototype of an SMD sector using the test triangular strips. We are following a number of the techniques used in the D0 forward preshower detector [18]. The strips are first wrapped with aluminized mylar. This has already been done for a large fraction of the test strips on an existing machine at IUCF. They will then be epoxied between two 0.3 mm sheets of fiber glass. The strips will only be rough cut to length. The final outer perimeter of the assembly will be machined with the IUCF router table. A 1.5 mm thick polystyrene fiber routing layer and protective channels will be glued to this assembly. The fibers will be inserted and then a final cover of 0.2 mm aluminum will be glued on. A small prototype of the fiber routing layer has already been constructed and joined to a small section of scintillator strips. The scheme for routing fibers off the edge in ϕ and back over the detector appears to work well. This small prototype is being used to study other features of the fiber routing as well.

Pulsed UV laser light will be injected into the SMD strips through the scintillator ends that house the mirrored ends of the WLS fibers. Each SMD module will be serviced by five “leaky” plastic fibers, each carrying laser light to about 60 strips. Four of these fibers will run through the fiber guide layer near the edge with the tie rod cutouts, until they exit to run alongside that edge of the SMD plane itself. The fifth leaky fiber will run through the channel where the WLS fibers bend over, entering the $\eta = 2$ edge of the SMD module through space vacated by a short unused strip near the inner edge (see Fig. 27).

The allowance for overlap of adjacent SMD sectors has increased the overall depth of the SMD from 21 mm in the Conceptual Design Report to 32 mm in the present design. This is one of several design changes and details that lead to a significant increase in the overall depth of the calorimeter. Nonetheless, as detailed in Sec. 8.1, it appears that the increased depth can be accommodated

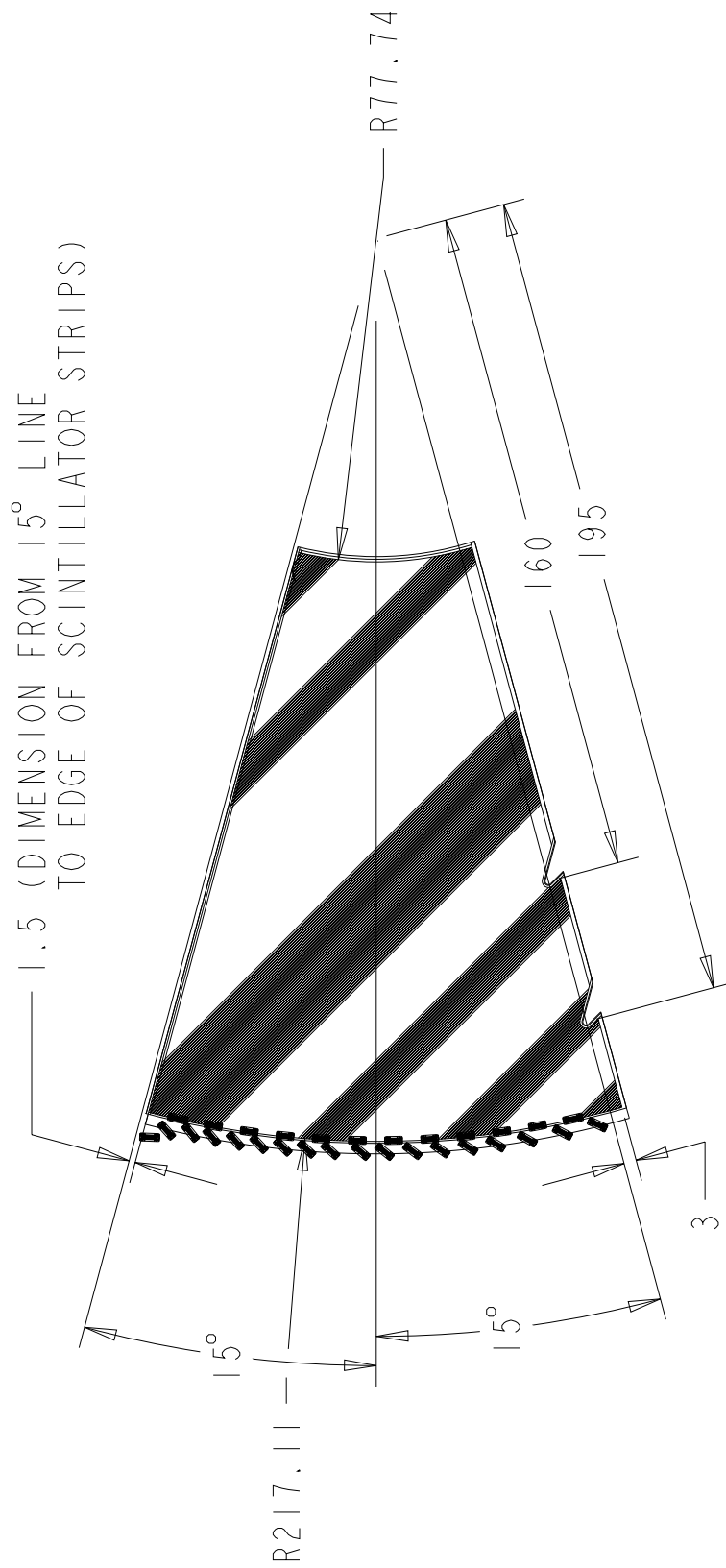


Figure 27: A modular 30° SMD sector. Only some of the strips are shown. Fibers exit the strips along the left ϕ edge and outer circumference.

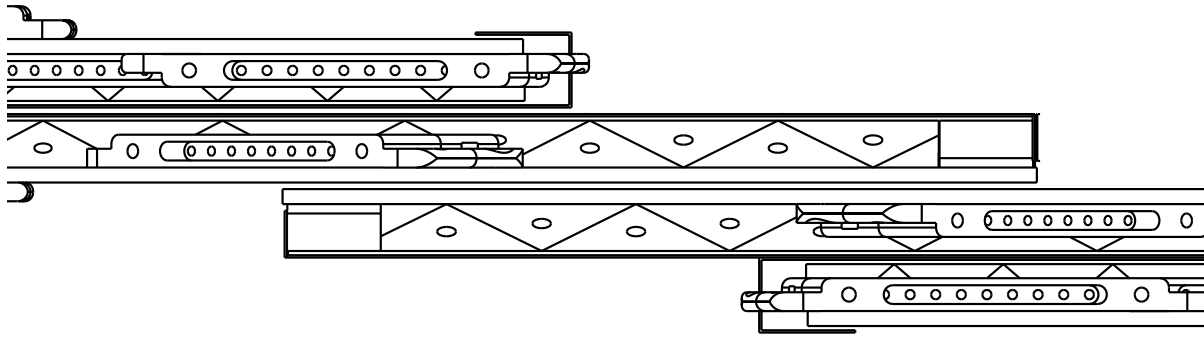


Figure 28: *An edge on view showing how the 2 planes in one sector interleave with 2 planes from an adjacent sector.*

within STAR, without sacrificing radiation lengths or sampling fraction in the EEMC. A uniform, rather than terraced, cutout will be made in the $\eta = 2$ SS hub for the SMD, facilitating the use of identical spare SMD modules for any of the four layers within the SMD.

4.4 Suppliers and Manufacturers

We have made initial contacts with suppliers and manufacturers for essentially all the components of the detector. These have served as existence proofs for the techniques we intend to use and in many cases we have gotten preliminary estimates to use in budgeting. Where possible we will continue to investigate additional vendors to allow for competitive bidding or alternative manufacturing techniques. We have also purchased small quantities of many of the materials to use in prototyping. Kuraray will be the supplier for all scintillator and fiber. A machine shop in Indianapolis considers our back plate and hub a mid-size part and has all the capability to do the annealing and certified welding. We are working with the same suppliers of lead used by CDF. The stainless steel for the radiators is standardly available in rolls and the size of the individual pieces fit on commonly available laser cutters. We have contacted mold makers used by CMS and MINOS about designs for fiber connectors. The rest of the materials are readily available.

4.5 Quality Control and Assurance

We have just begun to define our QA/QC procedures. For mechanical parts these will be primarily visual inspection, direct measurement and rejection of parts out of tolerance. The back-plate/hub structure and front plate will be manufactured by a shop that operates at ISO 9000 standards and has the capability to use a coordinate measurement machine to verify all dimensions of the final piece. For volume parts like the insert/spacers for the radiators we will measure a sample and use a gauge at limiting tolerances on all parts, to reject parts not meeting specifications. The thickness of the lead and scintillator will be sampled across their surfaces and catalogued for future reference in a part specific way. Final radiators and megatile assemblies will be checked for thickness using a gauge to verify they will fit in their final locations. As described above, the interface of the detector with the poletip will be checked using a jig plate prior to manufacture.

4.6 Coverage and Integration Issues

Critical issues in the mechanical design have included constraints from integration issues. These include the allowed depth of the detector or height off the poletip, the allowed outer diameter vs. depth and the total weight of the detector.

The allowed depth of the detector has forced us to be very careful in our designs to minimize thickness while maintaining the required performance of the radiators and scintillator. The actual size of the structure once designed is well constrained. In our design the depth is determined by precision machined parts, the hub at the inner radius and stainless steel spacers at larger radii. We expect the tolerance stack up to be less than 1 mm on the final structure. The gaps between radiator layers must be large enough to allow for thickness variations on the radiator plates and the megatiles. We have designed the gap to have 0.5 mm clearance when both the lead and the megatiles are at the edge of their tolerances, or a 1.2 mm gap for the nominal thicknesses. The result is a detector that requires 403 mm in depth compared to the existing allocation of 388 mm. (The detector depth budget is presented in greater detail in Sec. 8.1.) There is approximately 85 mm clearance in front of our detector before the TPC and SVT electronics. A distance of 51 mm must be maintained for air circulation. We have contacted the head of the STAR operations group, Ralph Brown, about the possibility of getting the additional space needed. After consultation with him we officially asked for an additional 22.4 mm, slightly more than the above difference, to allow for some design flexibility. The response has been tentatively positive, with no expected objections since there is no possibility of interference with other systems or violation of any other requirements. The final official change procedure will be followed after we have passed any reviews that might request additional changes in the design.

The edge of the active volume in pseudorapidity has been moved slightly since the Conceptual Design Report to allow more room for fiber routing. Previous designs have had the active volume at $1.069 \leq \eta \leq 2.0$. There are two concerns with the value near $\eta = 1$. More room is needed to get the fibers out of the circumference of the SMD and into a connector. The second concern is providing enough room for routing of the fiber bundles out of the detector. A considerable volume of such bundles builds up in certain regions before they can exit out the gap along the poletip. Our current design has moved the edge of the active volume to 1.078 in η . This was a rather small change in the width of the gap adding 2 cm to the original values, resulting in a gap in calorimeter coverage near $\eta=1$ of approximately 18 cm.

Previously it had been stated that STAR imposed a 30 ton weight limit on the calorimeter and associated hardware hanging on the poletip. It turns out that this number was in fact the limit on the weight hanging on the front of the poletip, as determined by the center of gravity of the detector and poletip when they are lifted by the poletip lifting fixture. This fixture is capable of lifting much more than the additional 30 tons, but if the detector moves the center of gravity too far forward, there is a danger of tipping during an earthquake. We are in the process of finalizing the calculations for an engineering change notice. Our design places less than 30 tons on the front face of the poletip and this weight is centered closer to the poletip than assumed in the original calculation that gave the 30 ton limit. We begin to approach 30 tons only when the PMT boxes and associated electronics are considered. These will be on the back of the poletip and thus help move the center of gravity away from the tipping danger. While the final numbers are not yet available, this no longer appears to be an issue.

5 Optical System Updates

5.1 Tower Optical Construction

Wavelength shifting fiber (0.83 mm, 200 ppm Y11, multiclاد S-type, from Kuraray) will be used to capture the light in a tile and transport it to a connector at the outer edge of the megatile. The σ groove is cut first with a straight end mill and then finished with a ball mill that creates a channel to capture the fiber. The σ grooves have a bend radius at the corners of 30 mm and, at one corner, a straight ramp up to the fiber routing layer. The fiber routing layer is cut as in Fig. 29 to include an S-curve that changes with layer to add extra fiber length to the run. The extra length allows for additional attenuation in the forward layers to compensate for ℓ/λ scaling of the light output from the tiles. This is about a 10% effect from the front to the back layer and requires about 21 cm of additional fiber in the first layer with respect to the last. The connectors are designed along the lines of connectors developed at the University of Illinois - Chicago. Ours will have 12 fibers to match the tower count on a megatile. Each fiber routing layer will include a track for a scratched fiber attached to the calibration laser pulsing system (see Sec. 7.4). Some of the layers will also include a thin stainless steel tube to allow insertion of a radioactive source. The longest wavelength shifting fiber is for the last layer and innermost tile. The total length of fiber in this case approaches 2 m.

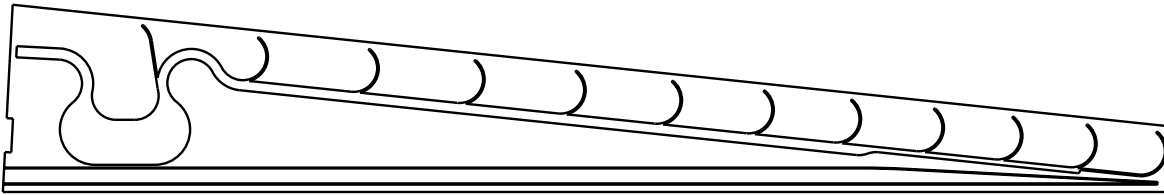


Figure 29: A fiber routing layer for a typical 6° megatile. Provision is made to allow for extra fiber length to correct for ℓ/λ scaling of the light from the tiles as a function of depth in the detector. The straight groove indicated at the bottom is intended for the “leaky” UV-transparent plastic fiber that will inject laser pulses into each of the 12 tiles within this megatile.

The light will be carried to the PMT boxes in clear fiber (0.9 mm, multiclاد S-type from Kuraray). There will be a second connector at the PMT box. The 12 fibers from a megatile will be bundled into round PVC plastic tubing, as is done with the barrel fibers, for transport out of the magnet. The detector will be enclosed in a light tight shell and the cable trays to the poletip will also be light tight. In the PMT box the fibers (1.0 mm, multiclاد S-type from Kuraray) will be rebundled into groups of 24 representing the towers for routing to individual phototubes. Note that this regrouping from 24 bundles of 12 fibers to 12 bundles of 24 fibers will physically tie the 12 PMTs together into a group. The longest path of clear fiber from megatile to PMT is expected to be about 3.6 m.

5.2 Tower Light Budget

To avoid having photostatistics limit the resolution of the calorimeter towers, it is necessary

to achieve 2 photoelectrons per minimum ionizing particle crossing individual scintillator layers of the EEMC. The light losses through the wavelength shifting (WLS) optical fibers, the optical connectors, the clear optical fiber and the mixer all must be accounted for in the ‘light budget’ between the scintillator tiles and the PMT.

Optical fibers produced by the MSU group, following the production and quality control procedures established for the barrel electromagnetic calorimeter (BEMC) construction, were used for measurements relevant to the ‘light budget’. Cosmic-ray muon events have been used to probe the megatiles of the prototype calorimeter (discussed in Sec. 3) and small scintillator tiles machined by a high-speed Thermwood router. The prototype megatiles were machined by a CNC milling machine, having a much smaller spindle speed than the Thermwood router. We have consistently observed smaller light output from the prototype megatiles than from the ‘Thermwood tile’, so the light budget accounting has focussed on the latter.

The prepared optical fibers we presently have to perform tests of ‘optical chains’ have the following lengths and connector configurations:

- WLS fiber (0.83 mm diameter) pigtails for the prototype tiles. The WLS fibers have lengths varying between 92 cm and 160 cm, are mirrored on one end and the other end is potted into a 10-fiber DDK optical connector.
- WLS fiber (0.83 mm diameter) pigtails for the prototype shower-maximum detector. Two different length fibers were produced. The WLS set 1(2) has fibers of length equal to 46(53) cm. They are prepared in an identical manner to the prototype tile fibers.
- Clear fiber (0.90 mm diameter) pigtail ‘set 1’ with 10-fiber DDK optical connectors on each end. The length of clear fiber is 350 cm.
- Clear fiber (1.00 mm diameter) pigtail ‘set 2’ with 10-fiber DDK optical connectors on one fiber end. The other fiber end is free. The length of clear fiber is 100 cm.
- Clear fiber (0.90 mm diameter) pigtails with 10-fiber DDK optical connectors on one fiber end. The other fiber end is free. The length of clear fiber is 245 cm.

All of the fibers were polished on both ends, and underwent the quality control procedures set up for the BEMC construction project.

From this set of prepared fibers, we have constructed a ‘complete optical chain’ similar to what is expected for the scintillator tiles near the $\eta = 2$ edge of the EEMC. The transverse dimensions of the 5-mm thick SCSN-81 scintillator tile are 9.0 cm \times 9.0 cm, again similar to the tile dimensions expected near $\eta=2$ in the EEMC. A schematic of this chain is shown in Fig. 30. It differs from that planned for the EEMC by an additional 100 cm of clear fiber. As well, specialized optical connectors will be used, rather than the 10-fiber connector built by DDK Electronics.

The photoelectron yield from the SCSN-81 tile machined by the Thermwood router (the so-called ‘Thermwood tile’) was measured in the IUCF cosmic-ray test stand. The large-area trigger scintillators of the test stand limit the incidence angles of the incident muons to $\leq 15^\circ$ with respect to normal incidence. To reduce the contribution of accidental dark current pulses to the Thermwood tile pulse height distribution, a second scintillator tile, with similar dimensions to the Thermwood tile, is placed immediately atop it, and software coincidence conditions are imposed on the Thermwood tile pulse height distribution. The resulting pulse height distribution is shown in Fig. 31. Apparent in the figure are peaks arising from 1, 2 and possibly 3 photoelectrons in the Burle 83101 PMT.

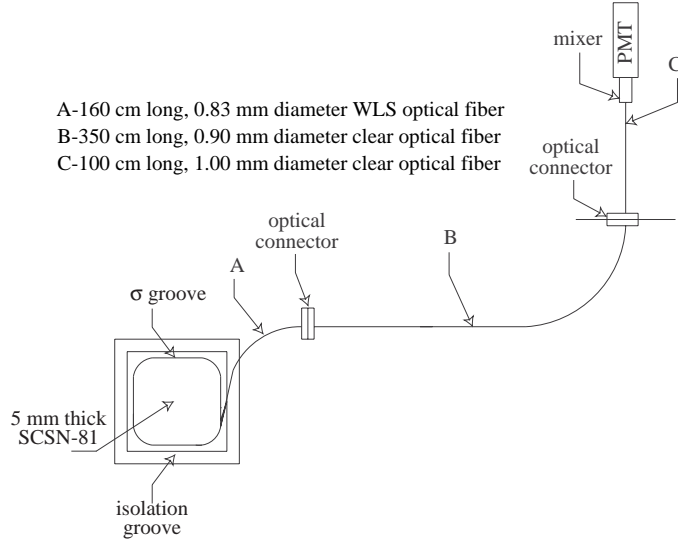


Figure 30: Schematic of the full ‘optical chain’ used in determining the light output from a 5-mm thick SCSN-81 scintillator tile.

To analyze the data to deduce the light output, the PMT response is assumed linear and is assumed to be the quantized response from 1, 2, 3, ... photoelectrons. The n^{th} photoelectron peak is assumed to be described by a Gaussian distribution defined by a centroid parameter $C_n = nC_1$ and a sigma parameter $\sigma_n = \sqrt{n}\sigma_1$. The yield of the n^{th} photoelectron peak is determined from Poisson statistics. The PMT response is then convoluted with Poisson distribution(s), specified by the mean number of photoelectrons observed in the PMT and an overall normalization. The mean number of photoelectrons for incident cosmic ray muons (μ_{MIP}) is fitted from the data in Fig. 31. Due to the conditions for the measurement, a second contributing Poisson distribution, representing the dark current response of the PMT accidentally coincident with the trigger, is included in the fit. The photoelectron yield for the dark current contribution was obtained in the same measurement by sorting the Thermwood tile pulse height distribution with different software conditions. The fitted photoelectron yield from the data in Fig. 31 is 2.3 ± 0.1 photoelectrons per minimum ionizing particle.

From this measurement, we expect that the photoelectron yield from most of the EEMC megatiles illuminated by a minimum ionizing particle will be more than 80% of the value deduced from Fig. 31. Except for the first two layers serving as preshower layers, the megatiles are 4-mm thick SCSN-81, whereas the tile that was tested had a thickness of 5 mm. It is expected that the clear fiber run carrying light between the EEMC and the PMT boxes (labeled as ‘B’ in Fig. 30) will be 250 cm rather than 350 cm, resulting in 10% larger photoelectron yield, assuming a 10 m attenuation length for the clear fiber. **The resulting yield meets the photostatistics requirements of 2 photoelectrons per minimum ionizing particle.**

Using other combinations of the optical fibers prepared for the prototype, different optical chains were constructed to investigate light losses. Light losses through the clear optical fibers, the DDK connectors and the WLS fibers were found to be consistent with other measurements [22]. A significant light loss ($\sim 30\%$) was found in the lucite mixer, used to couple the clear fiber to the

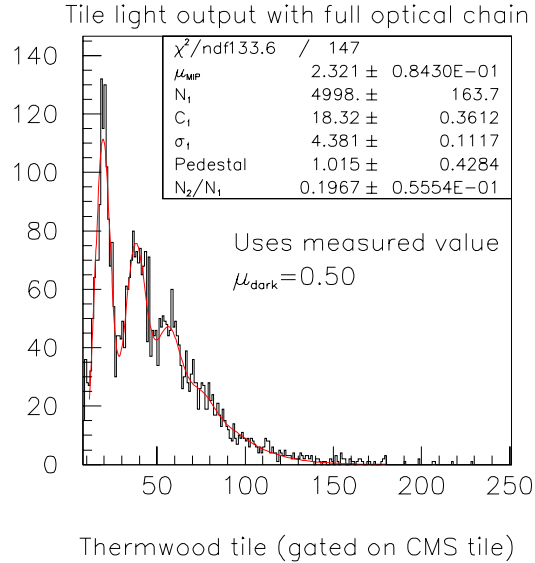


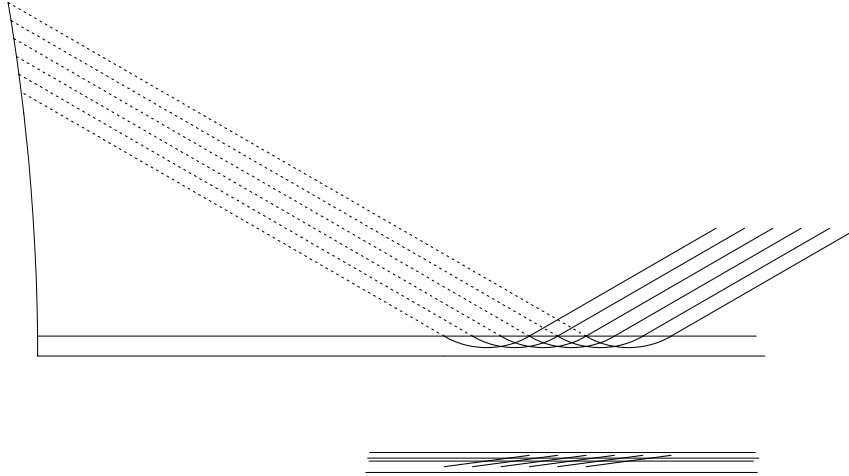
Figure 31: Measured pulse height distribution from a SCSN-81 scintillator tile exposed to near-normal incidence cosmic ray muons. The tile is readout by a ‘full optical chain’. The analysis of the distribution is described in the text. The deduced light output is 2.3 ± 0.1 photoelectrons.

PMT. The effective light attenuation in this mixer is large, and might be smaller for mixers that will be used in the BEMC. Measurements will be made with the light mixer that will be used for the BEMC.

5.3 SMD Fiber Routing

The same fiber materials as used in the megatiles will be used for the SMD detectors. As described in Sec. 4 wavelength shifting fibers exit both along one of the radial edges and also at the $\eta \approx 1$ circumference. As shown in Fig. 32 the fibers exiting along the edge in ϕ bend back and up into a fiber routing layer on top of the scintillator strips. A small prototype of this has been manufactured and works well. The fibers are then routed to the outer circumference where they enter the same type of 12-fiber connector as used for the towers. A possible concern is that the fibers in the fiber routing layers will be hit by showers and could possibly scintillate enough to produce ghost hits in the detector. We have consulted with experts from other detectors of similar construction and they find that this is in fact not a problem [18]. The fibers along the outer circumference exit and pass into a 9-fiber connector as shown in Fig. 33. The amount of space needed to get from the 5 mm pitch of the exiting fibers into the pitch of the connector is an important design issue. It appears to take at least 3 cm to do this without violating a 3 cm bend radius of the fibers. The number of fibers in this connector is chosen to reduce the space needed to get into the connector. The longest wavelength shifting fiber in the SMD is about 187 cm and the average is about 115 cm.

The clear fiber bundles for transport of light to the PMT boxes will be similar in construction to those used for the towers. In the PMT box the rebundling will be into groups of 16 for each MAPMT. Light from one of the SMD fibers for each MAPMT will be mixed with that from an LED pulser, to provide online gain stability monitoring for the MAPMT’s. Care will be taken to route adjacent strips to different phototubes to help avoid crosstalk problems within the range of a



c:\cad\smd_modular

Figure 32: *Routing of SMD fibers at the edge in ϕ .*

typical shower profile. Again the longest clear fiber run, detector to PMT, is expected to be about 3.6 m.

5.4 SMD Light Budget

The simulations of the performance of the STAR endcap calorimeter (EEMC) shower maximum detector (SMD) assumed a yield of two photoelectrons for a minimum ionizing particle (MIP) traversing from the apex to the base of the triangular strip. With this photoelectron yield, a shower-shape analysis achieved 80% rejection of di-photons produced in the decay of energetic $\pi^0(\eta)$, for an 80% retention of energetic single photons. The yield of two photoelectrons per MIP can be assumed as a requirement for the performance of the scintillator strips of the SMD. This section addresses tests of the photoelectron yield from strips having geometry similar to that envisioned for the SMD. The tests were conducted using an ‘optical chain’ similar to that envisioned for the light transport from the SMD strips to the multi-anode photomultiplier tubes (MAPMT).

Photoelectron yield measurements from the scintillator strips of the prototype shower-maximum detector (pSMD), whose construction is described in Sec. 3, have been made. The yields were measured from the pulse-height response of the pSMD strips to cosmic-ray muons. The observed photoelectron yield from a Hamamatsu H6568 16-anode MAPMT, used for detecting the scintillation light delivered by the fiber optics, averages ~ 4 photoelectrons, with a broad variation across the 160 strips of the detector. The large variation is attributed to the possibility that the 5-mm extruded strips, given to us by the D0 group, had not passed their quality assurance tests. As described in Sec. 3, the fiber optics used for the pSMD consisted of 53- (46-) cm long WLS fibers for the pSMD x plane (y plane) connected by a 10-fiber DDK optical connector to 245-cm long clear optical fibers. The latter were coupled directly onto the face of the MAPMT. There are several differences between the pSMD and the design of the EEMC-SMD:

- the strips used in the pSMD had a nearly equilateral triangular cross section with an apex-

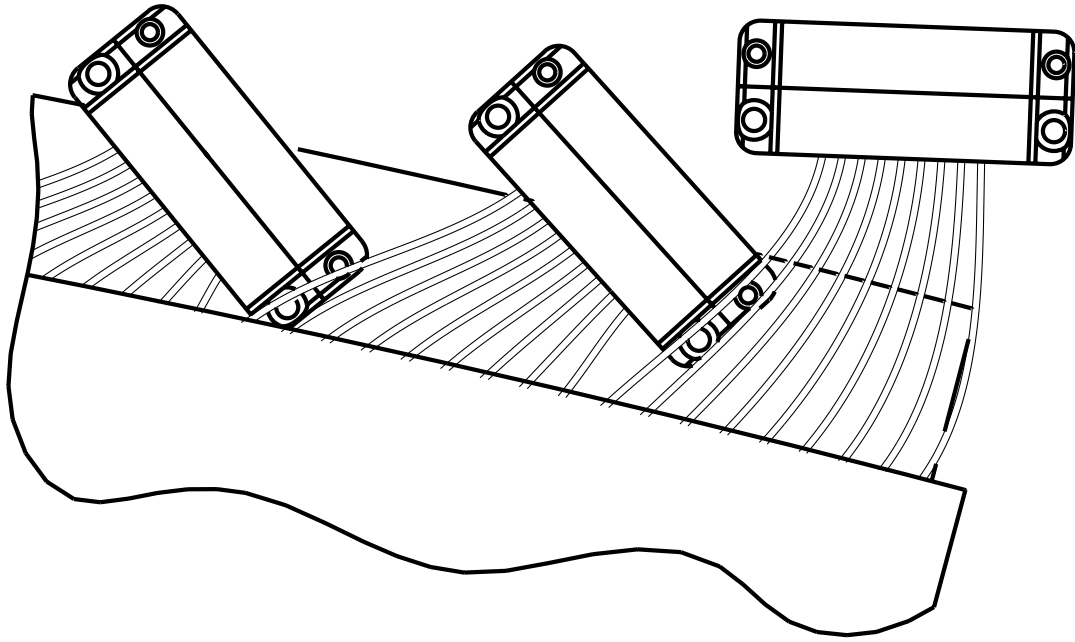


Figure 33: *Fiber connectors for fibers exiting the outer circumference of the SMD*

to-base height of 5 mm. For the EEMC-SMD, strips with an apex-to-base height of 5 mm and a base length of 10 mm will be used. The light collection could be different between the two strip geometries.

- the WLS fiber runs for the EEMC-SMD design average 115 cm, more than twice the length used in the pSMD tests.
- two optical connectors will be used in the ‘optical chain’ for the light transport from the SMD strips to the MAPMT, and the total length of clear fiber is expected to be 360 cm.

Ignoring the difference in strip geometries, the results from the pSMD tests suggest that the required photoelectron yield from the scintillator strips planned for the SMD can be achieved. The extrapolated photoelectron yield is ~ 2.4 , assuming a 3-m (10-m) attenuation length through the WLS (clear) fiber and 15% light loss at the connector. Separate measurements are required to establish if the required photoelectron yield can be obtained from the scintillator strip geometry planned for the EEMC-SMD.

A second set of photoelectron yield measurements have been performed using *machined* scintillator strips having 5-mm apex-to-base height and 10-mm base length. This profile is identical to the transverse dimensions of the strips planned for the EEMC-SMD. The strips were machined from 5-mm thick SCSN-81 and were 40 cm long. Fiber grooves were cut in the scintillator using an end mill having a diameter of 0.089 cm. A ball groove of diameter 0.107 cm was cut in the bottom of the milled grooves to capture the fiber. One possible problem with this construction is the spindle speed of the end mill used for the machining. The machining was completed before it was learned

that, for cutting the σ grooves in scintillator tiles into which WLS fibers are inserted for light collection, the higher spindle speeds of a high-speed router result in an important ($\sim 40\%$) increase in the photoelectron yield in comparison to identical grooves machined by a slow-spindle-speed end mill.

Strips with two different fiber groove depths were made. One set of 10 strips had a deep groove, effectively centering the WLS fiber in the strip, and a second set of 10 strips had a shallow groove, resulting in the WLS fiber running just inside the surface of the 10-mm base of the triangle. One of the goals of the measurement was to establish if the location of the WLS fiber in the isosceles triangle influenced the light collection. After machining, the ends of the strips were polished and painted. The other surfaces of the strips were not polished. The strips were then hand-wrapped in two overlapping layers of $25\ \mu\text{m}$ thick aluminized mylar. An array of strips shown in Fig. 34 was used for the light yield measurements. Cosmic ray muon data were collected with the strip array in the two orientations shown in the figure. Events with a specific topology of pulse heights observed in the strip array were chosen to ensure that the muon had the smallest possible path length variation through the triangular cross-section scintillator.

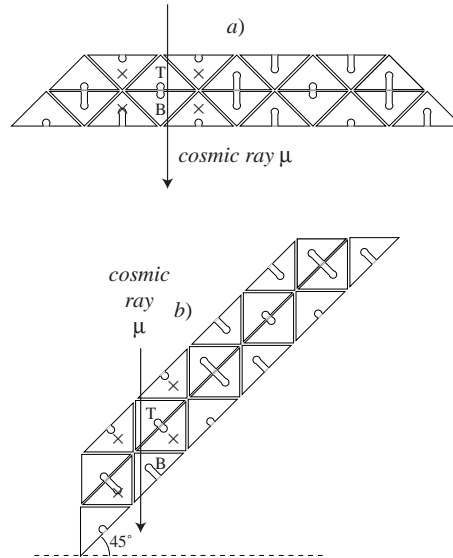


Figure 34: *Layout of machined scintillator strips used for light output measurements, performed using cosmic-ray muons. In a), muons that traverse the strips from apex to base were selected by choosing events with bounding strips (marked by \times) that have small pulse height. The pulse height distribution for $T(B)$ is then sorted for those events with large pulse height in $B(T)$. The loss of scintillator near the fiber groove can influence the deduced light output. In b), muons that traverse the strip along the side of $T(B)$ were selected by choosing events with small pulse height in bounding strips (marked by \times) and sizeable pulse height in $B(T)$.*

Various combinations of fiber optics, described in Sec. 5.2, were used for the measurements. The most pertinent of these measurements uses an ‘optical chain’ consisting of ~ 160 -cm long WLS fibers, 350-cm long clear fibers (‘set 1’) connected to the WLS fibers via a DDK optical connector, and 100-cm long clear fibers connected to the ‘set 1’ clear fibers using a second DDK optical connector. This chain is similar to that envisioned for the EEMC-SMD (discussed in the previous section) except for two aspects. There is an additional 100 cm of clear fiber in the optical chain

used for the test, resulting in $\sim 10\%$ less light (assuming a 10-m attenuation length) than will be obtained in the EEMC-SMD optical chain. As well, the WLS fiber length is 35 cm longer than the average length planned for the SMD strips, producing an additional $\sim 15\%$ light loss.

Measuring the light yield from triangular cross section strips is challenging because of the thickness variation in the scintillator associated with the triangular profile. An additional complication with the machined strips (that is not as severe for extruded strips), is the elimination of a significant amount of scintillator along the apex-to-base line, especially for the strips cut with the deep fiber grooves. Two separate measurements were conducted to address these problems. In the first measurement, the strip array was oriented horizontally in the cosmic-ray test stand (configuration *a* in Fig. 34). Events were selected that had pulse height less than 1 photoelectron in adjacent strips and ≥ 1 photoelectron in the ‘mirror symmetric’ strip. The latter condition is important to reduce the contribution from MAPMT dark current pulses, accidentally coincident with the trigger signal derived from the large area scintillator paddles not shown in Fig. 34. The event selection criteria chose cosmic ray muons that traversed the strip primarily along the line from the apex to the base of the triangle. In the second measurement, the strip array was tilted by 45° (configuration *b* in Fig. 34) and conditions were placed on the topology of strip pulse heights to select muons that traverse the strip nearly parallel to one of its sides. For all of the measurements, the resulting pulse height distributions were fit to Poisson distributions convoluted with a Gaussian response for the n^{th} photoelectron peak. The analysis strategy is described in Sec. 5.2. The fitted mean of the Poisson distribution is the deduced photoelectron yield from the strip.

The results from the measurements are:

- there is a broad distribution of the photoelectron yield from the different strips. This is attributed to the varying quality of the WLS fiber groove. Another contributing factor is the possibility that the WLS fibers used for light collection had some damage to their cladding layers, resulting from previously threading the fibers through machined grooves.
- on average, no significant difference in the photoelectron yield between the strips with ‘deep’ and ‘shallow’ fiber grooves was observed. This result is the same for data obtained in both ‘tilted’ and ‘horizontal’ orientations. The differences in photoelectron yield were smaller than the strip-to-strip yield variation.
- the photoelectron yield from the ‘tilted’ orientation was on average 60% larger than from the ‘horizontal’ orientation. For the latter, the small photoelectron yield reduces the effectiveness of the neighboring strip veto in selecting muons that traverse the strip from its apex to its base. The resulting pulse height distribution corresponds to an average of cosmic-ray muon paths in the vicinity of the apex-to-base line. The ratio of the photoelectron yields in the two configurations is consistent with producing less light when the muon penetrates in the vicinity of the fiber groove.
- on average, in the ‘tilted’ orientation with the full optical chain, we are observing 1.9 photoelectrons. This number must be divided by $\sqrt{2}$, and corrected for attenuation differences in the optical chain before it should be compared to the required average photoelectron yield, deduced from the simulated $\gamma/\pi^0(\eta)$ discrimination with the EEMC-SMD. The result is 1.8 photoelectron per MIP.

With the available information, only bounds can be placed on the photoelectron yield from the strip design planned for the EEMC-SMD, with the full fiber optics that will be used. The measurements with the D0 extruded strips, with the equilateral triangular profile, provide a ‘soft’

upper bound on the yield of 2.4 photoelectrons per MIP. This bound is soft because of the unknown quality of the strips obtained from D0. The measurements with the machined triangular strips suggest a lower bound of 1.8 photoelectrons per MIP. The light yield might be small because of known deficiencies in machining the scintillator with the slow-spindle-speed end mill. Another concern is that the WLS fibers used for the light collection had previously been inserted and extracted on multiple occasions from fiber grooves. This was necessary because of the limited number of finished pigtailed fibers we have available for tests. The concern arises because of the potential for damage to the fiber cladding when it is threaded through fiber grooves many times.

To establish more precisely the photoelectron yield from the scintillator strips, more tests are required. The first test will require that a new set of strips, machined by a high-speed router, be made. New WLS fibers need to be prepared for light output measurements to ensure that the fiber cladding is undamaged. If the photoelectron yield is found to be adequate, then an initial extrusion of scintillator strips with the planned geometry would be made and the photoelectron yield would be measured from the extruded strips. If the yield from the newly machined strips is found to be inadequate, the fallback position would be to increase the base-to-apex height of the scintillator strips for the EEMC-SMD, while retaining the base length of 10 mm. The present ‘depth budget’ for the EEMC has some contingency that could be used for this purpose.

5.5 Optical QA/QC

We have just begun to define the QA/QC procedures and will rely heavily on the experience of other detector projects. The checks we are considering will include testing of incoming materials, inspection during manufacturing processes, testing of the megatile before assembly and also of the finished megatile assembly and detector as a whole.

First, we will have Kuraray label each sheet of scintillator and provide batch/lot information. We will measure the thickness of each sheet of scintillator at some number of points. Finally we will remove a 1”x1” sample from each sheet of scintillator. The light output of a subset of these will be measured and the rest archived for future testing if questions arise. A computer data base of all this information will be formed and used to correlate the data with the final megatiles.

During manufacture there will be a list of procedure checkoffs, visual inspections and mechanical tests during the various stages. We are considering bar coding each megatile and using a computer to document this information although Fermilab uses a 3 sheet traveling form with each piece.

After assembly the tiles will be checked for light output and cross talk with a radioactive source. Each megatile will be checked by a height gauge to verify that it will fit into the gap between radiator layers.

The wavelength shifting fiber pigtailed and clear fiber bundles will have their own set of tests and inspections before shipping from Michigan State. These include visual inspections during manufacture and final testing with light sources for light output.

Finally after insertion of the megatiles into the mechanical structure we will make tile by tile tests using cosmic rays tracked through the detectors. We have already produced such a tile by tile testing device for the barrel project. It makes use of two planes of wire chambers above the detector and trigger scintillators above and below the detector. This allows multiplexing a number of tiles in one plane into one PMT and using the tracking to determine which one of the tiles was hit. Equipment from IUCF was assembled at Wayne State and used to test the 4 modules currently installed in STAR and will be used for the rest of the modules as they are produced.

Similar procedures will be needed for the SMD modules. This should include inspection of raw materials and light output testing of samples of the extruded strips. During manufacture procedure

and inspection checkoff lists should be used. Light output testing of the completed modules will be needed and finally they will be part of the final assembled detector cosmic tests.

6 Electronics Update

6.1 Overview

Over the last few months, as requirements for the EEMC tower and SMD electronics have become more firmly established, decisions have been made regarding which aspects of the full readout scheme can be taken over directly from the barrel EMC system, which BEMC components can be used only with modification, and where it is advantageous to adopt a completely new approach for the endcap.

In Section 6.2 below, we report recent progress towards selection of the tower PMT and SMD MAPMT, based on measurements performed at IUCF on a number of competing phototubes, and driven by test beam results which dictate more clearly the design specifications which the PMT's must meet. The use of Cockcroft-Walton bases for both the PMT's and the MAPMT's is also discussed. In the following section, progress on several aspects of the common BEMC/EEMC tower electronics is reported, placing particular emphasis on the Tower Data Collector (TDC) that is being developed and prototyped at IUCF. This will serve as the crucial link between the individual tower FEE crates and the STAR DAQ system. A single TDC will service both the barrel and endcap EMC's. Finally, in Section 6.4, we describe an alternative readout scheme proposed for the endcap SMD which will provide a better match to our scintillating strip design, and also allow for a wider dynamic range of signal information. This latter feature, which would be difficult to accommodate using the present BEMC SMD readout scheme, is needed to compensate for larger than expected channel-to-channel gain variations in the SMD, due to contributions from both the MAPMT's and strip-to-strip variations in light collection efficiencies.

6.2 PMT/MAPMT Tube and Base Selection

For the EEMC towers, in which observation of MIP's (both cosmic ray muons prior to beam and energetic charged particles during beam) will play a crucial role in calibration and monitoring, the photomultipliers selected must have high quantum efficiency, good response to single photoelectrons, and fairly high gain. To meet the requirements of the spin physics program, good linearity is also needed.

To make these statements more quantitative, we note that the gain and linearity requirements for the tower PMT are set by the largest signal of interest, corresponding to detection of 150 GeV electrons from W^\pm decay. Given the 6.5% sampling factor for the calorimeter, an expected light output of 2.5 photoelectrons per MIP from each 4 mm thick tile (at 18% quantum efficiency of the PMT), and a MIP energy deposition of 0.8 MeV in the same tile thickness, one can estimate the number of photo-electrons produced as

$$N_{\text{pe}} = (150 \text{ GeV})(0.065)(2.5 \text{ pe/MIP}) / (0.8 \text{ MeV/MIP}) = 3 \times 10^4 \text{ pe}$$

If this charge is to saturate an ADC rated at 1 nC full scale, then the PMT should have a gain on the order of 2×10^5 . With 12-bit digitization, this would place the MIP peak roughly 10 channels above the pedestal. We also note that, assuming a triangular pulse shape of 20 ns duration, a 1 nC integrated charge corresponds to a maximum peak current on the order of 100 mA.

Based on the experiences of other groups and on the manufacturer's specifications, four PMTs were selected for testing as possible candidates for the EEMC tower readout: the 9125B, 9124B, and 9107B from Electron Tubes Limited (ETL), and the R5800 from Hamamatsu. The three ETL tubes are very similar; the only differences are that the 9124B, a "green extended" version of the 9125B, has slightly higher quantum efficiency (20% compared to 18% for the 9125B) at 500 nm

wavelength (near the emission peak of the Y11 dopant to be used in the WLS fibers) and has a higher operating voltage, while the 9107B is simply a shorter (by 25 mm) version of the 9125B.

Measurements of the phototubes' gain and linearity were carried out using a G9732 blue LED located in front of the photomultiplier's entrance window. The LED was driven by a fast pulse generator with an approximately triangular output signal of less than 4 ns FWHM duration, and an amplitude of up to 30 V. Though characteristics of the LED output pulse were not directly measured, measurements taken with faster PMT's, such as the Burle 83101-600 or Hamamatsu H6568, indicated that the light pulse had a rise time of less than 3 ns and a fall time of below 10 ns, and thus should serve as a reasonable simulation of the light output expected from the calorimeter tiles. Neutral density filters (Hoya ND from Tokina Co, Ltd.), positioned between the LED and the PMT entrance window, were used to change the light flux incident on the photocathode for the linearity measurements.

The pulse height distribution of the output signals from each PMT was measured using two integrating ADC's simultaneously: a LeCroy 2249W, with a gate width of up to 2 μ s, and a LeCroy 2249A, with a 10–50 ns gate width whose delay could be adjusted. This combination allowed us to measure the time distribution of charge in the output pulse, and, more specifically, to determine whether the long pulse tails and after-pulsing that had been observed during the prototype test run (see Sec. 3) with the Burle 83101-600 PMT were present in this new set of PMT's being tested.

The voltage-gain characteristics for three of these tubes are shown in Fig. 35, while the pulse linearity characteristics are presented in Fig. 36. Because high linearity is required at high peak currents, all PMT's were tested with so-called 'tapered' bleeder circuits (tapered voltage dividers), which are known to improve pulse linearity by a factor of 5 to 10 compared to an equally divided (linear) circuit. For comparison, the R5800 tube was also tested with a linear voltage divider. Under these conditions, all of the phototubes tested met or exceeded the typical manufacturers' specifications. In measurements of the time distribution of the pulse charge, no significant deviation was found between the wide and narrow integration gate results, so there is no indication of long signal tails or after-pulsing. For all phototubes tested, the output pulses had rise times of about 7 ns and fall times of about 13 ns. More than 90% of the total output charge was contained within two 10-ns wide bins.

Three of the phototubes were also compared with regard to sensitivity to magnetic fields. With the PMT mounted in one of three orientations with respect to the field direction, the field was increased until the output gain was reduced by a factor of 2. These field values (in Gauss) are summarized in Table 6.1.

The primary conclusion from these studies is that all of the photomultipliers tested have pretty much the same quantum efficiency, single photo-electron response, and timing characteristics, and (when combined with a tapered voltage divider) all of them meet or exceed their specified limits on gain and linearity. The R5800 tube from Hamamatsu is the smallest of the four, and can tolerate somewhat higher magnetic fields, especially when oriented transversely to the field. On the other hand, it has a much higher operating voltage and much lower gain. At a more practical level, the R5800 is also about twice as expensive as the 9125B and 9107B tubes from ETL. The ETL tubes also come with a conductive coating and insulating black plastic sleeve, which improves noise characteristics of the PMT and makes for increased ease in handling. We thus plan to use the ETL 9107B PMT's. These then allow use of identical bases and readout electronics as for the barrel EMC PMT's.

Similar tests of other types of photomultipliers—in particular, the 16-channel Hamamatsu H6568 MAPMT, to be used in the shower maximum detector readout—are currently underway.

Concern over the heat load that resistive bases would generate has led us to consider the use

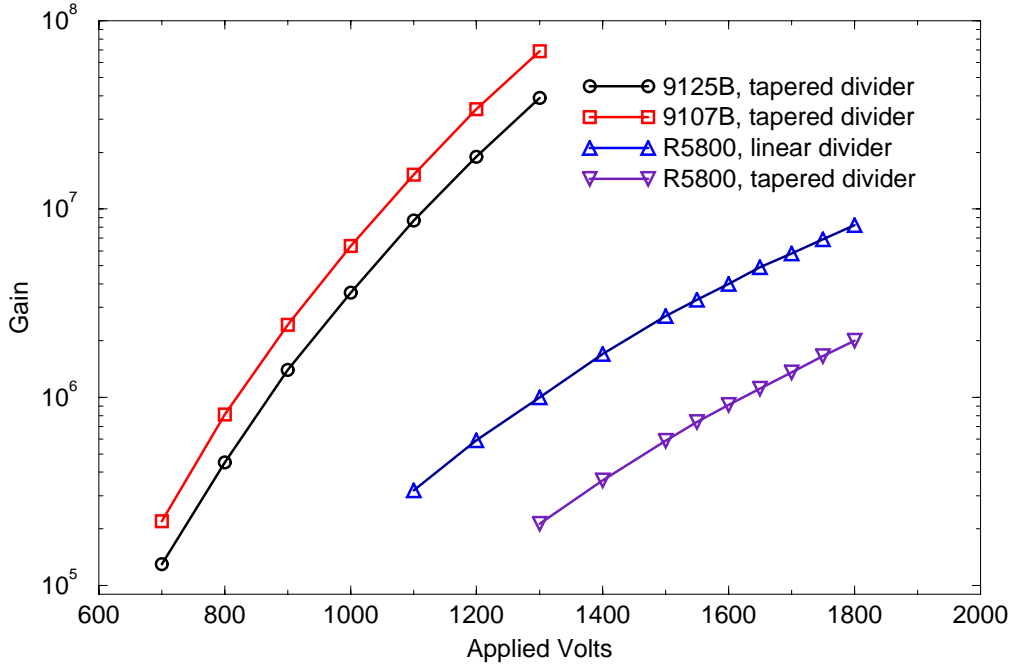


Figure 35: *The gain vs. voltage characteristics for three of the candidate tower PMT models tested at IUCF.*

of Cockcroft-Walton (CW) bases. Excess heat will clearly exacerbate PMT cooling problems, as the tubes and bases must be heavily shielded in order to operate reliably while mounted on the STAR magnet pole tip. Given their greatly reduced (factor of ~ 10) power consumption, CW bases are better suited to provide the linear PMT operation needed for the high peak currents that characterize the highest energy showers of interest.

CW bases appropriate for the tower PMT's have been produced for the BEMC by the UCLA group, and will also be produced by that group for the EEMC. For the Hamamatsu H6568 MAPMT to be used with the SMD strips, CW bases are under development by the Dubna group. This group has previously designed and built similar systems, capable of powering up to 10^4 PMT's, with high voltages stable to 0.05% (read out to 10-bits) and dissipated power per channel of less than 0.12 W. Preliminary (and comparable) design specifications have been established for the H6568 MAPMT. Controls are supplied through standard RS-232-C serial lines. The voltages will be controlled by

Table 1: PMT sensitivity to magnetic field strength

PMT type	along axis	at 45°	transverse
R5800	11.4	4.1	3.3
9125B	11.0	3.2	1.9
9107B	11.0	2.4	1.8

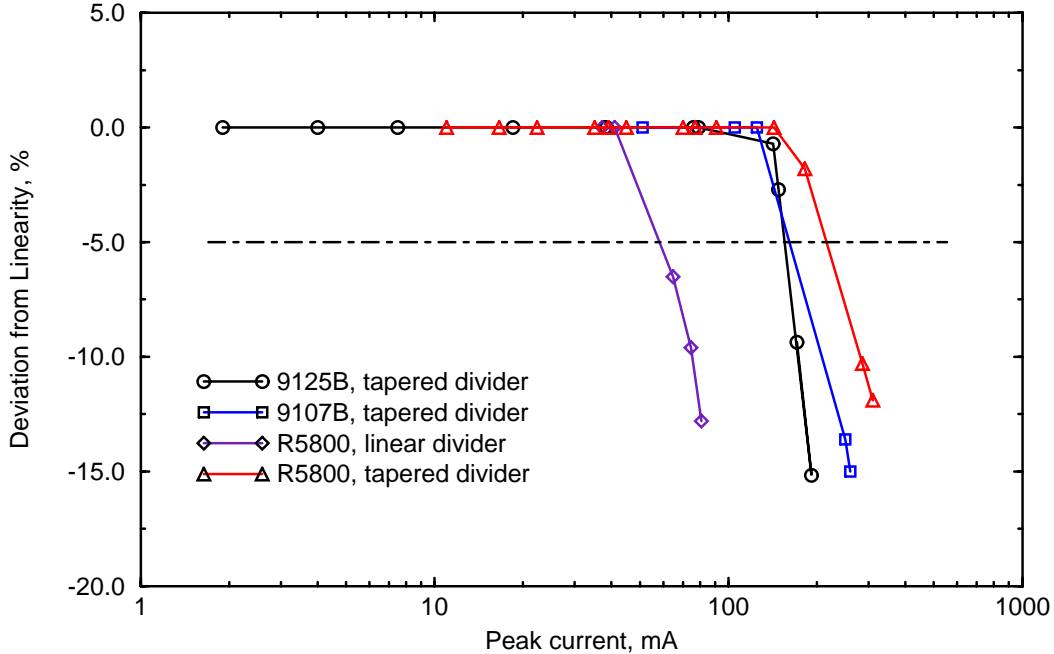


Figure 36: Measured linearity characteristics for three PMT models tested at IUCF.

a DAC made from the RC-filtered pulse-width modulation (PWM) output of a PIC16C873 microcontroller. The controller will monitor HV, power consumption, and housing temperature with an internal 10-bit ADC, and will contain a high speed control logic FPGA whose configuration can be easily downloaded. This will allow for external reprogramming of the PIC. Prototype Dubna CW bases will be used with the prototype SMD detector in the next beam test at SLAC.

6.3 Progress on BEMC Electronics

For the 720 channels of EEMC tower electronics, we will use FEE cards identical to those used for the 4800 channels of the barrel. To satisfy dynamic range requirements for the endcap, all cards (for both barrel and endcap) will digitize input signals to 12 bits (rather than using the 10-bit ADC's in the original barrel design). A more subtle modification was needed to ensure that 'pre- and post-crossing' tower information could be recorded. Due to the very large (~ 2000) number of tracks that will be contained within the TPC volume during high-luminosity pp running, it is essential that all EMC information (tower and SMD) be read out for the RHIC beam crossings that occur immediately before and after the crossing of interest, i.e., that which generated the L0 trigger. Detailed justification for this requirement can be found in Section 7.2 of [1]. To provide this capability, the output timing strobe for the tower digitizer card FIFO (in which the 12-bit tower data is stored for the 64 most recent crossings) will be generated by an FPGA, rather than a simple clock with a hard-wired delay. This will allow for multiple strobing of the FIFO, so that tower information from several consecutive crossings can be passed along to DAQ. The pre- and post-crossing SMD information will also need to be recorded; this capability will be easily

accommodated by the new SMD readout scheme described in the following section.

A significant amount of effort has been directed at IUCF toward the design and construction of the Tower Data Collector (TDC), which is the crucial link between the individual tower FEE crates and the STAR DAQ system. A schematic layout of the TDC is shown in Fig. 37. A single (expandable) TDC will service both the barrel and endcap EMC's. The TDC will be physically located on the STAR electronics platforms and ultimately will be receiving the digital data (via fiber optic cable) from 30 BEMC FEE and 6 EEMC FEE crates located on the back-leg iron and poletip of the STAR magnet, respectively. The data collector derandomizes the information and stores the data in a memory designed to accommodate a total of 4096×5520 locations of 12 bit data, corresponding to 4096 trigger tokens and 4800 EMC + 720 EEMC tower channels. The TDC also serves to pass the full event data on to the level 2 trigger. Upon receipt of a L2 trigger accept, the TDC sends the selected event data information to STAR DAQ.

The concept for the TDC has evolved over the last year in reaction to other electronics and trigger decisions. The design of the TDC is modular and consists of a series of identical receiver boards, a single transmission board, associated VME bus, 6U crate, and processor. The modularity of the receiver boards, each of which can read out 6 FEE crates, means the initial barrel EMC patch installation in year 1 RHIC running can be handled with one receiver board and one transmitter board. The system is then expandable to accommodate the full barrel plus endcap readout (5 receiver cards for 30 barrel crates plus one receiver card to accommodate the endcap tower readout).

The TDC serves not only its original purpose as a data collector, but since it now receives the FEE data quickly (crate to TDC transmission time $18 \mu\text{s}$), it must act also as a token addressable memory for subsequent trigger decisions. That is, because the data is resident in the TDC well before all trigger decisions subsequent to L0 are complete, the TDC must perform a "scorecard" function, keeping track of the data for which trigger decisions are pending, aborting transfer to L2 upon L1 reject, and otherwise appropriately treating data for which trigger decisions are being (or have been) made. A large capacity FPGA on the transmission board will handle the scoreboard and other data manipulation tasks.

A single channel of the complete TDC system has been successfully prototyped, including the construction of "test" fixtures capable of exercising the system at the maximum data rates (60 MHz to L2 and 40 MHz to DAQ). A receiver PCB layout is nearing completion and will be sent for manufacture shortly. First receiver test boards should be available by the beginning of March 2000.

6.4 SMD Readout Scheme

For the endcap SMD strips (and for the two preshower layers—these are all treated the same in the electronics), use of MAPMT's to amplify the scintillator signal already dictates that the input shaping electronics differ substantially from that used for the barrel gaseous SMD. Moreover, recent studies at IUCF of variations in both the intrinsic anode-to-anode MAPMT gains, and in the strip-to-strip light collection efficiencies through the full optical path, suggest that the 10-bit digitization firmly embedded in the barrel SMD readout electronics design will not be sufficient for the endcap.

To address these issues, we plan to replace the H6568 manufacturer's resistive MAPMT base with a unit that contains a Cockcroft-Walton base (see Section 6.2 above) integrated with a 'complete' FEE card. The latter will provide 16 channels of anode signal amplification and shaping, analog storage on a cycling switched capacitor array (SCA), and 12-bit ADC conversion. The digitized data will then be passed to a MUX card for temporary storage, with eventual transfer to an SMD Data Collector (SDC). The SDC plays the same role for the SMD (and preshower) data

EMC Electronics 10/25/99 Draft

1.1.3 Tower Data Collector Overall

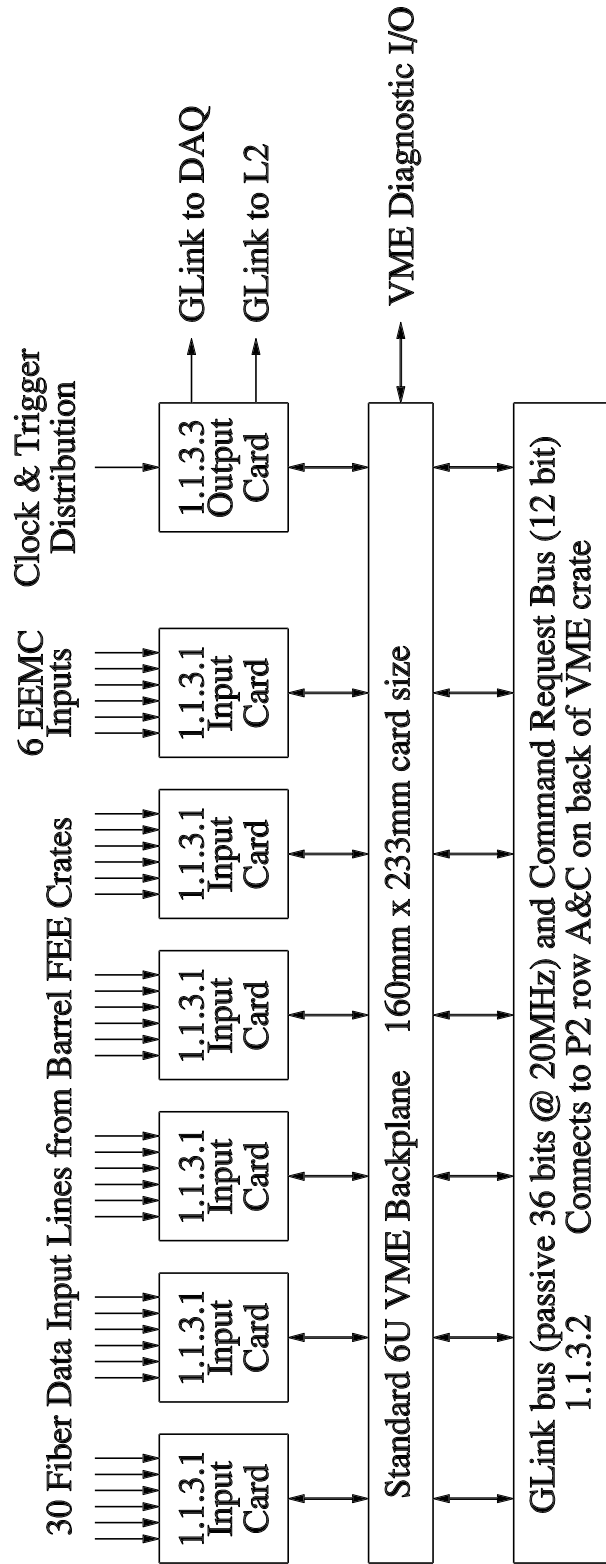


Figure 37: Schematic illustration of the Tower Data Collector that will collect information from both the barrel and endcap EMC front-end electronics, before passing it on to the Level 2 trigger and DAQ.

as does the TDC for EMC tower data, and will be identical in design. The proposed overall layout of the SMD electronics is summarized in Fig. 38, while the electronics intended for incorporation within the MAPMT bases is shown in more detail in Fig. 39.

The input signal shaping will have a time constant sufficiently fast ($\tau \approx 50\text{--}80$ ns) that data can be usefully strobed into the SCA at the RHIC crossing frequency of 9 MHz, yet not so fast that time jitter (due to varying fiber lengths, for example) will compromise pulse height determination. At any given time, the SCA will thus contain voltage levels proportional to the integrated current pulses for the most recent 128 RHIC crossings for 16 SMD strips. The SCA control logic (clocking and trigger instructions) will be sent from a Xilinx FPGA, which will offer great flexibility in the choice of data set to be processed (thereby easily satisfying the pre- and post-crossing data requirement). The requested data will be sent sequentially to a serial 12-bit ADC, which will convert in $1.7 \mu\text{s}$ and pass the digitized data along to an SMD MUX card.

The MUX card stores and accumulates the encoded data, and can perform simple data manipulations (*e.g.*, pedestal subtraction). The data set is then sent over optical fiber to the SMD Data Collector. The SDC uses multiple input and a single output card which are identical to those used in the TDC, thus saving on engineering costs (in addition to other parts costs).

To digitize and store the data from three consecutive beam crossings for the 16 input channels will require roughly $100 \mu\text{s}$, with transmission to the SDC in about $40 \mu\text{s}$ (these can occur in parallel if no data manipulation is performed in the MUX). The Data Collector can pass the entire SMD data volume to the L2 trigger in about $200 \mu\text{s}$, again operating in parallel. Overall, L2 should have all the SMD data (3×7200 channels) and preshower data (3×1440 channels) in less than $250 \mu\text{s}$ from the initial L0 trigger. The availability of EEMC SMD data at Level 2 provides greater flexibility in designing triggers for the high-luminosity pp running.

EEMC SMD Electronics 2/7/00 Proposed

4.5.4.4 Shower Max Electronics Overall

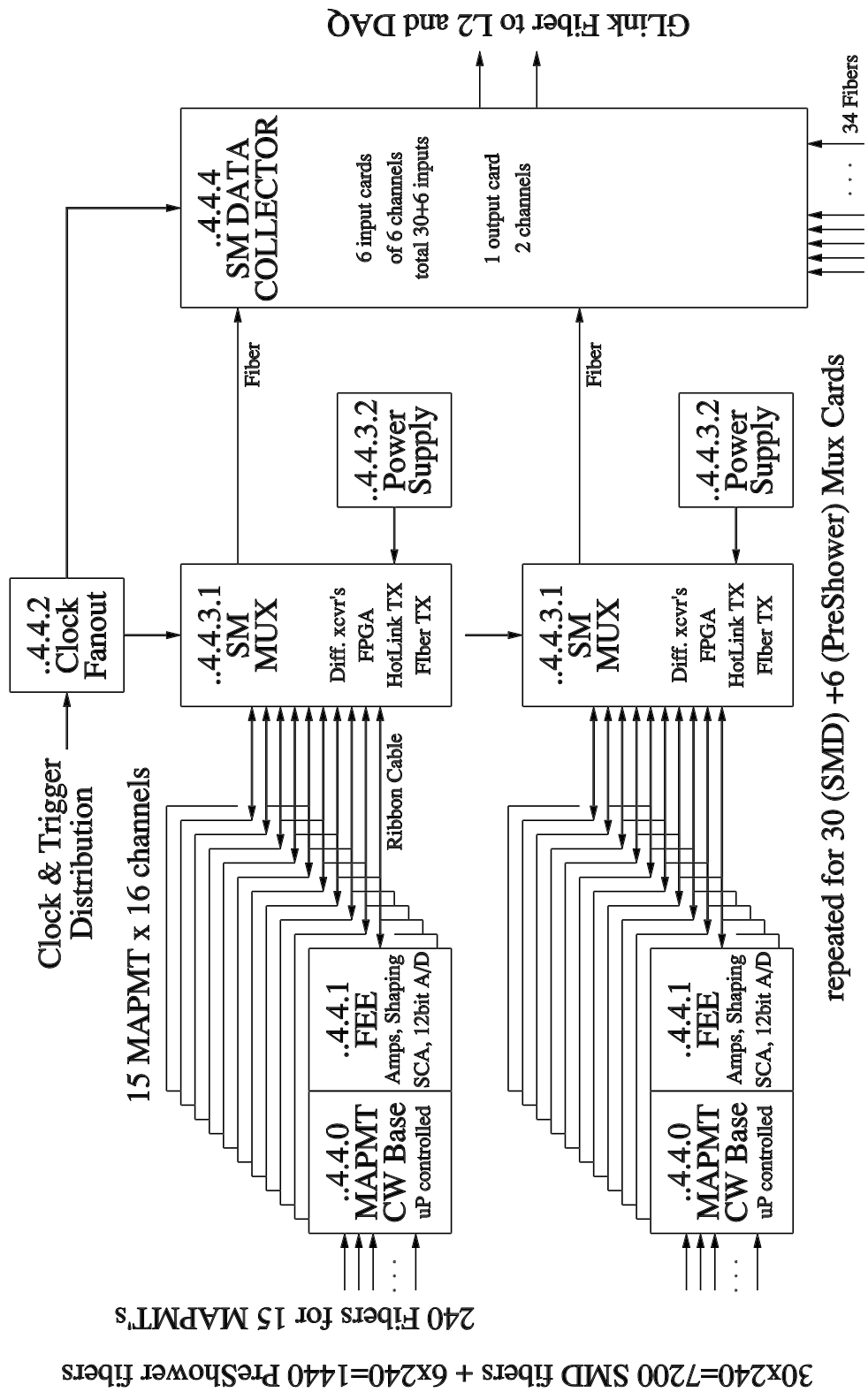


Figure 38: Schematic illustration of one possible layout of the proposed SMD electronic architecture. The FEE cards would be incorporated within the CW bases for the MAPMT's.

7 Calibration Issues

7.1 Overview of Current Status

For the last few months, calibration efforts have focussed primarily on two components of a complete calibration and monitoring strategy: (1) developing methods for ‘pre-beam’ gain adjustment, *i.e.*, ensuring that initial PMT high voltage settings, for example, are sufficiently well matched that all processes of interest are kept within the range of the electronic acceptance, and will not introduce any significant bias when triggering on high p_T photons or electrons; and (2) designing ancillary systems that can provide ‘yes/no’ tests of all components in the optical chain, as well as information on long-term gain stability for specific devices in the chain. A third, and equally critical, aspect of calibration involves establishing absolute (to within $\pm 2\%$) energy normalizations, preferably at several different values of tower energy deposition. The large volume of π^0 data that will be accumulated ‘parasitically’ during direct-photon data taking has been shown previously [1] to be adequate for this purpose, except at the very highest energies where rarer processes, such as coincident e^+e^- detection from Z^0 decay, will be needed. Use of these latter techniques will require additional simulation.

To make progress toward these goals, we held a workshop in mid-September on “Calibration Techniques for Electromagnetic Calorimeters,” in which members of several of the larger detector collaborations (ZEUS, CDF, D0, and PHENIX) presented their views and experiences regarding which calibration techniques have worked, what could have been done better, and how readily these methods could be adapted, if at all, for use in the STAR Endcap EMC. A summary of these discussions, and some of the conclusions reached relevant for the EEMC, are presented in Section 7.2 below. Based largely on the results of this workshop, we have since formulated a more comprehensive plan for the overall EEMC calibration, incorporating several distinct subsystems that will address the three primary concerns mentioned in the preceding paragraph. This scheme is discussed in detail in Section 7.3.

The single most complex, but we believe ultimately most useful, component in this plan is a laser-based system in which UV light is sent directly, via a network of UV fibers coupled to ‘leaky’ optical fibers, into every tile layer in every tower, as well as to every scintillator strip in every SMD module. The required set of beam splitters, attenuators, and (possibly) mechanical slits will provide great flexibility in terms of which towers (and SMD strips) are illuminated, and how the light is distributed from layer to layer within each tower, thus allowing simulation of the tower response to various particles (MIP’s vs. e.m. showers) over the full energy range of interest. Additional features are described in Section 7.4. For diagnostic and monitoring purposes, though, the laser network will be supplemented by other systems that focus more narrowly on specific components in the optical chain, such as controlled charge injection into the electronic front end, and an array of pulsed LED’s that will feed into every PMT and MAPMT. Narrow, thin-walled steel tubes will be installed to accommodate movable (and removable) radioactive sources in a limited capacity. See Section 7.3 for details.

7.2 Summary of the IUCF Calibration Workshop

A two-day workshop on Calibration Techniques for Electromagnetic Calorimeters was held at Indiana University on September 17-18, 1999. The goal of the workshop was to develop a set of practical and effective strategies for calibration of the STAR endcap EMC, including its SMD and preshower layers. To help in this effort, representatives of several other detector collaborations were invited to present some of the techniques and procedures that have already been employed, or

are being considered, for use in similar devices. Though many aspects of the complete calibration scheme were discussed, the primary emphasis was on ‘pre-beam’ calibration methods, both relative and absolute (the latter involving transfer of cosmic-ray or test beam standards), and the use of dedicated subsystems for monitoring the integrity of the full optical chain.

After a brief overview of the EEMC design and calibration requirements, much of the first day was devoted to presentations on calibration techniques currently in use on other EM calorimeters. To gauge the extent to which radioactive sources could prove useful, Jim Crittenden from Bonn discussed the ZEUS detector at HERA, which differs significantly from the other EMC’s in that depleted uranium is used for the converter sheets. The associated radioactivity, distributed uniformly throughout the calorimeter volume, tests every component of the optical system, from scintillator to phototube, and is highly sensitive to aging effects in either. The ever-present signal is also used to carry over absolute calibrations established with test beams. A major drawback to such a system—beyond the obvious cost, machining, and safety issues—is the inability to *remove* the source, so one could examine, for example, the PMT outputs (dark current) in the absence of an essentially constant DC current. It was emphasized that to fully exploit the benefits offered by a distributed source, one must ‘design it in’ from the beginning; much of the ZEUS front-end electronics is specifically tailored to deal with and take advantage of this feature of the calorimeter.

From Don Lincoln, representing D0, experience with their forward preshower detector was of particular interest, in that this device, like the EEMC SMD design, consists of alternating layers of extruded scintillating strips, triangular in cross section, with embedded WLS fibers (though the detectors differ significantly in their readout schemes). While there was great interest in trading inside ‘tips’ regarding the fabrication and mechanical assembly of these strip arrays, discussion centered on the two-component calibration plan developed by the D0 group. As a yes/no test of individual channel operation (from WLS fiber through to DAQ), light from blue LED’s is fed via clear fiber into bundles of the WLS fibers. While channel-to-channel comparisons are not useful (due to variations in light injection efficiency into the bundles), *relative* energy calibrations for each channel can be monitored with this system from the WLS fiber onward, including the VLPC readout. Channel-to-channel gain matching is done using MIP tracks, both those that fire a single strip in a layer (and therefore pass through the full ‘height’ of the triangle), and those that share energy between adjacent strips, two techniques that have direct application to our SMD. For D0, MIP’s also provide a close-to-final ($\sim 3\%$) absolute calibration, though reconstructed masses from in-beam data are used to set the overall scale in the energy regimes of primary interest.

Mike Lindgren of CDF was asked to speak on calibration techniques used for their recently upgraded endplug calorimeter, which is very similar in tower geometry and mechanical structure to that envisioned for the STAR EEMC. It also includes a fairly complex, multi-pronged calibration scheme. For calibration and monitoring of just the electronics, a precision (16-bit DAC-controlled) current source injects charge directly onto the front-end integrator. Going further upstream, a pair of nitrogen lasers flash light (wavelength matched to that from scintillators) directly into each tower PMT and preshower MAPMT. The lasers also illuminate monitor PMT’s that view NaI crystals loaded with Americium for normalization and long-term stability checks. This laser system is used to equalize the initial tube gains to within about 1% prior to each run. However, the most comprehensive calibration system (but also acknowledged as being the most troublesome to maintain) is a set of thin-walled stainless steel tubes that pass over every individual tower tile, through which 3 mC ^{60}Co sources can be pulled on wires. The highly localized sources measure the tile-by-tile scintillator response, after the tower PMT’s have been gain equalized with lasers, as described above. Together, these two systems determine relative gains for all components of the calorimeter towers; used in conjunction with cosmic ray and test beam data, absolute energy

scales and linearity checks can be established. As part of an overall calibration and monitoring philosophy, Lindgren emphasized the key role played by extensive QA/QC during all stages of tile machining and assembly.

Finally, Sebastian White described the calibration schemes used on the EMC for the PHENIX detector, located at RHIC. As with other calorimeters, cosmic ray MIP's (muons passing either transversely or axially through the EMC) provide both high-precision interchannel *relative* gain matching, as well as initial (pre-beam) *absolute* gains to within about 5%, with in-beam data setting the final calibration scales. For monitoring overall gain stabilization, however, PHENIX has developed a moderately flexible, highly distributed laser system, in which a network of optical fibers allows for direct UV excitation of all scintillator sampling layers. Light pulses from the Nd:YAG laser are split at three different stages, with PIN photodiodes providing reference signals at each stage. Each UV fiber is ultimately coupled to a 'leaky' fiber which extends down the center of a 4-tower module. Scribe marks machined along this fiber allow light to 'escape' into the surrounding tile layers; by varying the spacing between scribes, the longitudinal energy deposition profile typical of a 1-GeV e.m. shower can be simulated, to gauge accurately the overall tower response. Polarizing filters on the laser output can attenuate the light pulses by up to two orders of magnitude in a controlled, reproducible manner, so that system linearity can be monitored over a wide range. Though essentially every element of the optical chain is tested with this system (other than actual ionization within the scintillator), it is difficult to perform yes/no checks of the integrity of light collection from individual tiles.

Based on the above information, and keeping in mind the unique requirements of the STAR endcap EMC, various calibration methods were considered, debated, modified, and sometimes rejected in the ensuing workshop discussions. By the end of the workshop, though, several distinct themes had emerged, which have since been 'fleshed out' to varying degrees. First, it became clear that no single system could satisfy all the needed pre-beam and monitoring / diagnostic requirements, and that the multi-pronged approach used by CDF should be adopted as a general working philosophy; but at the same time, effort should be concentrated into the single system that provides the most comprehensive check of the complete endcap EMC, *i.e.*, the one that comes closest to testing the full optical chain, front-end electronics, and data readout modules. While radioactive sources test essentially all aspects of the optical system, special electronics are needed to integrate the DC current from the PMT's. A UV laser network, similar to that employed in PHENIX, does not induce ionization, but produces light signals within the scintillators that are otherwise processed in a manner identical to those due to a true e.m. shower. For this and other reasons outlined below, it was felt that a laser network should form the key component of the EEMC calibration system, augmented by additional, simpler systems that would provide largely diagnostic information on specific elements in the optical / electronic / readout chain.

7.3 A Calibration Scheme for the STAR EEMC

In this section, we present an overview of the devices we will use and the procedures we will follow to calibrate and monitor the performance of the calorimeter towers, SMD strips, and preshower layers that make up the EEMC. The methods are described in roughly the order in which they would be implemented for a 'cold start' calibration.

For the EMC towers (both endcap and barrel), the FEE tower digitizer cards contain a 12-bit DAC-controlled charge injection unit for each input channel. This precision current source, when externally triggered, injects a known charge to an input FET (SD210) which feeds the same amplifier, gated integrator, and 12-bit flash ADC used for PMT signal processing. This sub-

system will enable yes/no checks and linearity tests of the signal shaping, digitization, and readout electronics, both pre-beam and during data acquisition.

Going further upstream, an array of pulsed LED's will flash light into fibers that go directly to each tower PMT. The LED fiber light will be mixed with, and treated the same as, the light from the 24 fibers coming from the individual tiles within the tower. This system would be used primarily for diagnostic purposes, since channel-to-channel variations would be too large for useful gain setting. Once gains are established, however, long-term PMT gain stabilization would be monitored by testing for *relative* changes in tube output signal. LED pulses will be similarly mixed with the fiber feeding one pixel on each preshower and SMD MAPMT.

The 'centerpiece' of the EEMC calibration, though, will be a UV laser-based fiber network, modelled somewhat after that used by PHENIX. Details of the system architecture will be given in Section 7.4, but a few distinguishing features can be noted here. The light from a single Nd:YAG laser will be split in several stages to generate pulses simultaneously at several intensity levels. By routing these appropriately before connection to 'leaky' fibers (one fiber per 6° megatile section), it will be possible to simulate a variety of depth profiles in the calorimeter towers. For diagnostic purposes, the "profile" could also involve illumination of a single (or a small number of) tower layers. Laser and splitter stability will be independently monitored with a series of PMT's that simultaneously view a source-illuminated scintillator. This laser/fiber network will provide our best (pre-beam) check of linearity for the complete optical/electronic/readout chain. It will allow extension of absolute calibrations from cosmic rays over the entire dynamic range of interest for both towers and SMD strips. Calibrations determined in this way will be compared to test beam results for our 12-tower prototype detector, after the laser system is developed.

At this point, the role of radioactive sources in the EEMC calibration scheme is rather limited, and strictly diagnostic. Narrow (~ 1 mm diameter), straight (if possible), thin-walled source tubes will be embedded in the fiber routing layers that are adjacent to each megatile. Because the source radiation will penetrate several layers of the lead converter sheets, only every third or fourth routing layer will have such a tube. Sources inserted in these tubes will be used during assembly of the EEMC for QA/QC and diagnostics: a calibrated (in length) 'hot' wire will be inserted in these tubes for yes/no tests of individual tile/fiber integrity. As indicated earlier, this will require use of a dedicated, stripped-down acquisition system to integrate the low-level DC PMT currents. The sources would be used very sparingly after the EEMC is installed within STAR, since access to the tubes would require partial disassembly of the detector.

The complete set of devices described above should be sufficient to set relative gains among the 720 EEMC towers. In combination with cosmic rays, we anticipate that the system will permit absolute pre-calibrations of both tower and SMD strip gains to considerably better than the $\pm 10\%$ level needed for a "cold start." Indeed, the results of the prototype beam test (see Sec. 3.5) suggest that use of cosmic rays alone already approaches that level. We will rely on the comparison of cosmic ray and laser data acquired *in situ* within STAR, with the solenoid power off *vs.* on, to calibrate the few percent change in ionization-induced scintillation light expected [17] to arise from the ambient field. Previous studies [17] have shown that this shift is not apparent when the scintillator is excited by UV light. However, the laser system will monitor well any field-induced PMT gain shifts.

Final absolute gains for each tower must be established to $\approx \pm 2\%$ accuracy using actual STAR data. Several methods for doing so are described in detail in [1], and will be mentioned only briefly here. The goal is to reconstruct invariant masses at different scales. At the low end, one searches for π^0 decays in which the two photons produce e.m. showers in spatially separated towers. Even with fairly stringent software requirements (each shower far from a tower boundary, no other

showers nearby, etc.), such events will be abundant in the high- p_T data sample. By looking for charged ρ decays into $\pi^\pm \pi^0$, one can determine the charged pion 4-momentum using the TPC, and thereby ‘tag’ the π^0 . If both decay photons shower in the same calorimeter tower, one can fine-tune the tower gain. Studies of these processes will also allow us to determine the probability for π^0 conversion upstream of the preshower layers, which simulations indicate must be known to within 15% for effective π^0/γ discrimination. Absolute calibrations at even higher mass scales, *e.g.*, using $Z^0 \rightarrow e^+e^-$, require further simulation to judge feasibility and determine the level of statistical precision that can be achieved.

For the endcap SMD, consisting of scintillator strips read out via 16-channel MAPMT’s, one channel of each tube will view an LED pulser. Extensive QA/QC will determine the relative gains of each of the 16 anodes for each MAPMT prior to installation. The primary monitoring system for the SMD will be a set of leaky fibers from the UV laser network, with 5 fibers sent to each plane of a 30° sector. Each leaky fiber will be run along the outer edges of the sector, and illuminate roughly 60 strips from the end housing the mirrored end of the WLS readout fiber.

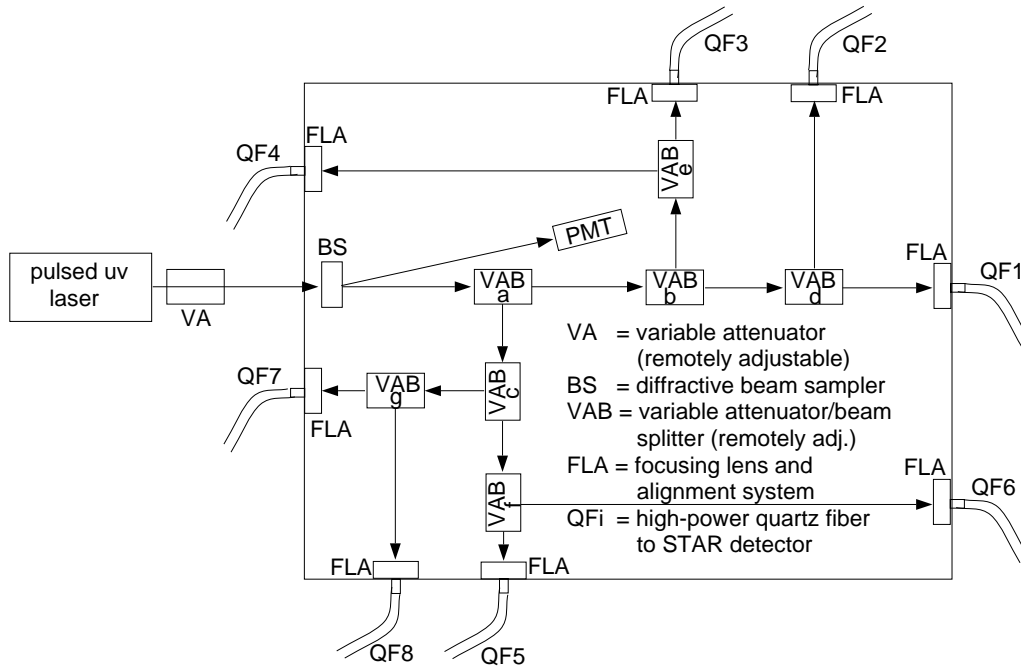
7.4 The EEMC UV Laser System

An overview of the UV laser network envisioned for the endcap EMC, and its primary uses for calibration, monitoring, and diagnostics, has been presented in the previous section. Here, we provide additional technical detail on the system architecture and implementation.

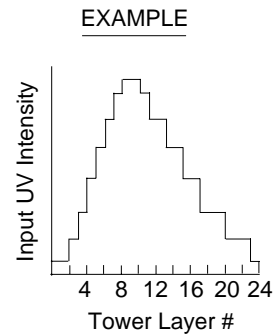
Starting at the beginning: to simulate the energy deposition of ionizing radiation in the various scintillator tiles and strips, the laser must deliver short ($\lesssim 10$ ns) light pulses at UV wavelengths. It must have sufficient power to illuminate a significant fraction of the detector at intensities similar to those due to a high-energy (~ 150 GeV) e.m. shower, at rates of up to 10 Hz. For practical reasons, it must be externally triggerable, remotely addressable, and relatively maintenance-free (as it must be mounted on the detector platform, and will not be easily accessible during running). A Nd:YAG laser, tuned to deliver beams at its third harmonic of 355 nm and capable of delivering at least 1 mJ per pulse, meets these requirements. Relatively small lasers with 5–10 times this power output are commercially available for \approx \$15K.

The first stage of beam manipulation will also be carried out on the STAR platform, and is illustrated schematically in Fig. 40. The full pulse will pass through a variable attenuator that can be remotely (and reproducibly) adjusted to provide up to two orders of magnitude variation in output energy. The attenuator consists of a rotatable half-wave plate that precesses the incident linearly polarized light from its initial horizontal orientation, followed by a birefringent crystal that transmits only horizontally polarized light. The attenuated beam is then passed through a branched three-level hierarchy of variable attenuator/beamsplitters (similar to the primary attenuator, except that the vertically polarized light is reflected rather than absorbed); by using seven of these devices in a cascade structure, the beam can be divided (with little loss) into eight arbitrary intensity levels. This flexibility will allow, after further splitting and routing as described below, for simulation of a wide range of depth profiles (from MIP’s to high-energy e.m. showers) in selected subsets of towers.

The eight beams are transported from the electronics platform to the STAR detector via UV-transparent fused silica fibers (silica cores and silica cladding). These fibers, like all of the ‘first-stage’ optics, must tolerate high power, and hence must be rated for high damage thresholds. Fibers of 400 μm core diameter would be sufficient for the full 7 mJ potentially available from the laser. At the poletip, the light from each of the eight quartz fibers would be equally divided into 180 (or 240) parts using two successive stages of multi-spot diffractive beam splitting. With a total of 60 6° sectors, and 24 tile layers in each, one can thus illuminate 3 layers in *each* tower with one of



Beam Distribution Center Output #	Relative Output Intensity ($f_i \equiv$ transmittance at VAB i)	Routed to Tower/SMD layer #s
1	$f_a f_b f_d$	9, 10, SMD u*
2	$f_a f_b (1-f_d)$	1, 2, 24
3	$f_a (1-f_b) f_e$	8, 11, SMD v*
4	$f_a (1-f_b)(1-f_e)$	3, 21, 22, 23
5	$(1-f_a) f_c f_f$	7, 12, 13
6	$(1-f_a) f_c (1-f_f)$	4, 18, 19, 20
7	$(1-f_a)(1-f_c) f_g$	6, 14, 15
8	$(1-f_a)(1-f_c)(1-f_g)$	5, 16, 17



* Use 5 leaky fibers per SMD sector/plane. This gives one u and one v leaky fiber per 6° phi sector of EEMC. If only one of the five fibers is pulsed at a time, then typically no more than 4 anodes on a given MAPMT should fire simultaneously.

Figure 40: Schematic illustration of the primary light distribution center for the proposed UV laser monitoring system. The primary variable attenuator will be housed within the laser, and will allow adjustment of overall pulser light intensity over two orders of magnitude. A series of seven variable attenuator/beamsplitters will then allow splitting of the beam into eight parts, with remotely adjustable splitting fractions. A possible routing of the eight resultant beams to tower and SMD layers is indicated, permitting simulation of depth profiles appropriate to electromagnetic showers or MIP's or illumination of only a few layers at once. Each of the eight beams will be subsequently split 180 or 240 ways, to feed all EEMC sectors, on the STAR poletip.

the eight remotely-adjustable intensity levels. Two of the eight fibers are split 240 ways to provide light in addition for the SMD u and v planes, as indicated in Fig. 40.

One final aspect of the splitting/distribution system is not yet at the conceptual design level. It would be highly advantageous to illuminate only a subset of the towers with any given pulse (though every tile layer *within* these towers would receive light from the same pulse at one of eight intensities). Because the last stage of beam splitting is performed with diffractive lenses which generate patterns of light (basically, spatial arrays of ‘dots’), one could consider a mechanical slit system which passes over and intercepts the light from the majority of these dots. This would not only reduce the data volume (only 90 towers would fire per pulse, rather than the full 720), but will be essential for the SMD, since the MAPMT response may be significantly distorted if all 16 inputs receive signals simultaneously. While a moving slit system has a conceptual simplicity, implementation and maintenance could be problematic, and more robust methods for achieving similar results are being considered.

Transport of the low-power light pulses from the distribution hub on the STAR poletip to the detector itself can be handled using UV-transparent plastic fibers, of 1-mm core diameter. This same type of fiber can also be used for the ‘leaky’ fibers, which provide the actual light to the scintillating tiles and strips. For the towers, the leaky fibers will be fed through radial grooves machined into the fiber routing layers adjacent to each megatile (see Fig. 29). Several scribe marks will be made at each of 12 locations along the fiber (there are 12 tiles per megatile), all on the same side of the fiber. During insertion, the fiber must be oriented so that this side faces the megatile. For the SMD planes, each of the five fibers will have a different pattern, though all 30° modules will be identical. Insertion and alignment of leaky fibers into the SMD will be fairly time consuming, and will require extensive QC procedures to be developed.

A small number (10) of additional PMT’s would be needed for monitoring the performance of the laser network. By comparing the laser signal against the integrated current from a scintillator illuminated by a radioactive source, one could correct for overall pulse-to-pulse intensity fluctuations, and also monitor the initial stage of beam splitting into eight intensity levels. Such devices are easily incorporated into the present design.

Equipment cost estimates for the laser system, included in the budget presented in Sec. 9, are based on commercially available lasers, optics and optical fibers.

8 Integration/Interface with STAR/RHIC

8.1 STAR Integration Limits

An integration review of the EEMC project will be held by the STAR collaboration in Spring 2000. The nominal integration volume available to the calorimeter itself, and to the EEMC PMT's and electronics to be mounted on the rear of the poletip, are indicated in Fig. 41. As the technical design of the EEMC has progressed, several significant changes have occurred in our estimation of where we stand with respect to the nominal integration limits.

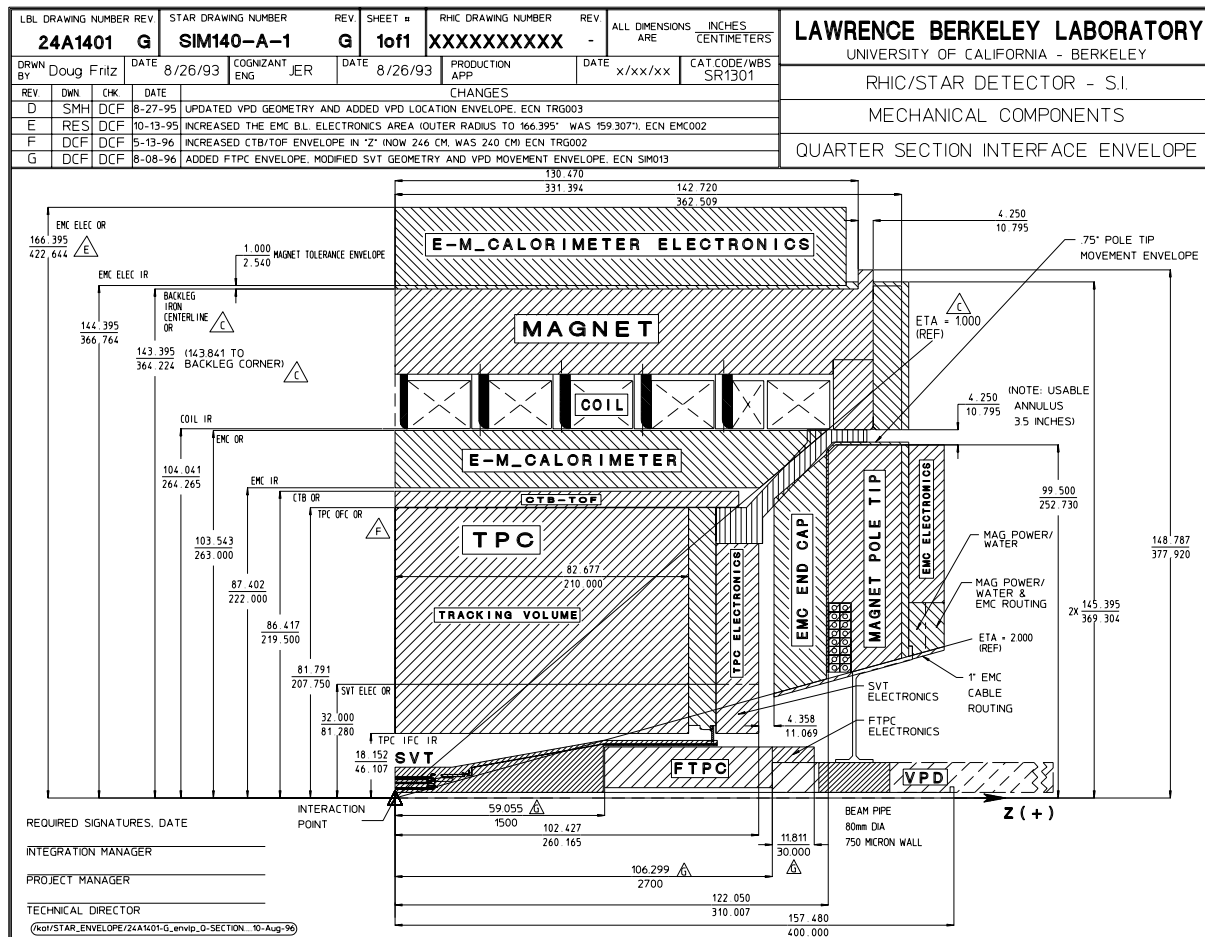


Figure 41: Quarter section interface envelope drawing for the STAR detector, indicating the depth and η limits currently allowed for the EEMC and its PMT's and associated electronics. Note that this version of the drawing is not quite up to date: it shows a small interference between the services volume at $\eta = 1$ and the endcap integration volume, which has since been resolved in favor of the endcap. We furthermore will request, and expect to receive, a small extension of the EEMC integration volume toward the TPC electronics, as discussed in the text.

The most serious change concerns the depth budget for the calorimeter itself. The overall depth had been estimated in the CDR [1] as 35.6 cm, about 2 cm under the space allowed by STAR.

The present design, outlined in Sec. 4, would require a total depth of 40.3 cm for the same basic active volume. Discussions with the STAR Operations Group have indicated that an appropriate relaxation of the integration limit (to 41.0 cm, to permit a small amount of additional flexibility) is likely to be approved, but we will wait for the outcome of the EEMC Technical Design Review in February 2000 to file a formal Engineering Change Request with STAR. The relaxed integration volume would still leave 6.3 cm clearance between the front edge of the EEMC and the TPC and SVT (Silicon Vertex Tracker) electronics, more than adequate for air circulation.

Table 8.1. Depth Budget for the EEMC.

EEMC Component	Thickness Spec. (mm)	Tolerance Allowed (mm)	Total Nominal Depth (mm)	Total Depth Tolerance (mm)
Pb radiator sheets	4.68	± 0.30	107.6	6.9
SS radiator covers	0.90	± 0.08	20.7	1.8
Epoxy in radiators	0.26	± 0.15	6.0	3.5
Std. scint. megatiles	4.00	± 0.20	88.0	4.4
Preshower scint.	5.00	± 0.25	10.0	0.5
Fiber routing guides	1.60	± 0.15	38.4	3.6
Tyvek reflectors	0.25	0	6.0	0.0
Tedlar light shields	0.10	0	2.4	0.0
Bent Al megatile covers	0.40	± 0.15	9.6	3.6
Megatile clearance	0.50	$+1.03^a$	12.0	0.0
4 SMD layers	32.00	± 2.00	32.0	2.0
Al front plate	9.53	+ 0.30 - 0.05	9.5	0.0
SS backplate	31.75	+ 0.64 - 0.13	31.8	0.6
24 SS spacers		± 1.22	0.0	1.2

Total depth including tolerance = 403 mm

^a This specification corresponds to the maximum clearance that will occur for any megatile if all components of that megatile come in at the low end of the allowed tolerances. The 0.50 mm allowed for clearance in each megatile is the *minimum* clearance, if all components come in at the upper end of the allowed tolerance ranges.

The depth increase arises mainly from four modifications in the design from the CDR. The thickness of the EEMC backplate has been increased from 22.2 mm to 31.8 mm to improve the mechanical integrity of the design. The redesign of the SMD to make it modular has increased its nominal depth from 21.0 mm in the CDR to 32.0 mm. This increase is needed to allow for the overlap between adjacent SMD sectors discussed in Sec. 4, which we view as essential to the design, and for sufficient space for optical connectors for the SMD fibers at the $\eta \approx 1$ edge of the detector. Detailed plans for the assembly of calorimeter megatiles, including allowances for worst-case thickness tolerance buildup on the scintillator and fiber routing guides, have increased the estimate for nominal thickness of each megatile assembly by 0.3 mm from the CDR. Finally, the design now includes the substantial additional clearances (totalling 19.9 mm) needed to allow for thickness tolerances on radiator sheets, the aluminum pans binding each megatile section, the SMD layer and the front and back plates. Thus, for example, the stainless spacers that maintain the separation between successive radiators will be machined with sufficient length to allow megatile insertion with 0.5 mm clearance in each layer, even in the case when all components exceed their nominal specified thickness by the maximum allowed amount. If all components were accurately produced at the nominal thickness, the assembly clearance within each layer would be 1.2 mm. The present depth budget, including tolerance allocations for each component, is summarized in Table 8.1.

The η integration limits for the EEMC are also indicated in Fig. 41. As indicated in the CDR, the EEMC active volume will extend all the way to $\eta = 2.00$. The extra 2.5 cm allowed beyond this limit, nominally for “EMC cable routing” in the integration drawing, will in fact be used for the inner detector hub. All optical fibers will be routed to the back of the poletip at the $\eta \approx 1$ edge of the detector. About 2 cm of additional space has been added for the fiber routing, in comparison with the plan presented in the CDR, thereby reducing the EEMC active volume slightly: it will now start at $\eta = 1.078$, rather than $\eta = 1.069$.

The total EEMC weight, including PMT boxes and their contents, is very close to the 30 tons that had been previously announced as the integration limit. However, it is now understood that the true limit is imposed by a shift in the center of gravity of the poletip plus EEMC, which might introduce the danger of the assembly tipping on the lifting fixture during an earthquake. In fact, the calorimeter structure itself will add substantially less than 30 tons on the front of the poletip, and this will be partially counterbalanced by the weight of the PMT boxes on the rear of the poletip. Thus, the present design should fall well within the effective weight limit.

The STAR integration review will also go over EEMC needs for space for electronics and cable routing, but no difficulties in that regard are now foreseen. A new need introduced by the calibration considerations in Sec. 7 is space for the EEMC laser. We had considered the possibility of mounting the laser itself and the primary beam distribution center described in Sec. 7.4 in a remote room in the West Assembly Hall near STAR. However, the cost for outfitting an appropriate room is excessive, and it would also add substantially to the laser system cost by increasing the required high-power UV fiber run lengths by a factor of 3–4. Hence, the present plan is to mount the laser and beam distribution center on one of the electronics platforms attached to STAR, in a sealed box designed for this purpose. The light would then be transmitted to an optical fiber hub on the rear of the poletip via 8 quartz fibers of length not exceeding 10 m apiece. This arrangement limits maintenance on the laser to be performed during periods of access to the Wide Angle Hall, presumably within a temporarily curtained area on the platform. The laser system for the TPC (to be shared by the Forward TPC as well) is already similarly mounted near STAR. The EEMC system will use a different Nd:YAG harmonic (third rather than fourth), and therefore must be separate from the TPC laser.

8.2 Conditions on the Rear of the STAR Poletip

In order to keep optical fiber runs reasonably short, the PMT's and MAPMT's for the calorimeter towers, SMD strips and preshower layers must all be mounted, with their front-end readout electronics, on the rear of the west end poletip of STAR. For similar reasons the beam-splitting system, which routs UV laser light from the 8 quartz fibers to 1560 UV-transparent plastic fibers for the individual megatiles and SMD sectors, must also be mounted on the rear of the poletip. All of these systems must be mounted in a limited space characterized by substantial ambient magnetic fields and heat load. This requires the design and fabrication of custom-made PMT boxes that combine sufficient capacity, magnetic shielding, cooling, space for fiber routing and reasonable accessibility for repairs or replacement of phototubes. A new collaborating institution (Texas A&M University), whose members (R. Tribble, C. Gagliardi) have considerable experience in solving similar technical problems, as well as in nucleon structure physics, has just joined to take on this design and fabrication task. It is thus too early to have a final design of the PMT boxes. However, continuing work performed over the past several months has convinced us that a suitable solution exists. In this section, we discuss the relevant considerations.

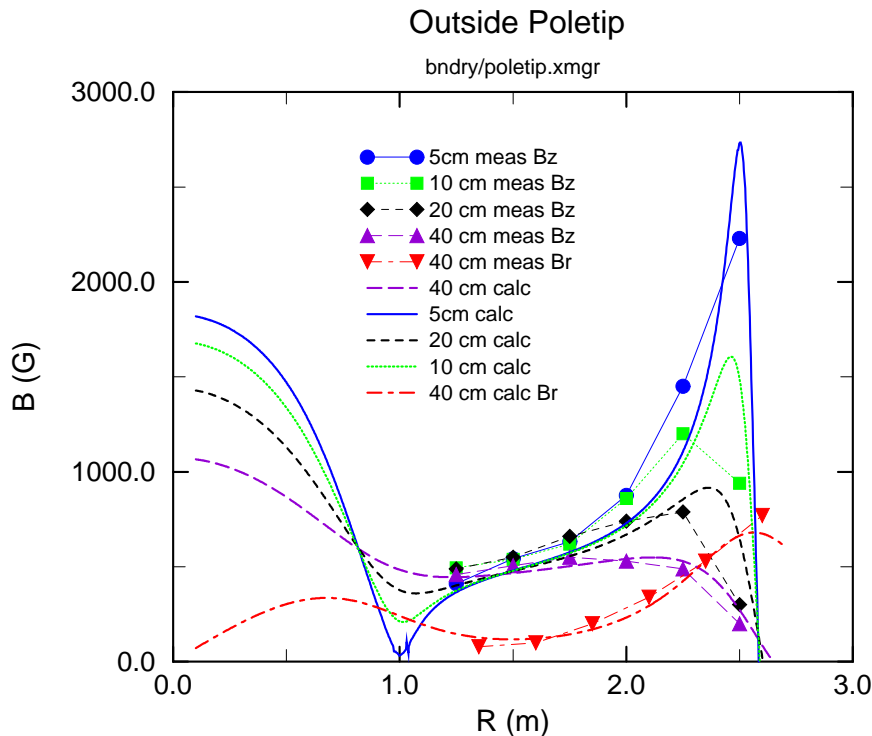


Figure 42: *The magnetic fields in the region where the PMT box will be placed. The calculations are compared to measurements of the field and show reasonable agreement.*

The fields measured near the bottom of the poletip with the STAR magnet at full field are compared in Fig. 42 to calculations performed within a simplified, axially symmetric model of the magnet. This model is sufficient to reproduce the qualitative features of the ambient fields, as needed for PMT box design. It is clear from Fig. 42 that one wants to keep the PMT's as far as possible from the outer radius of the poletip. However, in designs considered so far, adequate

capacity can be attained only if the PMT boxes extend out to radii of 2.1–2.3 m, where the fields can exceed 1 kG.

Two possible designs of steel PMT boxes that would provide adequate shielding are indicated schematically in Fig. 43, superimposed on a layout of the poletip indicating space available to the EEMC. The box layouts drawn on the right-hand half of the figure provide sufficient capacity for all PMT's and MAPMT's foreseen, from all sectors of the EEMC. The layout drawn on the left-hand side, which does not extend to equally large radii, does not provide sufficient capacity near the bottom of the poletip, where additional crowding is introduced by the inaccessible volume associated with the poletip lifting fixture. The larger boxes are envisioned to have 9.5-mm thick outer 1010 steel walls and inner steel walls of thickness either 9.5 mm (for the few nearest the outer radius) or 6.4 mm. Running along the inside of the outer walls is an L-shaped corridor to be used for fiber-routing. The inner wall dividers are steel sheets to which are attached mounts for 12 30-mm diameter PMT's (each to be surrounded by additional mu-metal sheet), to be laid out in two columns of 6 PMT's apiece, aligned parallel to the poletip surface. Each steel sheet would be made to slide into or out of the box, to facilitate PMT maintenance.

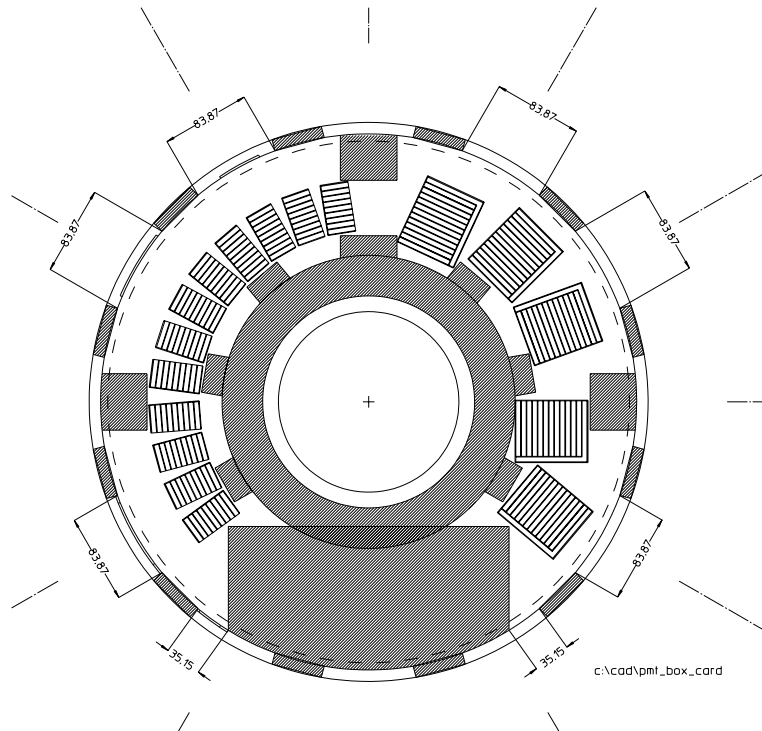


Figure 43: A view of the outside of the magnet poletip. The cross hatched areas are reserved and not available for EEMC use. Two possible designs and positions for PMT boxes are shown.

The magnetic fields calculated within our model for the inside of such a box are shown on two different scales in Fig. 44 and Fig. 45. The scale in the first figure is chosen to show the strong fields within the steel walls, while the second emphasizes the fields (before addition of mu-metal sheet surrounding the tubes) within the gaps left for PMT mounting. The gap fields are ≤ 40 G, from which level they can be further reduced by mu-metal sheet to below the ≈ 1 G limit desired for the ETL 9107 tower PMT's (see Sec. 6.1). The gap at the outermost radius is off-scale in Fig. 45,

but this corresponds to the fiber-routing corridor, where PMT's will not be mounted. The same calculation shows that the addition of such boxes on the poletip will change the central STAR field in the TPC active volume by $< 0.1\%$.

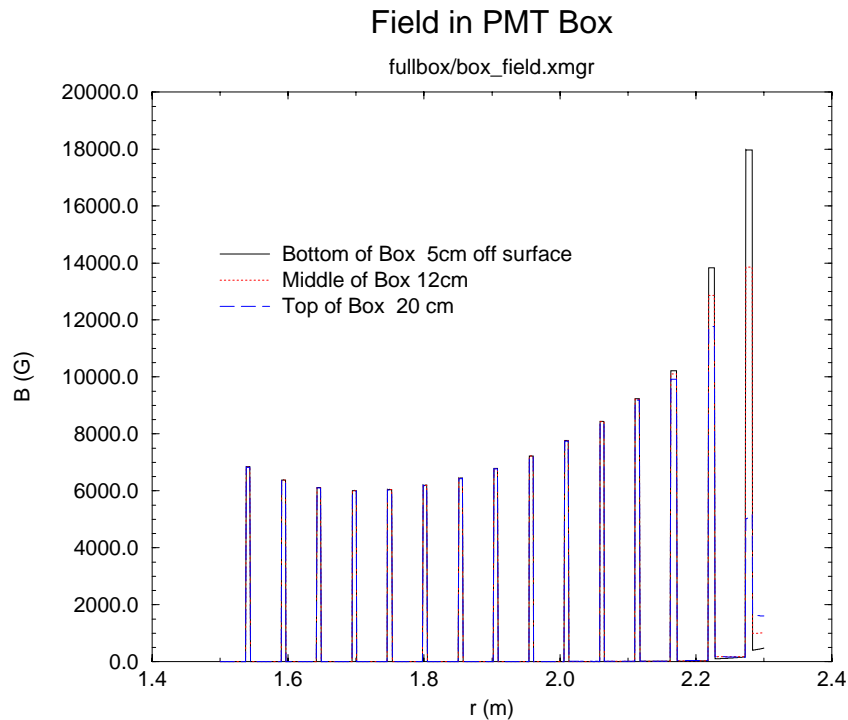


Figure 44: *The magnetic field magnitude in the steel walls of the PMT box vs radius from the magnet center line.*

A detailed design of the PMT boxes, incorporating allowance for adequate cooling, for incoming fiber connectors and outgoing cable connectors, should be completed by Summer 2000. On that time scale, we will also have a sufficiently advanced FEE design to make a reliable estimate of the total heat load and space needs within the PMT boxes. The Review Committee raised an additional question during the Conceptual Design Review concerning the heat load introduced by the trim coil mounted on the inside of the poletip. This does not appear to present a significant problem. The poletip trim coil runs typically at 85°F. The trip setpoints on the return cooling water allow a maximum swing of about 10°F before coil power would be cut off. However, the trim coil is thermally isolated from the poletip, which presently runs close to room temperature when the magnet is powered.

The poletip layout shown in Fig. 43 also can be used to illustrate two further integration issues currently under study. One concerns fiber routing to the lower PMT boxes. The clear fibers carrying light from the towers and SMD layers in the 5, 6, and 7-o'clock sectors of the EEMC must all exit through truncated gaps at $\eta = 1$, to avoid the obstruction caused by the massive poletip lifting fixture. Thus, the entries to these gaps will be especially crowded with fiber ribbons. A mockup of these regions made at IUCF indicates that the fiber-routing is still feasible, but not with a lot of space contingency. The second issue concerns space on the poletip for the fiber-routing hub needed for the laser system. With the present thinking regarding PMT box layouts, there should

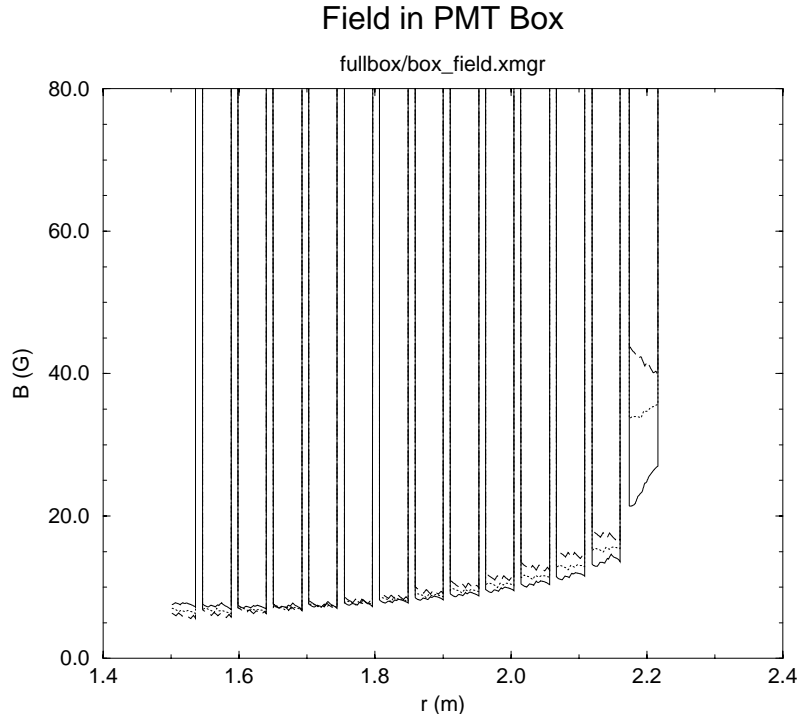


Figure 45: *The magnetic field magnitude in the gaps between the steel walls of the PMT box vs radius from the magnet center line.*

still be adequate space left near 12-o'clock on the poletip, but with the result that UV-transparent plastic fiber runs will have to be considerably longer (leading to greater attenuation) to the lower than to the upper sectors of the EEMC.

8.3 Progress on Level 3 Trigger Hardware and Software

As discussed previously in the CDR [1], high-luminosity p+p collisions at RHIC lead to a sizable probability that a minimum-bias event will occur in each beam crossing; beam crossings occur with a frequency of 9 MHz. The slow drift time of the TPC will result in the recording of track segments from these minimum bias events, arising from ± 400 bunch crossings relative to the trigger event, mixed with the tracks from the high- p_T event of interest. The design of the TPC for central Au-Au collisions enables it to resolve the resulting thousands of tracks in the event. The significant data volume from the TPC for a p+p event, including the pileup, would limit the DAQ throughput to ≈ 1 Hz. In order to increase the rate at which events can be recorded by DAQ by a factor of at least 20, to match the throughput required by the STAR spin physics program, an on-line reduction of the data volume from the TPC is required. The architecture of the STAR DAQ has provisions for performing this data reduction in the so-called Level 3 (L3) trigger. Progress on L3 hardware and software, and on an algorithm to filter the high- p_T event TPC tracks from the pileup of tracks from minimum bias events, are presented in this section.

The L3 system is designed to reduce the STAR trigger rate to DAQ for Au + Au events by about two orders of magnitude. The eventual system foreseen for this task [19] will comprise 24 Level 3

sectors (each corresponding to one 30° sector from one of the TPC end planes), plus one global L3 processor farm to combine data from all sectors and issue L3 decisions. Each sector will contain 4 parallel ALPHA 21264 CPU's to perform fast reconstruction of track segments from the centroids of three-dimensional TPC clusters deduced from the raw TPC pad hits. The cluster finding takes place in Intel i960 CPU's implemented within the STAR DAQ Sector Brokers (Motorola MVME-2306 VME boards, carrying PowerPC 604's, for each TPC sector). Hit information from the barrel and endcap EMC's and from the Silicon Vertex Tracker will be available at the global L3 master CPU's (either Pentium III or ALPHA XP1000). The sector and global processors will be able to communicate among one another (with information flow in any direction), and with the STAR DAQ Sector Brokers, via a MYRINET interface.

In Fall 1999, the STAR L3 subgroup, led by a team from the University of Frankfurt, assembled and tested a large-scale L3 prototype with laser and cosmic particle events. The architecture of the prototype system is indicated in Fig. 46, and the results of the successful tests are reported in [19]. The prototype system included 12 L3 sectors, based on ALPHA DS10 processors. The fast track reconstruction was based on a conformal mapping algorithm developed for STAR [20] by one of the EEMC collaborators. The final phase of the L3 architecture, described above, will raise the limit on L3 input rates from the present ≈ 25 Hz to ≈ 100 Hz. The final phase is envisaged for implementation in 2001, a time scale well matched to its eventual adaptation to the quite different aims of the high-luminosity p+p running. For the p+p mode, we will not rely strongly on L3 to reduce the trigger rate, but rather will use it to reduce the data volume for each event via rejection of TPC pileup track segments. It is incumbent upon the spin physics working group, which overlaps very strongly with the EEMC collaboration, to develop the algorithms that can effect this data volume reduction. Substantial progress on simulations toward this end is described below.

The reconstructed pileup tracks are shifted in the direction along the beams (taken as the Z direction) by an amount equal, on average, to the product of the drift velocity of the TPC and the time difference between the particular bunch crossing and the trigger bunch crossing. The variation of the Z position of the event vertex within a single bunch crossing (given by the Z component of the 'intersection diamond'), will randomly smear these average Z positions by $\approx \pm 10$ cm, which is large compared to the ≈ 7 mm TPC drift distance over the 110 ns interval between adjacent bunch crossings. The resulting distribution of the effective Z vertex of the pileup tracks is continuous. Nonetheless, most of those background tracks do not extrapolate to either barrel or endcap EMC towers associated with the triggered event.

The pileup filter algorithm (PFA) correlates information from the EMC towers (Barrel + Endcap) with TPC tracks reconstructed by existing L3 software to determine the position of the interaction vertex from the high p_T event. Once the vertex is found, only the TPC cluster information (three-dimensional center of gravity and ADC sum) associated with those tracks matched to either the vertex or the EMC towers would be passed to DAQ.

The most critical function of the PFA is to identify the Z position of the vertex (Z^{vert}) associated with the trigger event. To ensure the best determination of Z^{vert} , specific requirements are imposed on the reconstructed tracks. First, those with $|\eta| < 1$ are required to have > 20 cluster points to be used in the vertex determination. No hit requirement is imposed on tracks with $\eta > 1$, because they are naturally shortened by acceptance limitations of the TPC. Secondly, only those tracks that project directly to EMC towers with ADC values above a preset threshold are used to identify Z^{vert} . In the simulations the threshold has been set to 10 ADC channels, corresponding to $\sim 50\%$ (75%) of a MIP signal in the barrel (endcap) EMC (assuming all PMT gains are set to accommodate the same maximum p_T values). For each track matched to an EMC tower, we additionally require the distance of closest approach to the nominal beam line in the xy plane (R_{xy}^{DCA}) to be smaller than

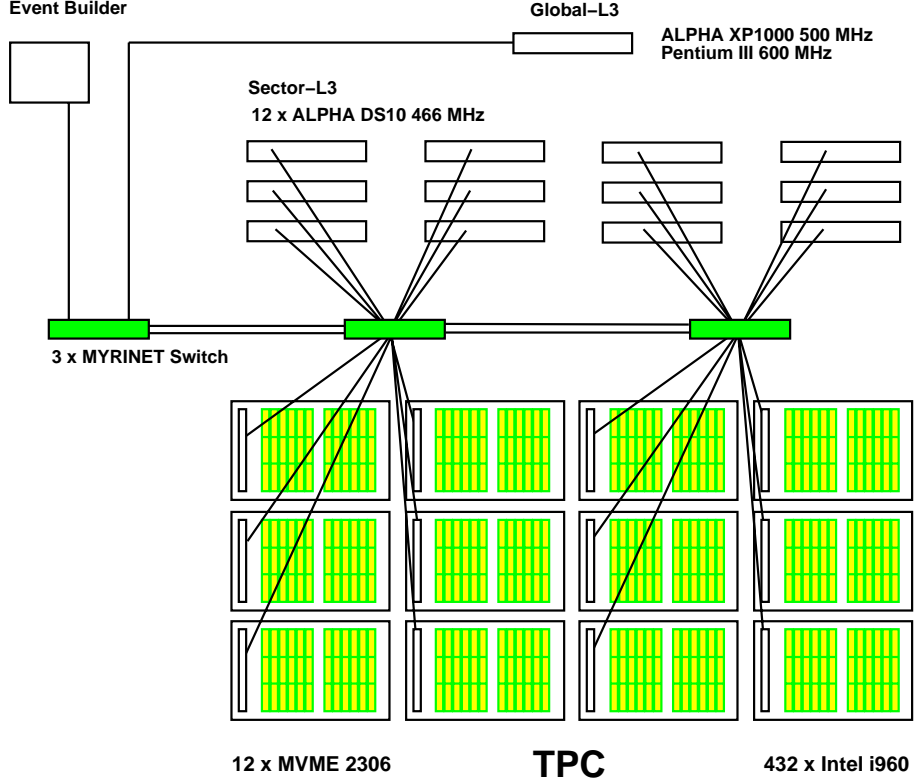


Figure 46: *STAR* Level 3 trigger system architecture used in the prototype test in December 1999. Results of the tests utilizing laser and cosmic ray events are reported in [19].

1.3 cm, in order to reduce accidental matches between background tracks and EMC towers.

The Z^{vert} was found as a maximum of the truncated likelihood function (LF)

$$\ln L(z) = \sum_i \left(Z_i^{DCA} - z \right)^2 / \sigma(\eta_i)^2 \quad . \quad (1)$$

The variation of the weights ($\sigma(\eta)$) used from different tracks in constructing the LF, accounts for the η -dependence of the Z^{DCA} resolution. For the TPC alone it may be approximated as $\sigma(\eta)/cm = 0.3 + 0.5 * \eta^2$. In order to exclude accidental tracks the contribution to the LF from the i -th track was set to be a constant for $|Z_i^{DCA} - z| > 2\sigma(\eta_i)$. A typical distribution of Z_i^{DCA} for a single event and the corresponding LF are shown in Fig. 47.

After Z^{vert} is found, the PFA accepts all reconstructed TPC tracks that either matched EMC towers or approach the nominal beam line at $|Z_i^{DCA} - Z^{vert}| < 4\sigma(\eta_i)$.

This algorithm was tested with a sample of 1000 high p_T (parton-level $\hat{p}_T > 10$ GeV/c) quark-gluon Compton scattering events at $\sqrt{s} = 200$ GeV, generated by PYTHIA. The events are pre-selected such that $\eta_\gamma \in [-1, 2]$ and $\eta_q \in [1, 1.3]$. These events, although well within the STAR detector acceptance, are the most difficult for the reconstruction since a large fraction of the tracks in the TPC from the quark jet are slanted towards the beam line and do not produce full length tracks in the TPC. Consequently, the resulting error in $Z_i^{DCA} - Z^{vert}$ is large. Also, the EEMC has coarser granularity, so the number of accidentals is larger than for the tracks that intercept the

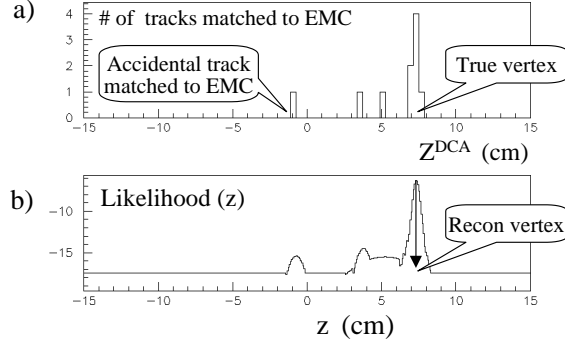


Figure 47: An example of the Z^{DCA} distribution for a single event (a) and resulting shape of the likelihood function (b).

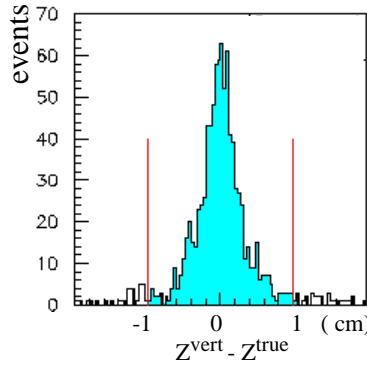


Figure 48: The distribution of errors in vertex position Z^{vert} reconstructed by the pileup filter algorithm for simulated quark-gluon Compton scattering events with $\eta_\gamma \in [-1, 2]$ and $\eta_q \in [1, 1.3]$.

BEMC. The distribution of the interaction point within the beam interaction diamond was approximated by a 3-dimensional Gaussian with $\sigma_x = \sigma_y = 0.5$ mm and $\sigma_z = 7.5$ cm. The trigger event in each case was contaminated with pileup TPC tracks associated with minimum-bias events at the rate (44% probability per beam crossing) expected for full luminosity ($\mathcal{L}_{pp} = 8 \times 10^{31}$ cm $^{-2}$ s $^{-1}$) operation at $\sqrt{s} = 200$ GeV.

For 88% of events in this sample the vertex finder algorithm was able to localize Z^{vert} with precision better than 1 cm, as shown in Fig. 48. On average, about 50 tracks/event were accepted by the PFA out of 2000 reconstructed ones in the fully piled-up event at $\sqrt{s} = 200$ GeV. This suppression is well in excess of that required to achieve the necessary DAQ throughput (the recording of TPC cluster information, in place of raw TPC hits, already effects a data volume reduction by a factor ≈ 5). As discussed below, fine tuning of the PFA must await more realistic TPC simulations. In principle, it may be possible to loosen constraints on either $|Z_i^{DCA} - Z^{vert}|$, or in the definition of track matching at the EMC to preserve more of the event topology, while maintaining the necessary data volume reduction.

With the conditions used in the present simulation, only $\approx 50\%$ of tracks from the original trigger event fulfilled the PFA criteria. The effect of the discarded real tracks on the global event analysis has been studied in several ways, including comparison of the p_T distribution of the reconstructed tracks with and without PFA. It is mainly low-momentum tracks ($p_T < 1$ GeV/c)

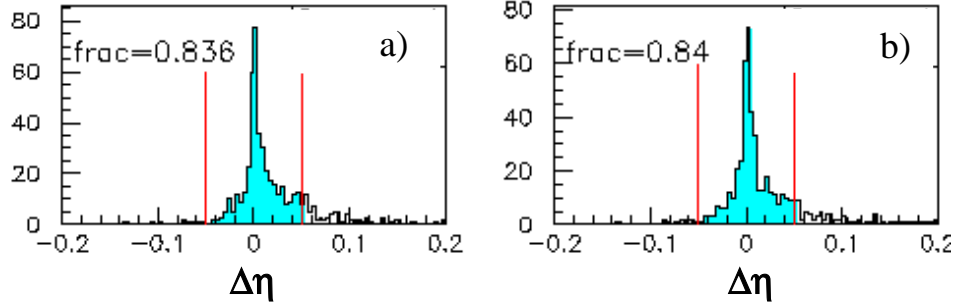


Figure 49: The error of reconstructed quark direction (eq. 2) does not increase if instead of all reconstructed TPC tracks (a) only those accepted by the PFA (b) are used.

that are lost: 94% of the high p_T tracks, crucial for the reconstruction of the jet direction, are preserved. The impact of the losses on the reconstruction of initial-state parton kinematics for γ +jet events then turns out to be minimal, since the hadronization dynamics for the hard-scattered quark already imposes a limitation on how well the recoiling quark direction can be deduced from the measured jet direction. A simulation of the hadronization [21] shows that the error in η_q deduced from a *perfectly* reconstructed jet, defined as $\Delta\eta_q = \eta_q - \eta_{jet}$, has a distribution with $\text{FWHM} \simeq 0.1$. This intrinsic error sets the scale for evaluation of the information losses due to the PFA. (The correlation between quark and jet *momentum* has a much larger intrinsic spread, so the envisioned analysis to extract gluon polarization information makes no use of the jet momentum magnitude.)

Let \vec{P}_g denote the sum of the π^\pm , K^\pm , p and \bar{p} generated momenta within a cone $\sqrt{\Delta\eta^2 + \Delta\phi^2} < 0.7$ around the quark momentum \vec{P}_q , known from the PYTHIA record. Let \vec{P}_r further denote the momentum sum, within the same cone, of only those tracks reconstructed in the TPC (and surviving the PFA when it is used) and matched to the PYTHIA record tracks. Then, the error of the reconstructed η_q , due to the track reconstruction losses, is

$$\Delta\eta_q = \eta(\vec{P}_q) - \eta(\vec{P}_q + \vec{P}_g - \vec{P}_r) \quad (2)$$

The distribution of $\Delta\eta_q$ while using all reconstructed tracks, or only those accepted by the PFA, is shown in Fig. 49. For 84% of the events accepted by the PFA the error $\Delta\eta_q$ is below ± 0.05 . This proves that the low p_T tracks erased by the PFA are of minor importance for the reconstruction of the recoiling quark direction.

The performance of the PFA has so far only been tested with the fast TPC simulator and with the offline reconstruction software, since only those tools were available. It is expected that in reality the TPC resolution will be about twice worse than in this simulation. Also, the L3 cluster finder and tracker will be less precise. Therefore, the maximum in the LF will not be as pronounced as in Fig. 47 (b). Moreover, for full luminosity at $\sqrt{s} = 500$ GeV, there is about a 20% chance to have a second interaction in the same bunch crossing, which may lead to a second maximum in the LF. The total number of pileup tracks will also grow with \sqrt{s} , and the larger number of accidentals may produce false maxima in the LF. Therefore, the following steps to establish the efficiency and overall effectiveness of the PFA are still required:

- (i) Apply the PFA to tracks reconstructed by the existing L3 tracking algorithm, based on space points determined by the L3 cluster finder, from more realistic simulations (the so-called slow simulator) that better predict the performance of the TPC.

- (ii) Modify the $\sigma(\eta)$ dependence by accounting for the number of space points assigned to the track and its p_T . The latter is important because the L3 track reconstruction does not account for the appreciable straggling for low p_T tracks. The pileup tracks are usually shorter in the TPC and of lower p_T than tracks from the trigger event, so these changes will reduce the role of the accidental pileup tracks in the vertex finding.
- (iii) Allow for multiple maxima in the LF and let the PFA preserve tracks in the vicinity of any of them. The offline analysis will have more CPU time available to identify the true vertex.
- (iv) Evaluate the impact of PFA losses on the efficiency of isolation cuts that will be used to reduce background for the direct photon production events. Also evaluate the need for pileup filtering for W^\pm production events, which will generally have fewer tracks available for vertex finding, but which constitute a small fraction of the trigger rate.
- (v) Carefully evaluate the performance of the L3 *vs.* offline cluster finder, in order to decide whether it is sufficient to store on tape only L3 space points, as opposed to the TPC raw hits. The former solution is desirable, since the latter one would require very significant modifications of the present L3 trigger logic.
- (vi) Implement the PFA on the actual processors to be used in L3, to gauge the required processing time. Discussions have already been initiated with the L3 group to converge on the optimal approach for utilizing EMC, and possibly SVT, information within the sector level processors, to minimize the number of pileup tracks that must be reconstructed and passed back and forth between sector and global L3 processors. Identify places where additional CPU's could reduce the PFA processing time. Funds for CPU's specific to the L3 trigger needs of the spin physics program will be sought by BNL from DOE.

8.4 Simulations Regarding the Importance of the Full Barrel EMC

The STAR spin physics program that drives the need for the EEMC also demands complete coverage of the $|\eta| \leq 1$ region by the barrel EMC. The funds so far authorized by DOE (\$8.5 M) for construction of the BEMC were known from the start to be insufficient for completing the full barrel. In fact, present projections indicate it will be enough to complete only slightly less than one half of the barrel. It thus becomes a critical integration issue for the EEMC to make sure that additional funding is received to complete the barrel. A review of the BEMC progress and plans will be held in Spring 2000, and a significant preparatory effort has been devoted by EEMC collaborators to simulations demonstrating the crucial role of the second half of the barrel.

Anything less than a full instrumented BEMC and EEMC would severely impact the quality of the spin physics measurements with the STAR detector. In particular, STAR's capabilities would be drastically reduced in the following regards: (1) acceptance for fully reconstructed jets; (2) ability to extract significant information on the integral gluon contribution (ΔG) to the proton helicity; (3) background suppression for W^\pm production and acceptance for Z^0 production; (4) ability to handle the high p+p luminosities essential to the spin physics program; (5) trigger capabilities for alternative channels providing gluon polarization sensitivity, such as Drell-Yan lepton pair production at high p_T ; (6) efficiency of isolation cuts in distinguishing prompt photons from decays of jet fragments; (7) possibility to compare STAR results to those expected from other experiments for parton polarizations at relatively high x_{quark} or x_{gluon} . Full details on simulations supporting this assessment will be provided in the BEMC proposal update in Spring 2000. Here, we add only a few comments regarding recent work.

As indicated in the preceding subsection, the critical first step in our promising TPC pileup filter algorithm is identification of the correct event vertex location via high- p_T tracks that match up with BEMC or EEMC towers fired during the trigger beam crossing. Elimination of half the BEMC coverage would reduce the number of relevant tracks for a typical event of interest to a dangerously low level, thereby reducing the effectiveness of the pileup filter. The net result, to minimize losses of good tracks, would be a substantial increase in data volume per event, and a consequent reduction in STAR's p+p trigger rate capability. Even then, the events that yield successful triggers will span much less of the interesting range in parton kinematic coverage. This is illustrated for direct photon production in Fig. 50. With only the forward half of the BEMC, one loses the ability to detect the photons originating from gluons with $x_{gluon} > 0.15$ and many of the jet fragments associated with gluons at lower momentum fraction. The former loss removes most of the overlap STAR would have with other experiments (COMPASS, PHENIX) that will study gluon polarization; the latter loss causes a severe deterioration in the quality of information that can be extracted about the integral ΔG . The results in Fig. 50 do not yet take into account the expansion of uncertainties that will arise from the subtraction of abundant background from misidentification of π^0 or η^0 decays as single photons. The reduced usefulness of isolation cuts near the edges of the EMC acceptance would eat further into the range of useful photon data.

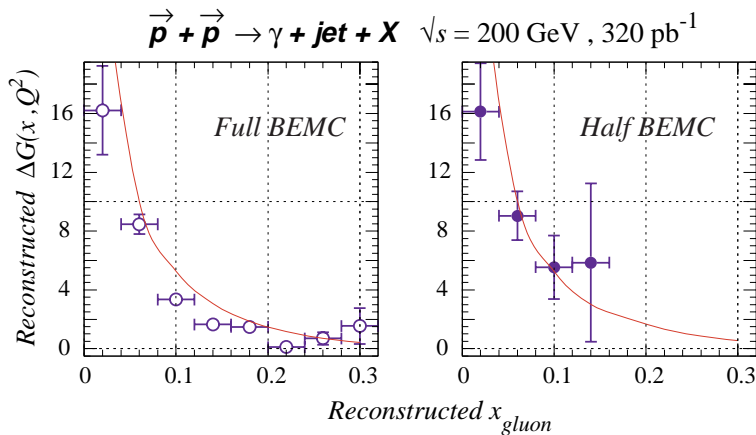


Figure 50: Comparison of $\Delta G(x)$ results directly reconstructed from simulated spin correlation data for the $\vec{p} + \vec{p} \rightarrow \gamma + \text{jet} + X$ reaction at $\sqrt{s} = 200$ GeV. The quality of the results is compared for a full barrel electromagnetic calorimeter (BEMC), spanning $-1 < \eta < +1$ and a half BEMC, spanning $0 < \eta < +1$. In both options, the detector spans the full azimuth and is complemented by the full STAR endcap EMC. The solid curve in each case represents the model input $\Delta G(x)$ (set A from [3]) used in the simulations. The small systematic deviations of the reconstructed from the input values arise from simplifying assumptions made in the analysis, as discussed in [1].

The net result of the above effects for direct photon production is that it would take much longer to acquire data of much poorer statistical and systematic quality, spanning a much smaller range in x_{gluon} . Similarly disastrous effects would occur for measurements to extract antiquark polarization information from W^\pm production or (for purposes of calibration against deep inelastic scattering results) valence quark polarization information from mid-rapidity high- p_T dijet production.

9 Funding, Management and Schedule

9.1 EEMC Funding

Funding for the endcap calorimeter project is now provided by NSF, DOE and Indiana University. An NSF Major Research Instrumentation (MRI) grant for \$1.847 M was awarded to the IUCF group in late Summer 2000. A decision by the Physics Division at NSF to provide additional funding for the construction project in FY 2000-2002 was strongly coupled to the success with the MRI grant. The Physics Division has agreed to put in a total of \$2.350 M spread over the three-year period, beginning with a relatively small amount (\$250 K) in FY2000, when they still have heavy commitments to other ongoing Nuclear Physics construction projects. Indiana University is providing matching funds in the amount of \$865 K, also over the three-year period, for the MRI grant. In addition, the University has agreed to put in half the difference, or \$77 K more, between the MRI amounts requested *vs.* awarded (the other half being subsumed in the total quoted above for the NSF Physics Division). An additional \$1.018 M will be funded over three years from the IUCF operating grant (also provided by NSF). This amount goes toward equipment and technical and professional staff labor for the construction, and is over and above a comparable (off-budget) IUCF contribution to physicist salaries and travel. The DOE has very recently agreed to provide substantial incremental funding (\$200 K/year, with a matching amount of \$100 K/year from the High Energy Physics Division at ANL) to Hal Spinka's group over the duration of the EEMC construction, to support two post-doctoral associates, 0.6 FTE of technician time and 40% of Dave Underwood's time for work on the SMD assembly and testing. The DOE has also approved a redirection of personnel support funds for the Texas A&M group from a now indefinitely postponed experiment to the EEMC. Additional funding requests from BNL to DOE and from Kent State University to NSF for contributions to the EEMC project are currently pending.

The funding profile established for the NSF and Indiana University contributions is shown in Fig. 51. Although the MRI funds are officially FY 1999 funds, only the first \$250 K was authorized for use in FY 1999, and that amount was awarded at the very end of the fiscal year. Release of the remainder of the MRI funds for spending in FY 2000 is pending the outcome of the Technical Design Review of the EEMC in February 2000. The Indiana University support shown in Fig. 51 for FY 1999 came from two accounts awarded previously, over and above the promised MRI cost-sharing funds discussed above. These Indiana University funds, as well as substantial personnel support (not indicated in the figure) from IUCF, were essential in producing the prototype detector and preparing for the test beam described in Sec. 3 of this report. The initial increment of MRI funding has already been partially spent to order a high-speed routing machine that will be used for megatile machining at IUCF, for setup of the associated megatile production facility, and for equipment purchases needed for ongoing prototyping. The portion of Indiana University matching funds already released (proportional to the MRI funds so far authorized for spending) have been used to support essential engineering consulting help in the initial preparation of engineering drawings and in verifying the FEA calculations regarding the structural integrity of the EEMC.

If the expected contributions from the BNL and Kent State collaborators are approved, we will then have a funding plan that fully supports the budget presented later in this section. The funding profile does not allow completion of both halves of the EEMC by Summer 2002, as had been optimistically projected in the Conceptual Design Report. It will still allow installation of one half of the EEMC during that summer shutdown if spending authorization for the remainder of the MRI funds is released in Spring 2000. As will be shown in the timeline presented in Sec. 9.4, many large purchases have to be initiated in Spring and Summer of 2000 to meet this aggressive

EEMC Funding Profile

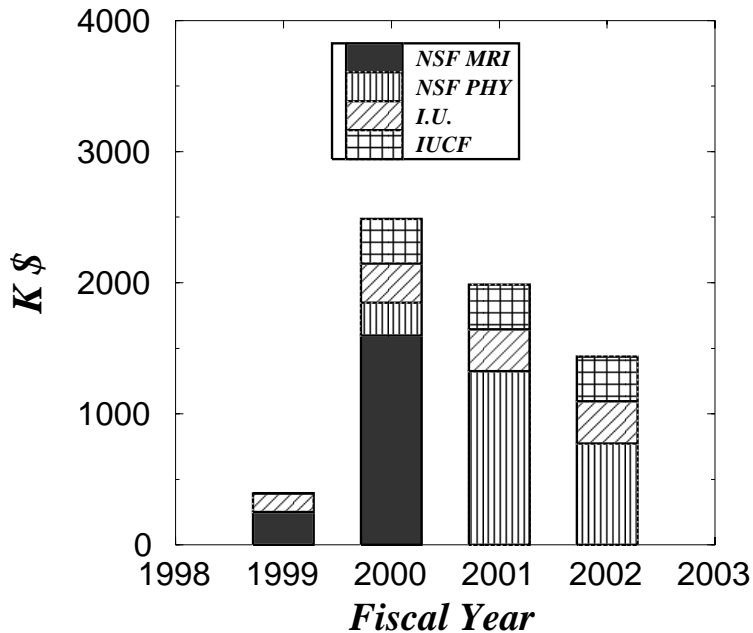


Figure 51: *Anticipated profile of funding for the EEMC project from NSF and Indiana University sources. The MRI grant was received at the tail end of FY 1999. The Indiana University contribution shown for FY 1999 is from accounts over and above the MRI cost-sharing funds. The integral of the funds shown here is \$6.30 M.*

goal.

9.2 Additions to the EEMC Collaboration

We continue to work on attracting new collaborators, from both within and outside the existing STAR collaboration, to work on the EEMC project. A new group from Texas A&M University is set to join, pending only approval by the STAR Council. This group, comprising Bob Tribble and Carl Gagliardi, with post-docs and graduate students, brings considerable relevant experience and intellectual leadership. They have been very active participants in the NUSEA collaboration at FNAL, which has used dilepton production to probe the flavor imbalance in the nucleon sea, J/Ψ production mechanisms and other issues. They have engineered and built boxes to house phototubes in a high magnetic field environment for the MEGA collaboration that searched for the lepton-family-violating decay $\mu \rightarrow e\gamma$. They have agreed to take on a similar technical role in the EEMC construction, and have expressed strong interests in leading physics programs associated with p+A collisions (probing the gluon distribution in nuclei) and with Drell-Yan processes in STAR. Their laboratory includes a DOE-supported cyclotron facility, and brings substantial additional research infrastructure to the project. DOE has approved their move in this direction.

A second group, from Rutgers University (Charlie Glashauser, Ron Ransome and Ron Gilman), has also expressed strong interest in the STAR spin program. Due to their existing heavy com-

mitments at Jefferson Lab, they feel hiring a new faculty member is critical to their being able to contribute strongly to the STAR efforts. They have initiated discussions within the Physics Department at Rutgers, and already invited two potential candidates to probe the possibilities. This group has extensive expertise in intermediate-energy spin physics. Given the time scale on which they are likely to make a firm decision, they are most likely to contribute strongly to physics analysis and to STAR software needs associated with the EEMC.

The Argonne National Laboratory group, comprising Hal Spinka, Dave Underwood, plus technicians, postdoctoral associates and undergraduate students, required additional funding from DOE to remain involved with the EEMC project. That funding increase has now been approved, and we are counting on the ANL group to take on the major responsibility for SMD assembly and testing.

Other collaborating institutions within STAR are either in the process, or initiating discussions, to hire new faculty or staff members with experience and interest in the spin physics program. These include Indiana University, Lawrence Berkeley Laboratory, the University of Texas and Brookhaven National Laboratory. Such hires will help to ensure a vibrant program of spin physics with STAR, but are not being counted upon in our present planning to make major contributions to the EEMC construction.

The present collaborator list for the EEMC is as follows:

ANL: D. Hill, T. Kasprzyk, H. Spinka, D. Underwood, A. Yokosawa

BNL: W. Christie, T. Hallman, K. Turner

Dubna LHEP: G. Averichev, R. Badalian, S. Chernenko, V. Dunin, L. Efimov, Y. Panebratsev, E. Potrebenikova, D. Razin, S. Razin, O. Rogachevskiy, M. Tokarev, V. Yurevich, A. Zubarev

IUCF: C. Allgower, J. Balewski, L.C. Bland, W. Hunt, W.W. Jacobs, A. Klyachko, K. Komisarck, W. Lozowski, J. Puskar-Pasewicz, T. Rinckel, K. Solberg, J. Sowinski, E.J. Stephenson, S.E. Vigdor, S.W. Wissink

Kent State U: B. Anderson, D. Keane, J. Watson, W. Zhang

Michigan State U: A.M. Vander Molen, G. Westfall

Penn State U: S. Heppelmann, A. Ogawa

Rice U: B.E. Bonner, G. Eppley, E. Platner, P. Yepes

Texas A&M U: C. Gagliardi, R.E. Tribble

UCLA: V. Ghazikhanian, H. Huang, G.J. Igo, S. Trentalange, O. Tsai, C.A. Whitten, Jr.

U. Texas: G.W. Hoffmann, C.F. Moore, R.L. Ray, J.J. Schambach, H.J. Ward

Wayne State U: T. Cormier, C. Pruneau, V. Rykov

In addition to the above groups, we expect considerable support from the STAR Operations Group with respect to integration issues, and from groups at LBL, BNL and Creighton University that are currently working on barrel EMC electronics projects that will be carried over for the EEMC.

9.3 Management Plan

The project management structure for the EEMC construction is shown in Fig. 52. Will Jacobs is the Project Manager. With the exception of the important SMD assembly and testing that will be carried out at Argonne, coordination of the other aspects of the project remains at IUCF, where the production of megatiles and final assembly and testing of the EEMC are envisioned to occur. The grouping of responsibilities in the management chart has been tailored, to some extent, to the talents, interests and available time of the physicists and engineers leading the efforts. Thus, the subprojects to be supervised by teaching faculty (Bland, Vigdor, Wissink) are more limited than those overseen by full-time research faculty (Jacobs, Sowinski, Spinka) or engineers (Hunt).

The responsibilities listed in Fig. 52 for groups from LBL, MSU and UCLA, and also some of the IUCF electronics projects, are very similar to tasks these groups are already carrying out for the barrel EMC project. The large Dubna group is being assigned a number of responsibilities, some to be carried out at Dubna and some in the U.S. at other institutions. Thus, much of the Dubna work on SMD readout electronics will be carried out at IUCF, and their contributions to SMD sector assembly and testing will be carried out at ANL. The labor-intensive QA/QC procedures for optical fibers (MSU), tower PMT's (Rice), and SMD and preshower MAPMT's (Kent State) are assigned to groups not directly involved in the also labor-intensive production of megatiles and SMD modules. Les Bland leads the extensive efforts on simulations, but strong short-term contributions are expected as well from the other individuals and groups listed in that box.

9.4 Timeline

A detailed timeline and schedule of critical tasks and projected milestones for the endcap EMC project is presented in Fig. 53. At the time of this technical review, indicated by the dashed vertical line near mid-February '00, several milestones have been achieved and significant progress made toward initiation of the construction phase of the project.

The decision to aim for installation of only one half of the Endcap EMC in the summer '02 RHIC shutdown, still leads to a fairly tight schedule. Following release of additional funds, there will be a significant start up effort to get long lead time orders placed and the production of detector components going in a timely fashion. The goal of having the first half of the detector in test mode with cosmic rays at IUCF near the beginning of calendar year '02, seems imperative in order to allow enough time for retrofitting and problem solving before shipment to BNL and installation in that summer.

9.5 Budget

Since the time of the CDR in May '99, many aspects of the EEMC design have been solidified, allowing more realistic budget estimates to be made. The sought after funding sources and their expected profiles have been established and additional funding contributions have been identified.

In reviewing the budget items we have identified savings in the cost of some major items (e.g., PMT's, detector structure) which are balanced by suggested additional items to the detector budget (e.g., laser calibration system) and the desire to supply more engineering effort and allow for tooling expenses. Over all there is a slight upward pressure on the CDR budget numbers, but not at the level of the 30% contingency suggested by the panel. Details will be presented and discussed at the review.

EEMC Project Management Structure (1/2000)

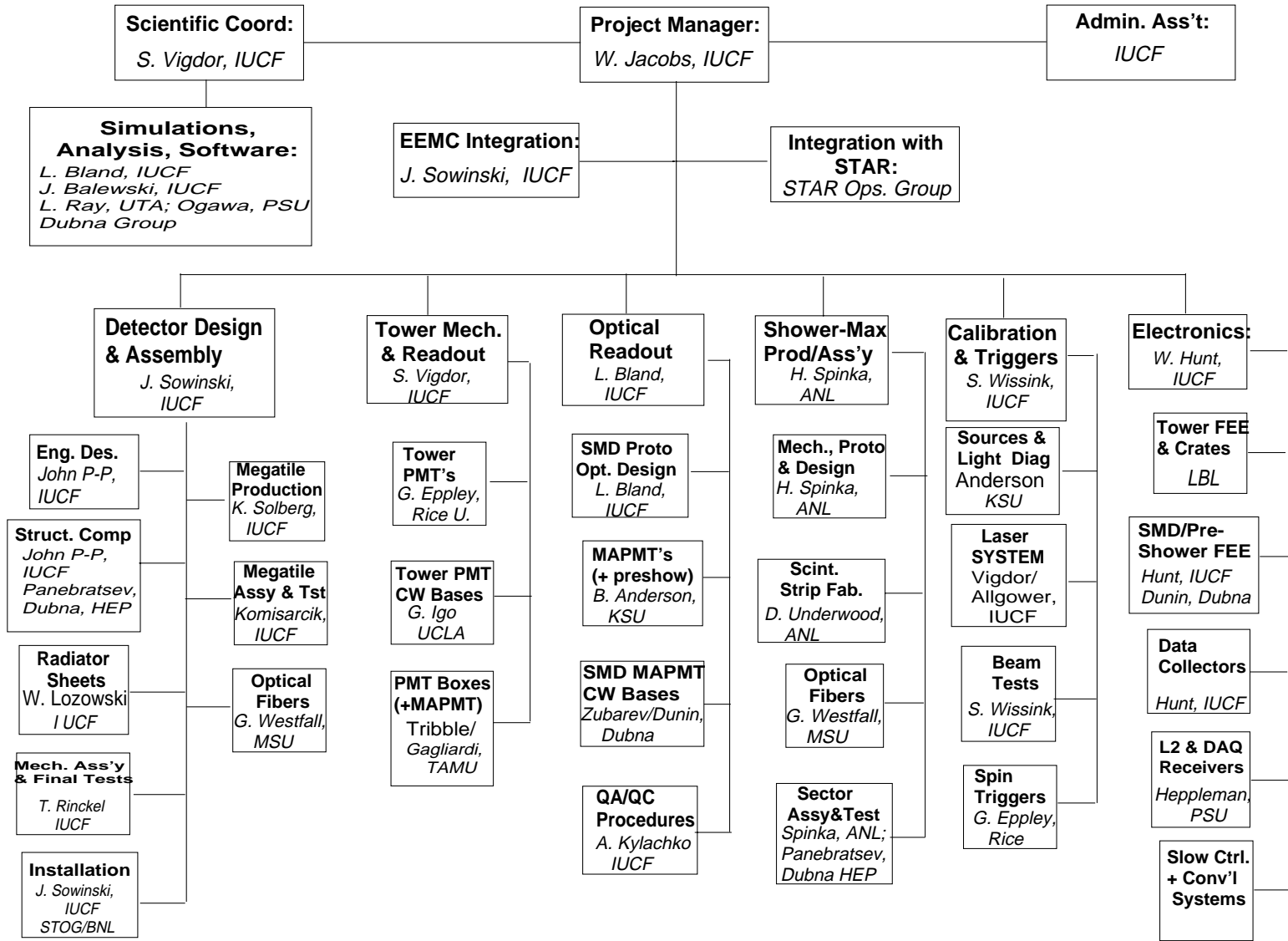
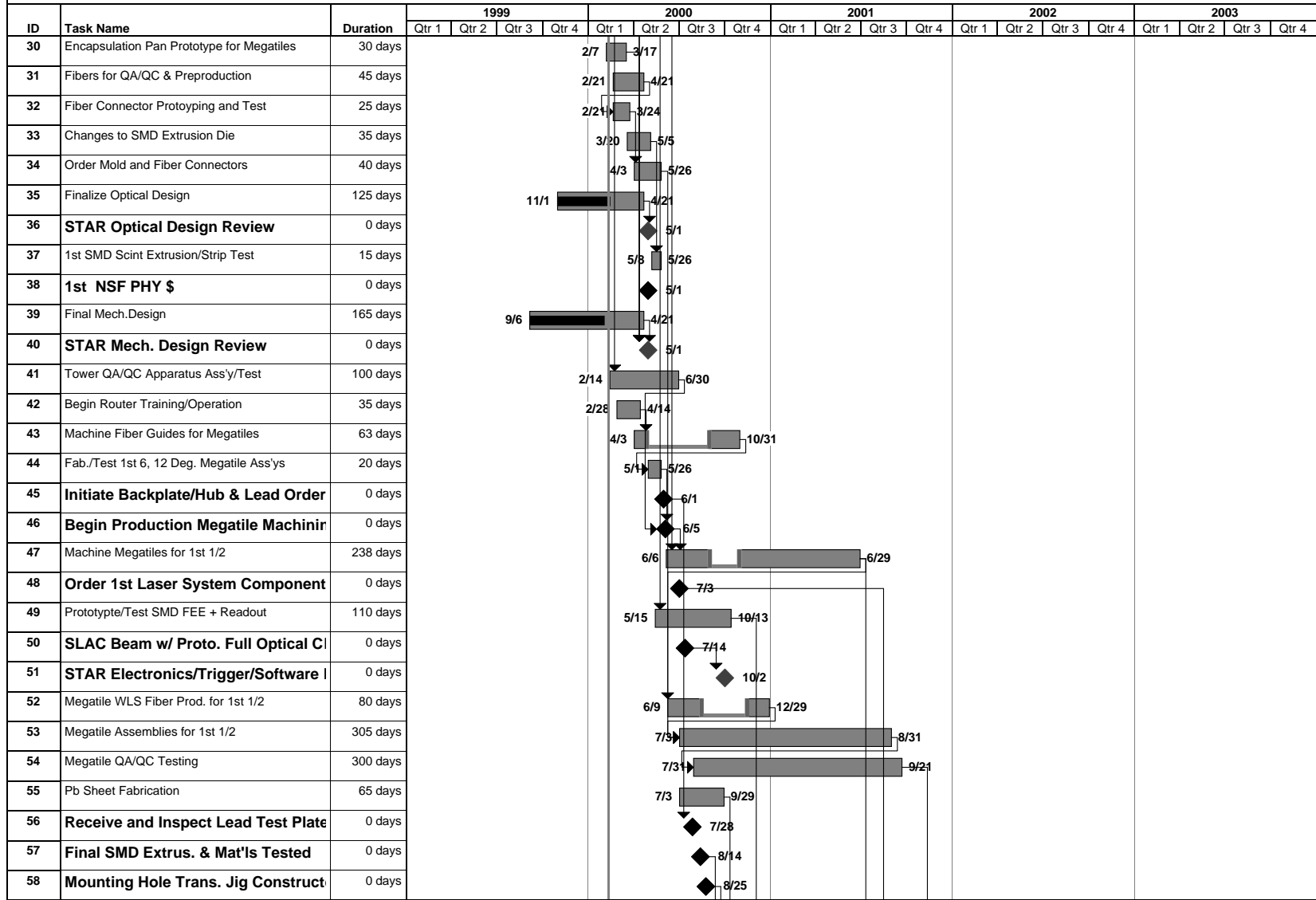


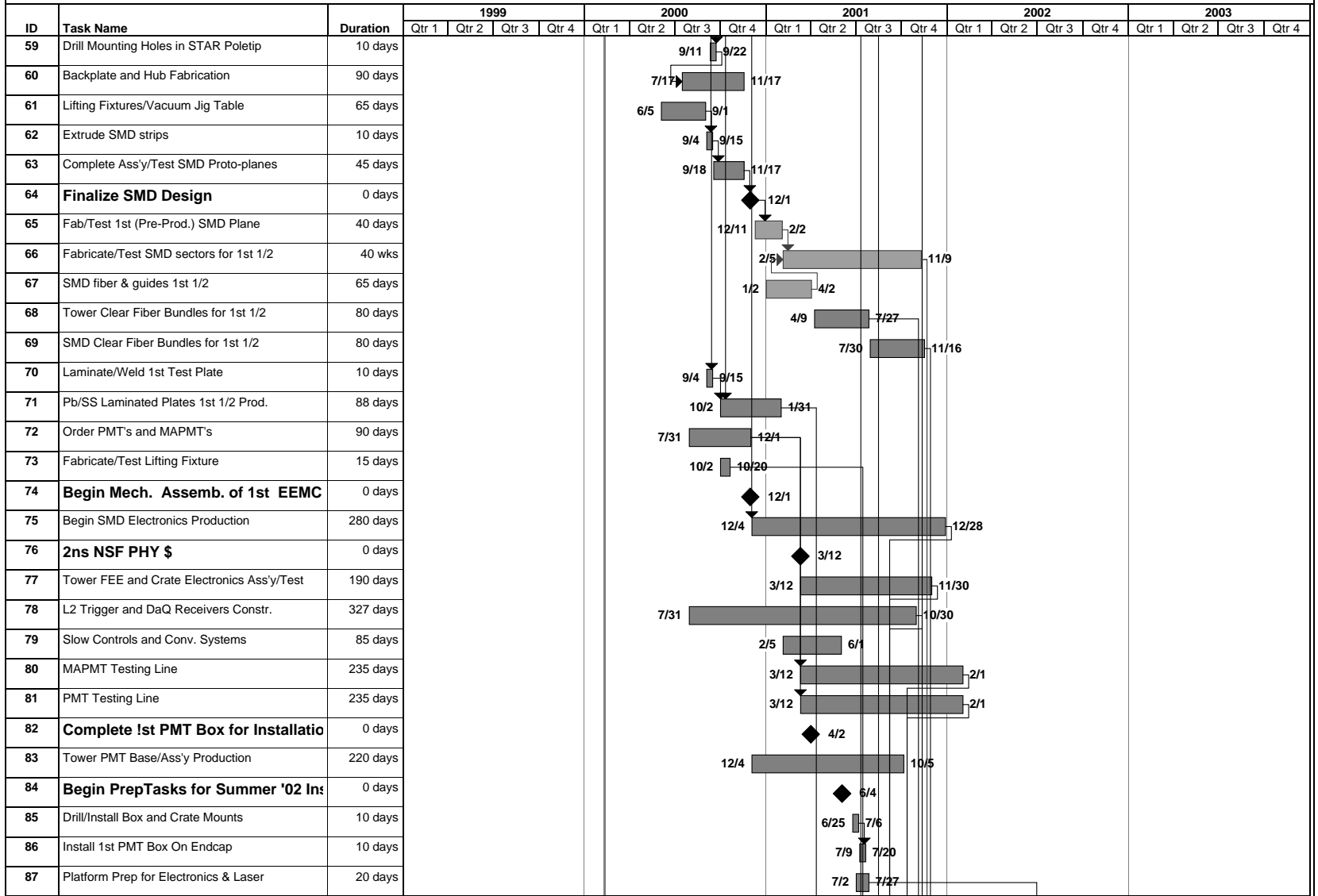
Figure 52: Management structure of the EEMC project.

EEMC Construction Milestones and Critical Path Tasks



87

EEMC Construction Milestones and Critical Path Tasks



88

EEMC Construction Milestones and Critical Path Tasks

ID	Task Name	Duration	1999				2000				2001				2002				2003							
			Qtr 1	Qtr 2	Qtr 3	Qtr 4	Qtr 1	Qtr 2	Qtr 3	Qtr 4	Qtr 1	Qtr 2	Qtr 3	Qtr 4	Qtr 1	Qtr 2	Qtr 3	Qtr 4	Qtr 1	Qtr 2	Qtr 3	Qtr 4				
88	1st Round Install Conventional Systems	20 days									7/30	8/24														
89	Laser Assembly Completed	0 days										9/3														
90	Assemble 1st 1/2 Mech. Struct.	66 days									4/13	7/13														
91	Lifting/Structure Tests	10 days									7/16	7/27														
92	Install SMD and Megatile Scints	25 days										11/12	12/14													
93	Integrate/Test Electronics 1st 1/2	90 days									10/4		2/1													
94	Prepare/Fiber PMT & MAPMT Boxes	84 days									11/5		2/28													
95	Calibration Run at SLAC	5 days									11/12	11/16														
96	Detail Installation Procedures	90 days									10/15		2/15													
97	Ass'y/Test Cosmic Ray Test Stand for 1/2	86 days									9/3		12/31													
98	Complete 1st EEMC 1/2	0 days											12/14													
99	Test 1st EEMC 1/2	67 days									1/1		4/3													
100	Fab/Test Installation Fixtures	50 days									12/3		2/8													
101	Installation Review	0 days											2/15													
102	3rd NSF PHY \$	0 days											3/18													
103	Ship 1st 1/2 to BNL	6 days											4/22	4/29												
104	Receive/Unpack in STAR AB	5 days											4/30	5/6												
105	Install Megatiles/SMD and Test	25 days											5/7	6/10												
106	RHIC Shutdown Begins	1 day											6/3	6/3												
107	1/2 EEMC in WAH Prior to STAR Rol	0 days											6/12													
108	Mount Lower 1/2 on Poletip	5 days											6/17	6/21												
109	Laser Installation on STAR N. Platform	20 days											7/1	7/26												
110	Electronics/Trigger Install on Platform	25 days											6/17	7/19												
111	Slow Controls Install/Test	25 days											6/17	7/19												
112	Install PMT/MAPMT Boxes for 1/2	20 days											6/24	7/19												
113	Fiber Routing Detector/Boxes	40 days											6/24	8/16												
114	Crate Mounting and Hookup on Poletip	15 days											7/8	7/26												
115	Trigger/Online Additions Install/Test	20 days											8/5	8/30												
116	Roll In/Hook up to Platform	2 days											8/19	8/20												

68

EEMC Construction Milestones and Critical Path Tasks

06

ID	Task Name	Duration	1999				2000				2001				2002				2003			
			Qtr 1	Qtr 2	Qtr 3	Qtr 4	Qtr 1	Qtr 2	Qtr 3	Qtr 4	Qtr 1	Qtr 2	Qtr 3	Qtr 4	Qtr 1	Qtr 2	Qtr 3	Qtr 4	Qtr 1	Qtr 2	Qtr 3	Qtr 4
117	Source/LED/Cosmic Ray Testing	35 days																				
118	Tests w/ Platform Electr/Contr. to DAQ	38 days																				
119	1/2 EEMC Installation Complete	0 days																				
120	RHIC Shutdown Ends	1 day																				
121	Comissioning of 1st 1/2 EEMC	45 days																				
122	Machine Megatiles for 2nd 1/2	258 days																				
123	Machine Fiber Guides for Megatiles	53 days																				
124	Megatile WLS Fiber Prod. for 2nd 1/2	80 days																				
125	Megatile Assemblies for 2nd 1/2	305 days																				
126	Megatile QA/QC Testing	305 days																				
127	Pb/SS Laminated Plates 2nd 1/2 Prod.	85 days																				
128	Begin Mech. Ass'y of 2nd EEMC 1/2	0 days																				
129	Assemble 2nd 1/2 Mech Struct	43 days																				
130	Fabricate 2nd 1/2 SMD sectors	44 wks																				
131	SMD fiber & guides 2nd 1/2	65 days																				
132	Install SMD and Megatile Scints	25 days																				
133	Complete 2nd EEMC 1/2	0 days																				
134	test 2nd 1/2	67 days																				
135	Ship 2nd 1/2 to BNL	6 days																				
136	Receive/Unpack in STAR AB	5 days																				
137	Install Megatiles/SMD and Test	25 days																				
138	RHIC Shutdown Begins	1 day																				
139	1/2 EEMC in WAH Prior to STAR Rol	0 days																				
140	Mount Upper 1/2 on Poletip	5 days																				
141	Electronics/Trigger Install on Platform	25 days																				
142	Slow Controls Install/Test	25 days																				
143	Install PMT/MAPMT Boxes for 2nd 1/2	20 days																				
144	Fiber Routing Detector/Boxes	40 days																				
145	Crate Mounting and Hookup on Poletip	35 days																				

EEMC Construction Milestones and Critical Path Tasks

ID	Task Name	Duration	1999				2000				2001				2002				2003				
			Qtr 1	Qtr 2	Qtr 3	Qtr 4	Qtr 1	Qtr 2	Qtr 3	Qtr 4	Qtr 1	Qtr 2	Qtr 3	Qtr 4	Qtr 1	Qtr 2	Qtr 3	Qtr 4	Qtr 1	Qtr 2	Qtr 3	Qtr 4	
146	Trigger/Online/Controls Updates	20 days																					8/4 8/29
147	Roll In/Hook Up to Platform	2 days																					8/18 8/19
148	Source/LED/Cosmic Ray Testing	35 days																					7/7 8/22
149	Tests w/ Platform Electr/Connect to DAQ	34 days																					6/30 9/1
150	2nd 1/2 EEMC Installation Complete	0 days																					◆ 8/22
151	RHIC Shutdown Ends	1 day																					9/1 9/1
152	Comissioning of 2nd 1/2 EEMC	22 days																					9/1 9/30

10 References

References

- [1] L.C. Bland, W.W. Jacobs, J. Sowinski, E.J. Stephenson, S.E. Vigdor and S.W. Wissink, *An Endcap Electromagnetic Calorimeter for STAR: Conceptual Design Report*, STAR Note 401 (1999).
- [2] R.D. Ball, S. Forte and G. Ridolphi, *Phys. Lett.* **B378**, 255 (1996).
- [3] T. Gehrman and W.J. Stirling, *Phys. Rev.* **D53**, 6100 (1996.)
- [4] M. Hirai, S. Kumano and M. Miyama, *Comp. Phys. Commun.* **108**, 38 (1998).
- [5] L.C. Bland, in EPIC99 Proceedings, eds. L.C. Bland, T. Londergan and A. Szczepaniak (World Scientific, Singapore, 2000).
- [6] A. Bravar, D. von Harrach and A. Kotzinian, *Phys. Lett.* **B421**, 349 (1998).
- [7] L.E. Gordon and W. Vogelsang, *Phys. Rev.* **D48**, 3136 (1993).
- [8] T. Sjöstrand, *Comp. Phys. Commun.* **82**, 74 (1994).
- [9] F. Abe *et al.*, *Phys. Rev. D* **57**, 67 (1998).
- [10] J. Alitti *et al.*, *Phys. Lett.* **B299**, 174 (1993).
- [11] C. Bourrely and J. Soffer, *Phys. Lett.* **B314**, 132 (1993).
- [12] G. Altarelli, R.K. Ellis and G. Martinelli, *Phys. Lett.* **B151**, 457 (1985).
- [13] B. Abbott *et al.*, *Phys. Rev. D* **58**, 092003 (1998).
- [14] A. Ogawa, in the Proceedings of the RHIC Spin Workshop, Brookhaven, October, 1999 (to be published).
- [15] M. Adams *et al.*, *Nucl. Instrum. Meth.* **A378**, 131 (1996).
- [16] Y. Bonuskin *et al.*, *Nucl. Instrum. Meth. A* **381**, 349 (1996).
- [17] D. Blömker *et al.*, *Nucl. Instrum. Meth.* **A311**, 505 (1992).
- [18] M. Adams *et al.*, *Nucl. Instrum. Meth.* **A366**, 263 (1995) and *Nucl. Instrum. Meth.* **A378**, 131 (1996); D. Lincoln, private communication (1999).
- [19] J.S. Lange *et al.*, to be published in *IEEE Trans. Nucl. Sci.* (2000).
- [20] P. Yepes, *Nucl. Instrum. Meth.* **A380**, 582 (1996).
- [21] *Proposal to Construct an Endcap Electromagnetic Calorimeter for Spin Physics at STAR*, available at public ftp site ftp://ftp.iucf.indiana.edu/pub/iustar/eemc_proposal.ps.gz, and at url http://www.iucf.indiana.edu/Experiments/STAR/BNL_proposal.html.
- [22] *Technical Design Report for the Barrel EMC in STAR* (1998), available at web site http://rsgi01.rhic.bnl.gov/star/starlib/doc/www/html/emc_1/emc.html.

A Responses to the Conceptual Design Review

Much of the work carried out in the past nine months has been stimulated by issues raised in the May 1999 review of the Conceptual Design. We summarize briefly below the actions taken to address the excerpted quotes from the committee report, and indicate where in the earlier sections of this document more relevant detail can be found.

“A detailed critical path has not yet been established, and potential interruptions in the production flow which might arise due to, for example, the FNAL sputtering facility not being available exactly when needed, have not yet been folded into the planning. ... The spokesman and project manager should establish a number of clear milestones that include the testing and analysis of prototype modules, a battery of simulation studies, the rate of progress on the long-term production tasks, and so on.”

A critical path, allowing some leeway for procurement delays, has been prepared, and is presented in Sec. 9. With the now established funding profile, completion of both halves of the EEMC for installation in Summer 2002 is no longer feasible. The reduced goal of installing the first half in 2002 and the second in 2003 appears achievable, but the goal remains “aggressive.” This somewhat stretched timeline goal was agreed to by the NSF when funds were awarded.

“In order to better assess the budget and schedule, it is strongly recommended that the Project Manager immediately begin working with modern management software tools.”

The Project Manager and modern management software tools are gradually coming to terms with one another. IUCF has short-term plans to hire a Project Planner, who will be able to help with much of the bookkeeping for the EEMC project.

“...the management plan will have to be completed on a timely basis...the leadership positions...[should be] rapidly filled with names of real persons who can devote their time to these specific issues.”

A revised division of responsibilities among collaborators is presented in Sec. 9. It identifies the people that will have to assume responsibility for the various major tasks, at least at the start of the project, given the present status of the collaboration. Other details of the management plan, such as procedures for changing designs or releasing contingency funds, and schedules of collaboration meetings, will be worked out in the near future.

“The committee identified a number of technical issues during the presentations that are considerably less well thought out compared to the major core items. These include the calibration system, slow controls, the magnetic shielding boxes with cooling, and potential engineering underestimates. With this in mind, and based on experience with other similar scale projects, the Committee believes it would be wise to plan for a contingency of 30%. This would bring the project total to about \$7.1 M.”

The revised budget presented in Sec. 9 is now based on a firmer plan for calibration systems and includes allowance for increased engineering manpower. Detailed design of the magnetic shielding boxes and slow controls are just beginning, so these items retain higher than normal contingency in the budget planning. Other reallocations within the budget have occurred naturally as the planning becomes more detailed. The revised budget estimates total cost for the EEMC as \$6.9 M. Further funding for the project through collaborating institutions is discussed in Sec. 9.

“If funding fails to meet the \$7.1 M level, a descoped detector can follow several paths that individually produce only modest savings. ... However, these descoped paths are not desirable and should be avoided if possible.”

To date, we have avoided all of the descoping paths discussed at the Conceptual Design Review. In particular, the updated design presented in Secs. 4–6 of this report still includes the originally planned η segmentation into 12 towers per ϕ sector (yielding a total of 720 calorimeter towers), 24 layers in depth within each tower, and full preshower readout.

“Committee concerns voiced focused on what seems to be an underestimation of engineering, a very necessary ingredient in order to complete the Final Design and begin to procure parts.”

The revised budget presented in Sec. 9 includes allowance for additional engineering. In the short term, we have made use of engineering help available on a consultant basis, to help with the large and pressing task of translating construction ideas into mechanical drawings.

“Increased effort on simulation studies (e.g., physics sensitivity, optimization of the SMD strip placement, calibration system, magnetic field shielding, etc.) would greatly accelerate the pace toward Final Design and construction.”

About 2 FTE’s worth of effort have been devoted to simulation studies on a wide range of topics, as reported in Secs. 2, 3, 7 and 8 of this document. These studies span most of the specific questions raised by the Review Committee, plus additional critical work related to Level 3 TPC pileup rejection and the importance of completion of the full barrel EMC.

“It is important that the collaboration broadens to include capable groups that bring intellectual leadership as well as technical help.”

Broadening of the collaboration is work in progress. We feel that the recent addition of the Texas A&M group addresses both intellectual leadership and technical help. So would the Rutgers group if they decide definitively to join. The existing collaboration is also being strengthened via increased funding for some groups and a clear delineation of responsibilities for the large Dubna group.

“Investigate the feasibility of a modular design for the SMD and the effect on the overall mechanical design of the calorimeter structure.”

As detailed in Sec. 4, the SMD design has been modified to incorporate 30° modules that can be inserted or extracted from the fully assembled detector. By devoting increased depth to the SMD layer, we have allowed for sufficient overlap of adjacent azimuthal sectors that the modularity does not introduce dead regions at the SMD module boundaries. This change, together with more detailed planning of the structure surrounding each calorimeter megatile, has led to a small increase in overall depth of the EEMC, as reported in Secs. 4 and 8. However, the STAR Operations Group considers the necessary relaxation of the endcap integration volume as manageable.

“Investigate the mechanical clearances before and after the STAR magnet is powered.”

STAR Chief Engineer Ralph Brown assures us that the poletip will move no more than 0.005” when the magnet is powered. The revised EEMC integration volume still allows 2.5” clearance from cables and services associated with the TPC. There is thus ample room for air circulation and for the slight tilting of the poletip that will be required when it is to be removed from the detector.

“Investigate and complete the study of the thermal effects of the magnet being powered. Investigate the effect of the magnetic field on the scintillator response and the calorimeter calibration. Complete the measurements to assess the appropriate magnetic field screening for the PMT’s and engineer the PMT boxes.”

The poletip trim coil runs typically at 85°F. The trip setpoints on the return cooling water allow a maximum swing of about 10°F before coil power would be cut off. However, the trim coil is thermally isolated from the poletip, which presently runs close to room temperature when the magnet is powered. As the planned PMT bases, high voltage distribution system and readout electronics for the EEMC are detailed, we are trying to update estimates of heat load and the implications for cooling needs in the PMT boxes. Other investigations of magnetic field effects on scintillators similar to that we plan to use indicate [17] that the response to ionizing particles is likely to shift by a few percent when the magnet power is on. Unfortunately, this change in response is not observed for UV light excitation of the scintillator [17], and so will not naturally be monitored by the envisioned laser system described in Sec. 7. Rather, we will rely on the comparison of cosmic ray and laser measurements made with the EEMC *in situ* within STAR, with field off *vs.* on, to calibrate this small shift. The laser system will measure any field-dependent gain shifts in PMT's. Field calculations and the design of the PMT boxes are in progress, as reported in Sec. 8. The interim results presented in that section make it clear that a workable solution to the magnetic shielding problem is feasible. The Texas A&M group has solved a similar problem, in similar ambient fields, for the MEGA collaboration at LAMPF.

“The likelihood of scintillation in the WLS fibers creating fake ‘double-peaks’ should be assessed.”

This potential problem has been discussed in detail with the D0 preshower group, who have performed extensive tests on triangular scintillating strips of very similar geometry to those planned for the EEMC. They have seen no evidence for scintillation in the WLS fibers at a level of a few percent of the light output from a similar thickness of plastic scintillator. In particular, they observe [18] a 25–30% dropoff in light yield as they scan MIP's across the face of a triangular strip, when they cross the location of the axial hole for the WLS fiber. This dip is precisely what is expected on the basis of the scintillating material removed to allow for the WLS fiber hole, and shows no sign of being filled in by scintillation in the fiber itself. On the basis of these results, we have gone in the revised modular SMD design for the EEMC to a fiber-routing scheme (see Sec. 5.4) in which fibers exiting from scintillating strips fold over onto the back of the SMD layer for routing to the outer circumference of the sector. This scheme would introduce sensitivity to “fake double-peaks” between very specific pairs of strips if the WLS scintillation were an appreciable problem. Thus, projected prototype tests of an SMD module should be able to rule out this problem at any level that could affect the $\gamma - \pi^0$ discrimination.

“The fiber design should be finalized and, if possible, the SMD design should be improved to avoid dealing with a large number of pigtailed of different lengths.”

Fiber routing plans for both the towers and SMD layers are described in Sec. 5. The revised SMD design still calls for a substantial range of variation in WLS fiber lengths. After discussion with the D0 preshower group, we have decided that the issues arising from pigtailed of different length are less serious than the potential “cures,” *e.g.*, choosing less symmetric *u*- and *v*-plane layouts for the scintillating strips, or reducing the angle between the strips in the two planes substantially below 90°.

“A more critical specification may be needed for the long term stability and rate effect criteria. For this an estimate of the integrated amount of charge collected at the anode over the lifetime of RHIC should be made for the innermost towers...”

The expected data rates near $\eta = 2$ do not, in fact, strongly exceed those in the barrel region. Detailed conservative estimates of integrated charge in the endcap region lead to a specification of long-term stability only slightly more stringent than that used for the barrel PMT's, namely,

requiring all other specifications to remain within quoted limits for an integrated anode charge of 25 C, as opposed to the 10 C used for barrel PMT requirements. The EEMC PMT's must also remain highly linear up to peak currents about twice as large as those for the barrel. Other PMT requirements are summarized in Sec. 6.

“For the MAPMT's ... the specifications ... should further require that the gain variation from channel to channel in one tube is less than a factor of 2, since the readout of these tubes uses only a 10-bit ADC.”

We agree with this specification. However, we have also discovered that variations in light output from different SMD strips may be comparable to the MAPMT channel-to-channel gain variations. To accommodate this range, we have decided to convert to 12-bit ADC's for the SMD, as well as for the towers. This decision engenders some significant re-engineering of SMD electronics from the barrel EMC, but re-engineering was envisioned in any case, due to the very different detector characteristics.

“The procedures for selecting a manufacturer for the tower tubes and the final selection/testing and measurement of important tube parameters ... need to be developed and test/measurement setups constructed.”

QA/QC procedures for the PMT's and MAPMT's are being developed, as summarized in Sec. 5. Collaborating institutions (Rice University and Kent State University) not involved in calorimeter megatile or SMD production have been assigned responsibility for the selection, testing and recording of phototube characteristics.

“Somewhat marginal are the 12-bit ADC's for the tower readout, since the energies are much higher in the endcap than in the barrel, and the 10-bit ADC for the SMD.”

The original plan for the barrel EMC tower electronics was to use 10-bit ADC's. The EEMC group helped to convince them to switch to 12-bit ADC's to accommodate the interesting dynamic range of signals in both the barrel and the endcap. This range for the endcap is $\approx 1000 : 1$, extending from 150 GeV electrons (from W decay) at the upper end to below the MIP peak (about 300 MeV shower equivalent) at the lower end. We have judged that possible advantages from converting to 14-bit ADC's for the endcap do not merit the re-engineering costs. In contrast, as indicated above, we have decided to switch to 12-bit ADC's for the endcap SMD, since here re-engineering costs were inevitable in any case.

“The third level trigger ... will require a large software effort. ... This large task should be started soon, and could easily be done by an institute not involved in the calorimeter construction.”

As detailed in Sec. 8.5, the Level 3 trigger software project is well under way. Extensive development of rapid algorithms for TPC track reconstruction has been carried out by STAR collaborators from the University of Frankfurt and by Pablo Yepes from Rice University. Yepes is also a collaborator on the EEMC. An IUCF postdoc, Jan Balewski, has developed the principles of an algorithm that combines TPC track and EMC hit information to reject pileup tracks with sufficient efficiency to meet the Level 3 requirements for high-luminosity running. Obviously, much software development remains to extract cluster information from the raw EMC (both barrel and endcap) ADC values, and to combine these with the TPC track reconstruction, to pass only those TPC clusters from useful candidate tracks, in an efficient way. Ongoing discussions are aimed also at identifying additional Level 3 hardware needs (i.e., additional CPU's) that may be needed to accomplish the necessary track filtering in the limited processing time available.

“It will be necessary to have systems in place for an initial 'cold start' calibration as

well as systems to track the gain variations of the tubes during running. ... We recommend that the collaboration develop these and other schemes to gain a much more detailed understanding than has been possible up to now. A dedicated workshop devoted to calibration issues should be called, inviting experts from other detector collaborations."

The suggested workshop was held at IUCF in September 1999. The speakers and conclusions are summarized in Sec. 7.2 of this report. We have adopted a calibration/monitoring system modeled after that being used for the PHENIX detector at RHIC. Initial absolute pre-calibrations of both tower and SMD scintillators will be based on measurements of cosmic rays, but transferred to the entire dynamic range of interest by means of a pulsed UV laser system incorporating precisely variable attenuators and monitor PMT's, as described in Secs. 7.3–4. The laser light will be injected directly into the scintillator material, and thus can also be used for online monitoring of the stability of the entire optical chain for both calorimeter towers and SMD. We anticipate this system should be capable of providing considerably better precalibrations than our 10% requirement. Its accuracy will be checked with a test beam run on our small prototype detector, after that detector is updated to include final scintillator, fiber, readout electronics and laser illumination configurations. Auxiliary monitoring capability will be provided by pulsed LED light fed into the PMT's and MAPMT's and a pulser to inject charge into the readout ADC's. Holes will be machined in the fiber routing guides for every few calorimeter layers, to allow manual insertion of radioactive sources for system tests during assembly, but we have no plans for an automatic source guide system to be used *in situ* within STAR.